Università Degli Studi di Genova

School of Mathematical, Physical and Natural Sciences

PhD course in
PHYSICS AND NANOSCIENCES

XXXVI cycle

A thesis submitted for the degree of
Doctor of Philosophy

Exploring the Biophysics of Aging: Chromatin Architecture Modifications in Hutchinson-Gilford Progeria Syndrome through Super Resolution Microscopy

Tutor:
Prof. Alberto Diaspro

Candidate:
Chantal Usai

Co-supervisors:
Prof. Paolo Bianchini
Dr. Isotta Cainero

Academic Year 2023-2024

To my brother

"*Sometimes I feel you with me in the dark*
And your face is in the faces of the strangers walking by me in the park
So though we cannot be together
I know that I will carry you wherever I go"

Tim Minchin

ACKNOWLEDGEMENTS

I would first like to thank my tutor, Prof. Alberto Diaspro, and my co-supervisor, Prof. Paolo Bianchini, for providing guidance and support throughout this thesis work and for offering me the valuable opportunity to carry out this work at the Istituto Italiano di Tecnologia.

I would also like to thank Dr. Isotta Cainero for helping me define my research project and mentoring me throughout my thesis work, for the long hours at the microscope together, for all the laughs, and so much more.

A special thanks to all those who, within the Nanoscopy group, supported me during this work, particularly Michele Oneto and Marco Scotto, for teaching me how to use a microscope. A special thanks also goes to my colleagues, Francesca and Elena, for their advice with the lab work and their patience with my lack of knowledge in biology.

Thanks to the other current and former PhD fellows and Postdocs in the Nanoscopy and MMS group, especially Andrea, Simone, Francesco, Alberta, Matteo, Fabio, Jack, and Eleonora, for making this academic journey so memorable and our lunch breaks so much fun.

An exceptional thank you goes to Laura, my lifelong chosen sister, and to Marika, my oldest friend. Thank you, girls, for everything, especially for giving me my favorite nephew.

Finally, I want to express my immense gratitude to my partner, Riccardo, for his unwavering support and belief in me throughout this journey, for all the clean mugs, and for his patience during the long weeks of writing this thesis. Also, thanks for all the birrette alla Lepre.

TABLE OF CONTENT

LIST OF FIGURES

LIST OF TABLES

1. INTRODUCTION

Hutchinson-Gilford Progeria Syndrome (HGPS) represents one of the most striking forms of human premature aging disorders. Characterized by accelerated aging throughout childhood, HGPS provides a unique opportunity to study the molecular pathways underlying aging and age-related pathologies. An essential aspect in comprehending this disease is the investigation of chromatin architecture modifications, the dynamic framework crucial for controlling gene expression and preserving genomic stability.

This thesis offers an in-depth biophysical investigation into the chromatin and nuclear lamina modifications associated with HGPS by bridging super-resolution microscopy and cellular biology. By exploiting super resolution microscopy's ability to provide a detailed view of cellular structures at a molecular level, this research aims to uncover the fine aspects of chromatin organization and its aberrations in an HGPS cellular model. A particular focus in this dissertation is posed on the use of Expansion Microscopy and its capability to increase the optical resolution of conventional microscopes, allowing for the exploration of the complex interactions at the interface between nuclear lamina and chromatin.

The significance of this study extends beyond the limitations of progeria. Understanding chromatin dynamics in HGPS can offer valuable insights into the underlying mechanisms of natural aging and age-related disorders.

This dissertation is organized into the following sections:

- Chapter 2 provides a comprehensive description of the organization of the cell nucleus, with particular emphasis on chromatin arrangement and its interaction with the nuclear lamina.
- Chapter 3 presents an overview of Hutchinson-Gilford Progeria Syndrome, with a particular focus on its effects at a cellular level.
- Chapter 4 provides a detailed introduction to fluorescence optical microscopy, mainly focusing on super resolution microscopy techniques.
- Chapter 5 reviews expansion microscopy, specifically discussing the

available protocols and validation practices.

- In chapter 6, the methodology and experimental approaches employed in this study are presented and explained.

- Chapter 7, which presents and discusses the results, is divided into two subsections. The first one presents the optimization of the expansion microscopy protocol. The second subsection examines the nuclear architecture modifications in our HGPS cellular model.

- Chapter 8 concludes with a concise overview of the conducted experimental study.

To summarize, the investigation of chromatin architecture modifications in HGPS using super resolution microscopy not only advances our comprehension of this rare yet significant disease but also contributes to expanding the knowledge in the fields of biophysics and cellular aging.

2. THE CELL NUCLEUS

The cellular nucleus, a defining feature of eukaryotic cells, is a highly organized and dynamic complex serving as the genetic material repository. The nuclear envelope (NE) functions as a crucial protective barrier that governs the transport of molecules between the nucleus and the cytoplasm via specialized nuclear pores. The nuclear lamina, an intricate proteinaceous scaffold, plays a pivotal role in the elaborate organization of the nucleus by providing essential structural support and influencing chromatin arrangement (Bridger et al., 2007). Within the intranuclear compartment, the genetic material is intricately organized into a dynamic structure known as chromatin, comprising a composite assembly of deoxyribonucleic acid (DNA), histone proteins, and various other proteins (Rippe, 2007). The nucleolus, a distinguishable subcompartment located within the nucleus containing only ribosomal DNA, orchestrates the processes of ribosomal ribonucleic acid (RNA) synthesis and ribosome assembly (Boisvert et al., 2007). The meticulous coordination of these components assumes paramount importance in regulating gene expression, DNA replication, and other indispensable cellular mechanisms, thereby highlighting the elaborate character of nuclear organization (Lai & Pugh, 2017).

2.1. Nuclear Envelope: More Than a Barrier

The NE is a double-membrane structure that surrounds the nucleus of eukaryotic cells, effectively segregating the nucleoplasm from the cytoplasm. The NE comprises two lipid bilayer membranes, the inner nuclear membrane (INM) and the outer nuclear membrane (ONM), divided by the perinuclear gap, which acts as a buffer region (Nigg, 1989). The double-membraned structure contains nuclear pores complexes, which are intricate channels acting as a gateway between the nucleus and the cytoplasm (Fig. 1).

The nuclear envelope is a highly dynamic structure that undergoes continuous remodeling throughout various cellular processes, including cell division, encompassing both mitosis and meiosis. During mitosis, the nuclear envelope disassembles, allowing for the segregation of chromosomes, followed by its subsequent reassembly in the resultant daughter cells (De Magistris & Antonin, 2018).

2.1.1. The Outer Nuclear Membrane

The ONM is an essential lipid bilayer that encloses the nucleus of eukaryotic cells, creating an effective barrier between its contents and the cytoplasm. The ONM exhibits continuity with the endoplasmic reticulum, creating a link between the nuclear envelope and the extensive network of membranes within the cell (D'Angelo & Hetzer, 2006). This connection plays a crucial role in controlling cells' mechanosensory function, enabling force transmission from the nucleoskeleton to the cytoskeleton (Uzer et al., 2016).

2.1.2. The Inner Nuclear Membrane

The INM is a highly specialized cellular structure that plays a crucial role in maintaining the integrity and functionality of the nucleus. As the lipid bilayer surrounding the nucleoplasm, the INM is in direct contact with the nuclear components, including the chromatin and the nuclear lamina (Wilson & Berk, 2010).

The proteins located within the INM are of utmost importance in governing nuclear organization and facilitating proper nuclear function. Integral membrane proteins like emerin, lamin B receptor, and MAN1 promote the attachment of the nuclear lamina to the inner surface of the nuclear envelope. The INM serves as a crucial structure for the anchorage of chromatin, thereby exerting a significant influence on the spatial arrangement of the genome (K. K. Lee et al., 2000).

2.1.3. The Nuclear Pore Complex

Nuclear pores, also known as nuclear pore complexes (NPCs), are large protein complexes traversing both inner and outer nuclear membranes (Davis, 1995). NPCs are composed of approximately 30 different proteins called nucleoporins (NUPs) that assemble symmetrically, creating an octagonal structure (Doye & Hurt, 1997). These complex structures regulate the selective transport of molecules between the nucleus and the cytoplasm, facilitating the passage of ions, small molecules, and macromolecules and ensuring a selective and controlled flow of substances between the nucleus and the cytoplasm (Gorlich, 1998).

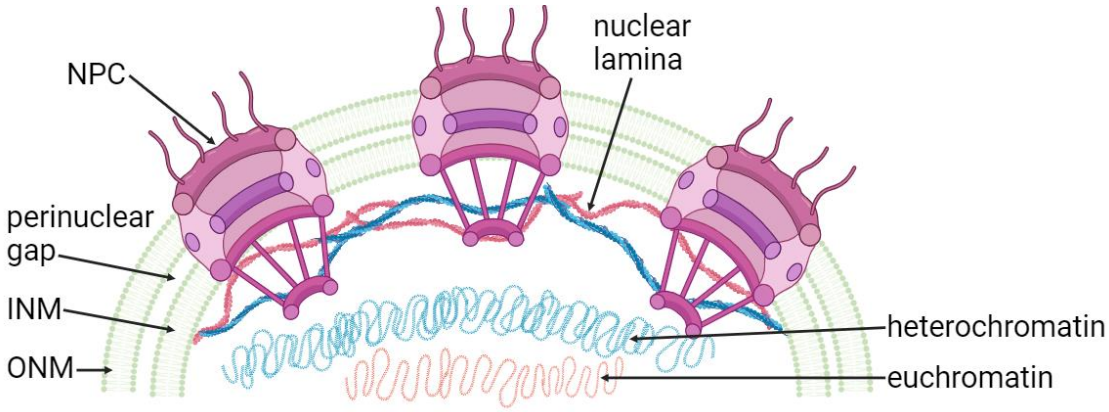

Fig. 1 Schematic representation of NE and nuclear lamina. Created with Biorender.com

The NPC comprises cytoplasmic filaments, a central channel, and a nuclear basket, each serving specific roles in molecular transport. Nuclear transport receptors, such as importins and exportins, identify distinct signals on cargo molecules and coordinate their passage in both directions through NPC (Markaki et al., 2010).

The nuclear pore also plays a role in organizing chromatin, regulating gene expression, and maintaining nuclear structure. Specifically, NUP153 has a crucial function in the regulation of active transcription (Vaquerizas et al., 2010). Localizing in the nuclear basket, NUP153 plays a crucial role in mediating the establishment of distinct nuclear environments favorable for transcriptional activity by actively tethering transcribed genes to the nuclear periphery. The interaction between NUP153 and RNA polymerase II, a DNA-dependent enzyme responsible for active gene transcription, suggests a direct involvement in the transcriptional process, potentially enhancing the transcription machinery's recruitment and functioning and playing a role in the intricate control of gene expression (Jacinto et al., 2015). The influence of NUP153 on the organization of chromatin highlights its more extensive involvement in the coordination of nuclear architecture, adding another level of intricacy to our comprehension of the diverse functionality of nucleoporins in the context of ongoing transcription (Liang & Hetzer, 2011).

2.2. Nuclear Lamina: Regulating Nuclear Structure

The nuclear lamina is a highly conserved structural protein framework below the INM of all eukaryotic cell nuclei. It offers support, stability, and regulatory control over several cellular activities. It functions as a mesh-like scaffold that interacts with chromatin and integral membrane proteins, assisting in maintaining the nucleus's shape and structural

integrity and offering structural reinforcement to the nuclear envelope, limiting excessive distortion during cellular processes like migration and division (Bridger et al., 2007a).

The nuclear lamina is primarily composed of two different type V intermediate filament proteins called lamins, which are classified as A and B. Lamin A and Lamin C, which originate from the alternative splicing of the LMNA gene, are exclusive to metazoan cells and play a crucial role in maintaining the structural and functional integrity of the nuclear envelope (Al-Saaidi & Bross, 2015). Instead, Lamin B1 and B2 are produced by two distinct genes, LMNB1 and LMNB2. The lamins undergo post-translational modifications, such as farnesylation, which is essential for their association with the INM (Camps et al., 2015).

Furthermore, the nuclear lamina is involved in chromatin organization, influencing gene positioning and regulating gene expression. It serves as a medium for the recruitment of regulatory proteins and transcription factors, which affect the transcriptional state of genes associated with the nuclear periphery (Dechat et al., 2008). The interaction between lamins and chromatin plays a role in the genome's spatial organization within the nucleus.

2.3. Chromatin organization: the Blueprint of Genetic Information

The cellular nucleus serves as the command center for the intricate orchestration of genetic information. At the heart of this complex process lies chromatin, a dynamic interplay of DNA and proteins. Although the hierarchical organization of chromatin (Fig. 2) at the nanoscale level is still not fully understood, it is known that at its core lies the nucleosome, a fundamental unit that serves as the architectural cornerstone constituting the elemental packaging of DNA within the cell nucleus (Masae et al., 2018). The nucleosome possesses a 'beads on a string' configuration, enveloping 147 DNA base pairs around histone octamers, creating the first level of DNA organization with these 11-nanometer DNA-nucleosome polymers (Luger, 2001). Each histone octamer consists of two duplicates of the histone proteins H2A, H2B, H3, and H4 and is characterized by the presence of three α-helices that are interconnected by short loops (Dans et al., 2016). The interactions between histones, specifically, H3 paired with H4 and H2A paired with H2B, culminate in a stable tetramer through H3:H3 associations. This arrangement exposes the amino-terminal tails of histones, creating a positive charge necessary for the interactions with the

Fig. 2 Schematic representation of chromatin organization. Created with Biorender.com

negatively charged DNA (Chakravarthy et al., 2005). The connection between nucleosomes involves the linker histone H1, which contributes to chromatin's stabilization and further compaction. Notably, the human genome exhibits a variety of H1 histone subtypes, each playing a distinct role in the structure and function of chromatin (Happel & Doenecke, 2009).

While the basic nucleosome structure is well established, our understanding of higher-order chromatin organization is still evolving. Traditional models, like the 30 nm fiber model, have been challenged by recent research suggesting more complex and varied folding patterns of chromatin. By using a combination of fluorescent staining and electron microscopy, a recent study revealed chromatin as a dynamic, disordered chain with diameters ranging from 5 to 24 nanometers (Ou et al., 2017). This chain is densely packed in various configurations, differing between interphase and mitotic cells. Chromatin's configuration is not static but changes throughout a cell's life cycle. During mitosis, chromatin undergoes significant condensation to form chromosomes, which are vital for efficient and accurate genetic material segregation (Bonev & Cavalli, 2016). Although various models have been proposed to explain chromosome formation, a complete understanding of these processes remains elusive (Tremethick, 2007).

Nevertheless, chromosome territories, regions occupied by individual chromosomes, influence gene expression by affecting gene accessibility. The different levels of chromatin compaction, traditionally known as euchromatin and heterochromatin, play crucial roles in this phase, with euchromatin being less condensed and more transcriptionally active (Allis & Jenuwein, 2016). Chromatin remodeling is a dynamic process that occurs throughout the cell life. During cell division, chromosomes condense, while in interphase, chromatin decondenses, with euchromatin housing active genes and heterochromatin remaining condensed (Duc & Thiriet, 2021).

The intricate spatial arrangement of chromatin plays a crucial role in determining the

accessibility of genes, thereby serving as a pivotal factor in the regulatory mechanisms that underlie the functional importance of higher-order chromatin structures. Within the vast realm of chromatin organization, it becomes evident that microscopic techniques emerge as an indispensable ally. Electron microscopy constitutes a powerful tool for elucidating detailed structural complexities of nucleosomes and chromatin fibers. Optical microscopy, particularly super-resolution techniques, provides spatial precision and molecular specificity, allowing for the exploration of the dynamic organization of chromatin. Subsequent chapters will delve into these techniques and their applications in revealing the intricate molecular structure within the nucleus of mammalian cells.

2.3.1. Epigenetic Modifications: Orchestrating The Genome Function

The nucleosomal arrangement is vital for regulating gene accessibility and expression and can be modulated by post-translational processing of DNA and histones, called epigenetic modifications, which can alter chromatin's physical structure, impacting the accessibility and regulation of genetic information (Duc & Thiriet, 2021). Epigenetic modifications encompass a myriad of chemical alterations that modulate gene expression without altering the underlying DNA sequence. This sophisticated molecular language is essential in cellular differentiation, development, and response to environmental cues (Chrun et al., 2017).

A crucial post-translational modification is DNA methylation, typically involving the addition of a methyl group to the 5th carbon of the cytosine ring within CpG dinucleotides. This process mainly occurs in CpG islands found in gene promoters, and it is catalyzed by DNA methyltransferases (DNMTs, Fuks et al., 2000). DNA methylation is commonly linked to transcriptional repression, as it can impede the binding of transcription factors to DNA or recruit proteins that suppress transcription, although its effects can be context-dependent (Murr, 2010).

While DNA can only be methylated, histones undergo a vatiety of modifications. Among the more common ones, methylation, acetylation, and phosphorylation are worth mentioning (Vaissiere et al., 2008).

Histone methylation occurs on particular lysine or arginine residues located on histone tails. This modification is mediated by different histone methyltransferases

(HMTs), which introduce methyl groups, and histone demethylases (HDMs), which eliminate them. Depending on the specific methylated residues, histone methylation can either activate or suppress transcription (Castillo-Aguilera et al., 2017). For example, histone H3 lysine 4 (H3K4me) methylation is generally associated with transcriptional activation, whereas methylation of histone H3 lysine 9 (H3K9me, H3K9me2, H3K9me3) is connected to gene repression (Patel & Wang, 2013). H3K9me2, mediated by Histone-lysine N-methyltransferase (EHMT1), constitutes a standard marker for heterochromatin (Poleshko et al., 2019).

Histone acetylation is the enzymatic addition of an acetyl group to lysine residues located on histone tails, mediated by histone acetyltransferases (HATs) and reversed by histone deacetylases (HDACs). Acetylation of histones reduces the electrostatic attraction between the histones and DNA, resulting in a chromatin structure that is more open and may be easily accessed by transcriptional machinery. Therefore, histone acetylation is commonly associated with the stimulation of gene transcription (K. K. Lee & Workman, 2007). A common marker for transcriptionally active euchromatin is H3K9ac, whose acetylation is regulated by Histone acetyltransferase (KAT2A).

Finally, histone phosphorylation involves adding a phosphate group to serine or threonine residues of histone proteins. This modification is catalyzed by kinases and reversed by phosphatases (Rossetto et al., 2012). Histone phosphorylation plays a significant role in regulating chromatin condensation during cell division and in response to DNA damage. For instance, the phosphorylation of histone histone H2AX (γH2AX) is pivotal for DNA damage detection and response (Lesterlin et al., 2014).

Epigenetic modifications play a crucial role in governing the structure and function of chromatin, hence controlling gene expression and cellular phenotype. The deregulation of these mechanisms is associated with various illnesses, including cancer and genetic diseases (Kanwal & Gupta, 2012).

2.3.2. Tethering chromatin to the nuclear lamina

A delicate interplay of proteins is involved in the attachment of chromatin to the nuclear lamina. A pivotal player in this ensemble are Lamin-associated domains (LADs), genomic regions interacting with the nuclear lamina (Alagna et al., 2023). The tethering of

chromatin to the nuclear lamina is mediated by lamina-associated proteins (LAPs) that establish dynamic connections between specific genomic regions and the lamina (Bridger et al., 2007). This tethering not only influences spatial organization but also contributes to the regulation of gene expression, highlighting the intimate link between chromatin organization and nuclear architecture.

Among many other proteins, two proteins, Heterochromatin Protein 1 alpha (HP1α) and Proline-Rich Region Protein 14 (PRR14), emerge as a central protagonist in this process. HP1α, a chromodomain-containing protein, promotes and maintains heterochromatin by specifically binding to di- and tri-methylated histone H3 at lysine 9 (H3K9me2, H3K9me3), playing a central role in gene silencing and chromatin compaction (Kiseleva & Poleshko, 2023). Following disassembly in the early stages of mitosis, PRR14 undergoes reassembly in a two-step process. Initially, it binds to anaphase chromosomes attaching to peripheral HP1-H3K9me3-marked heterochromatin (Fig. 3), and subsequently associates with the nuclear lamina during telophase. PRR14 may therefore have a role in determining the specific location of heterochromatin when it reattaches to the nuclear lamina as cells complete mitosis (Poleshko et al., 2013).

The interplay between HP1α, PRR14, and the nuclear lamina underscores the intricate regulatory mechanisms governing chromatin organization within the three-dimensional confines of the nucleus, and their dysregulation may play a role in numerous diseases,

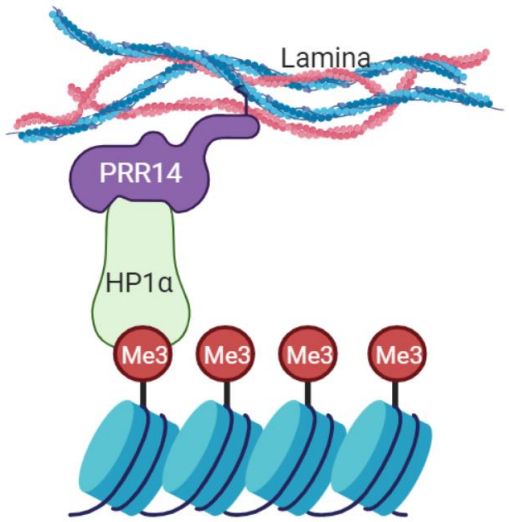

Fig. 3 Schematic representation of PRR14 and HP1α tethering heterochromatin to the nuclear lamina. Created with Biorender.com

especially in genetic disorders caused by mutations in genes that encode proteins of the nuclear lamina, also known as laminopathies. This subject will be further explored in the next chapter.

3. HUTCHINSON-GILFORD PROGERIA SYNDROME: UNRAVELING THE ENIGMA OF PREMATURE AGING AT THE CELLULAR LEVEL

Hutchinson-Gilford Progeria Syndrome (HGPS) stands as a remarkable anomaly within the spectrum of laminopathies genetic disorders, presenting an accelerated aging process that defies the conventional trajectory of human development (McKenna et al., 2013). This exceedingly rare condition, occurring in approximately 1 in every 20 million live births, has captivated the attention of biophysicists, posing a challenge to the existing understanding of cellular aging and underscoring the intricate interplay between genetics and the aging process (Burtner & Kennedy, 2010).

3.1. Phenotypic effects and symptoms

Individuals with HGPS have a unique collection of features at the phenotypic level, distinguishing them from their counterparts. The defining characteristic is accelerated aging, resulting in the rapid emergence of symptoms associated with age, usually noticeable during the initial two years of life. Affected individuals exhibit a striking resemblance to elderly persons, presenting with characteristics such as alopecia (loss of hair), restricted joint movement, and a distinctive facial look characterized by a high forehead, small chin, and thin lips (Fig. 4, Hennekam, 2006).

Furthermore, the cardiovascular system bears a significant burden in HGPS, with affected individuals commonly experiencing cardiovascular issues reminiscent of those seen in much older adults. Cardiovascular complications, including arteriosclerosis and cardiovascular calcification, contribute to the high mortality rate associated with HGPS, often resulting in death during early adolescence due to cardiovascular events (Capell et al., 2007).

Beyond the overt signs of premature aging, HGPS also manifests in other physiological abnormalities. Musculoskeletal deformities, growth retardation, and a predisposition to hip dislocations further underscore the profound impact of this syndrome on multiple organ systems (Coppede, 2021).

Fig. 4 Images depicting a 7-year-old female afflicted with HGPS, specifically characterized by the LMNA c.1824C>T genetic mutation.

3.2. Cellular Characteristics

Within the intricate landscape of cellular biology, the origins of HGPS are rooted in a genetic anomaly. The vast majority of HGPS cases can be attributed to a de novo mutation in the LMNA gene, which can be classified as a point mutation, specifically a single-nucleotide substitution (J. M. Lee et al., 2016). The LMNA gene is responsible for encoding the necessary instructions for the synthesis of lamin A and lamin C proteins (Al-Saaidi & Bross, 2015). These proteins play a crucial role as integral constituents of the nuclear lamina, a structure that, among other functions, confers structural stability to the cell nucleus. Among the 18 possible mutations, the mutation responsible for HGPS most frequently manifests at position 1824 of the LMNA gene, resulting in a genomic-level substitution of cytosine (C) with thymine (T). The occurrence of this C >T substitution leads to the production of a mutant form of lamin A protein known as LAΔ50 or Progerin (Luo et al., 2014).

Below is a detailed breakdown of the mutation and its consequences at a cellular level:

- Consequence on Pre-mRNA: the LMNA gene undergoes transcription to

produce a precursor mRNA (pre-mRNA). The point mutation in HGPS results in the incorporation of the mutant nucleotide into the pre-mRNA.

- Aberrant splicing: the mutated pre-mRNA molecule undergoes splicing, a crucial step in gene expression. During splicing, introns, which are non-coding regions within the pre-mRNA, are excised, while exons, which contain the coding regions, are joined together to generate the mature mRNA molecule. This intricate process ensures the proper removal of non-coding regions and the accurate assembly of coding regions, ultimately contributing to the production of functional mRNA transcripts. In HGPS, the mutation at position 1824 leads to a cryptic splicing of the LMNA mRNA, causing the omission of 150 nucleotides (J. M. Lee et al., 2016).

- Creation of Abnormal Protein: the mRNA produced during the aberrant splicing encodes for the mutated LAΔ50 or progerin, a lamin A variant missing 50 amino acids at its C terminus (Luo et al., 2014). Progerin is characterized by the absence of a cleavage site typically observed in the wild-type (WT) lamin A protein. This cleavage site is crucial for the removal of a farnesyl group during the post-translational modification process (Fig. 5).

- Accumulation of Progerin: due to the absence of the cleavage site, the permanently farnesylated progerin interferes with the normal turnover of lamin A, leading to the persistence of the mutant protein in the nuclear envelope. The consequences of progerin accumulation are multifaceted and have profound implications for cellular function (Dreesen, 2020).

- Nuclear Envelope Abnormalities: the accumulation of progerin causes structural abnormalities in the NE, leading to a condition known as nuclear blebbing. The observed phenomenon is characterized by the presence of irregular bulges and invaginations within the nuclear membrane. Progerin has been shown to interact with specific nucleoporins within the NPC, such as Nup62 and Nup153 (Martins et al., 2020), suggesting that the abnormal protein affects the composition and the NPC. The presence of progerin can alter the distribution and organization of NPCs, disrupting their normal

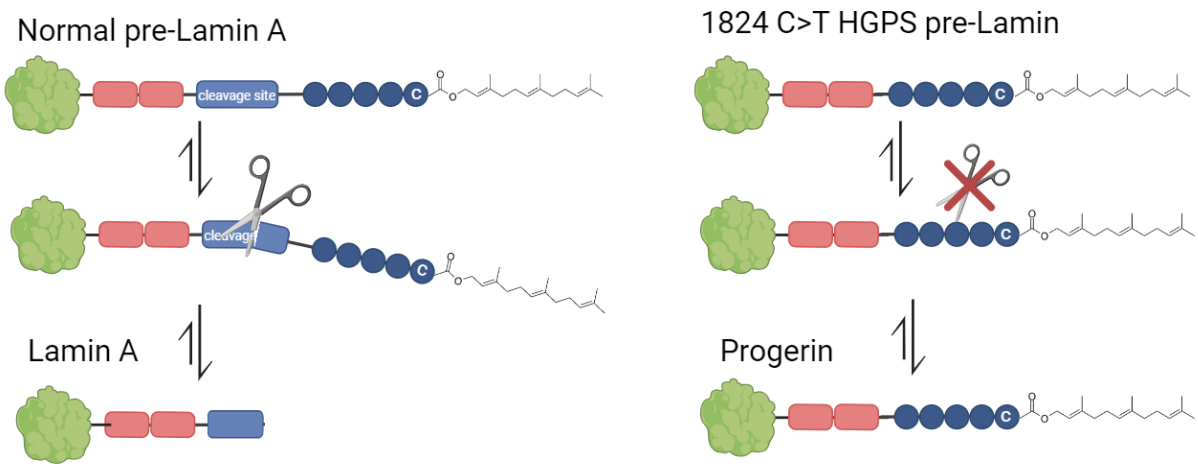

Fig. 5 Schematic representation of aberrant protein production. Created with Biorender.com

function and leading to impaired nucleocytoplasmic transport (Röhrl et al., 2021).

- Chromatin Disorganization: the nuclear lamina, containing lamin proteins, is crucial for maintaining the spatial organization of chromatin within the nucleus. The accumulation of progerin in the NE of HGPS cells contributes to chromatin disorganization (Arancio et al., 2014). Progerin-induced alterations in chromatin structure also impact the epigenetic landscape, causing alterations in DNA methylation and histone modifications, potentially affecting gene expression and regulatory processes. The disorganization of chromatin is particularly evident in regions near the NE, ultimately leading to the loss of peripheral heterochromatin (Prokocimer et al., 2013).

- DNA Damage and Repair Deficiency: HGPS cells exhibit increased susceptibility to DNA damage, such as double-strand breaks (DSB), due to impaired DNA repair mechanisms. Cellular accumulation of DBS causes genome instability, leading to systemic and premature aging. Fibroblasts from HGPS patients exhibit an elevated frequency of DSB and an upregulation of nuclear foci of the biomarker γH2AX (Musich & Zou, 2011).

- Cellular Senescence: the cellular consequences of progerin accumulation often lead to premature cellular senescence, where cells cease to divide and become metabolically inactive. Senescent cells, characterized by irreversible cell cycle arrest, have been implicated in the pathogenesis of tissue

dysfunction and degeneration, playing a role in the degenerative effects on tissues and organs observed in HGPS (Röhrl et al., 2021).

The intricate interplay of these cellular effects underscores the complexity of HGPS. Scientific researchers in related fields are actively investigating these mechanisms to uncover potential therapeutic targets. Understanding the cellular pathology of HGPS is not limited to shedding light on the molecular basis of premature aging in this syndrome, it also offers valuable perspectives into the broader realm of cellular aging and degeneration.

4. FLUORESCENCE OPTICAL MICROSCOPY AND THE CHALLENGE OF RESOLUTION

Fluorescence optical microscopy is a crucial tool for modern biological and biophysical research, allowing for visualizing complex biological processes with remarkable specificity and sensitivity. It enables detailed visualization of cellular components, molecular interactions, and tracking of dynamic processes in live cells, promoting a deeper understanding of cellular activities and mechanisms (Conchello & Lichtman, 2005). At its core, this technique leverages the properties of fluorescence, which is the emission of light by a substance that has absorbed light or other electromagnetic radiation, to generate high-contrast images of structures and molecules within cells and tissues.

The fundamental principle behind fluorescent optical microscopy revolves around the excitation of fluorescent molecules, known as fluorophores, which emit light at a longer wavelength after absorbing light at a specified wavelength. In order to understand these transitions, a widely employed tool for fluorescence microscopy is the Jablonski diagram (Fig. 6). This diagram is a graphical representation illustrating the electronic states of a molecule and the different possible transitions between these states. It depicts how a

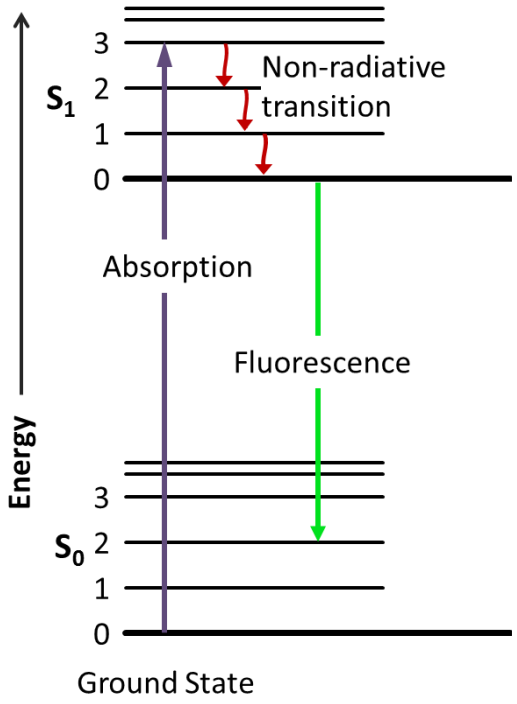

Fig. 6 Jablonski diagram showing the relevant energy transitions for fluorescence emission. Reproduced from https://commons.wikimedia.org/wiki/File:Jablonski_Diagram_of_Fluorescence_Only.png Creative Commons CC0 1.0 Universal Public Domain Dedication.

molecule, after the absorption of a photon, transitions from a state of lower energy, commonly referred to as the ground state, to a state of heightened energy, known as the excited state. This excitation is followed by non-radiative processes like internal conversion and vibrational relaxation, which lead the molecule to a lower vibrational level of the excited state. The molecule then returns to the ground state, emitting a photon of lower energy (longer wavelength) than the absorbed photon, through a process known as fluorescence emission. This emission is essential in fluorescence microscopy to visualize specific components within biological samples.

An essential aspect of fluorescence microscopy, and indeed all forms of optical microscopy, is the concept of resolution, which refers to the ability of a microscope to discern two closely positioned points as distinct entities. Resolution quantifies the level of detail observable in the generated images, and it is primarily limited by the diffraction of light. Diffraction is a physical phenomenon associated with the propagation of waves encountering an obstacle or a slit whose dimensions are comparable to or smaller than its wavelength. In accordance with the Huygens-Fresnel principle, after light has passed through a slit, each point of the slit behaves as if it were itself a source of circular waves, and these waves interact with each other creating an interference pattern. In fluorescence optical microscopy, fluorescent molecules act as point-like light sources, and when their emitted light traverses the circular aperture of a microscope lens, as a result of diffraction, the light scatters and creates a distinct pattern called Airy disk (Murphy D, 2012). Airy disks are characterized by the presence of a central bright spot, containing ~80% of the total light, encircled by concentric rings of light with diminishing intensity (Fig. 7 A). The dimensions of the Airy disk play a pivotal role in establishing the level of detail that a microscope may resolve, with smaller Airy disks enabling better resolution (Dunst & Tomancak, 2019). As the distance between two point sources of light decreases, the Airy disks associated with each source start to intersect. Once they overlap beyond a specific threshold determined by the Rayleigh criterion (Rayleigh, 1879), the microscope loses its ability to differentiate between the two distinct points, causing them to appear as a single entity. The overlap between Airy disks establishes the fundamental resolution threshold in an optical microscope . In the context of fluorescence microscopy, the diffraction limit d for light having a certain wavelength λ was postulated by Ernst Abbe in the late 19th century (Abbe, 1873) as:

$$d = \frac{\lambda}{2NA} \tag{4.1}$$

The numerical aperture NA (Fig. 7 D) represents the angular extent to which a given optical system is capable of accepting or emitting light and is defined as:

$$NA = nsin\alpha \tag{4.3}$$

Where n is the refraction index of the medium between the sample and the objective, and α is the half-angle of the cone of light that can be effectively collected by a lens. Considering visible light having λ in the range of 400-700 nm, conventional fluorescence microscopy has a lateral resolution of about 200 nm and about 600 nm along the optical axis.

Abbe's diffraction limit was later redefined by John William Strutt, who postulated the Rayleigh criterion defining two Airy patterns as resolved if one diffraction figure's central maximum aligns with the other's first minimum (Fig. 7 B). Rayleigh´s diffraction limit is given by:

$$d = 0.61\frac{\lambda}{NA} \tag{4.2}$$

In an image produced by a microscope, the Airy disk is better described by the Point Spread Function (PSF, Fig. 7 C) (Sheppard & Choudhury, 1977). The PSF is a mathematical representation of how a point source of light, such as a fluorescent molecule, is represented by an optical system, including information about the distribution of light in lateral (x and y) and axial (z) dimensions. The PSF fundamentally characterizes the three-dimensional configuration of the Airy disk, and it is essential for comprehending and measuring the resolution of a microscope.

In summary, the resolution challenge in fluorescent optical microscopy is primarily determined by the interplay among diffraction, the generation of Airy disks, and the parameters of the PSF. Each of these factors adds to the inherent physical constraints on our ability to discern minute details in the microscopic realm, guiding the development of advanced techniques to glimpse beyond these limits.

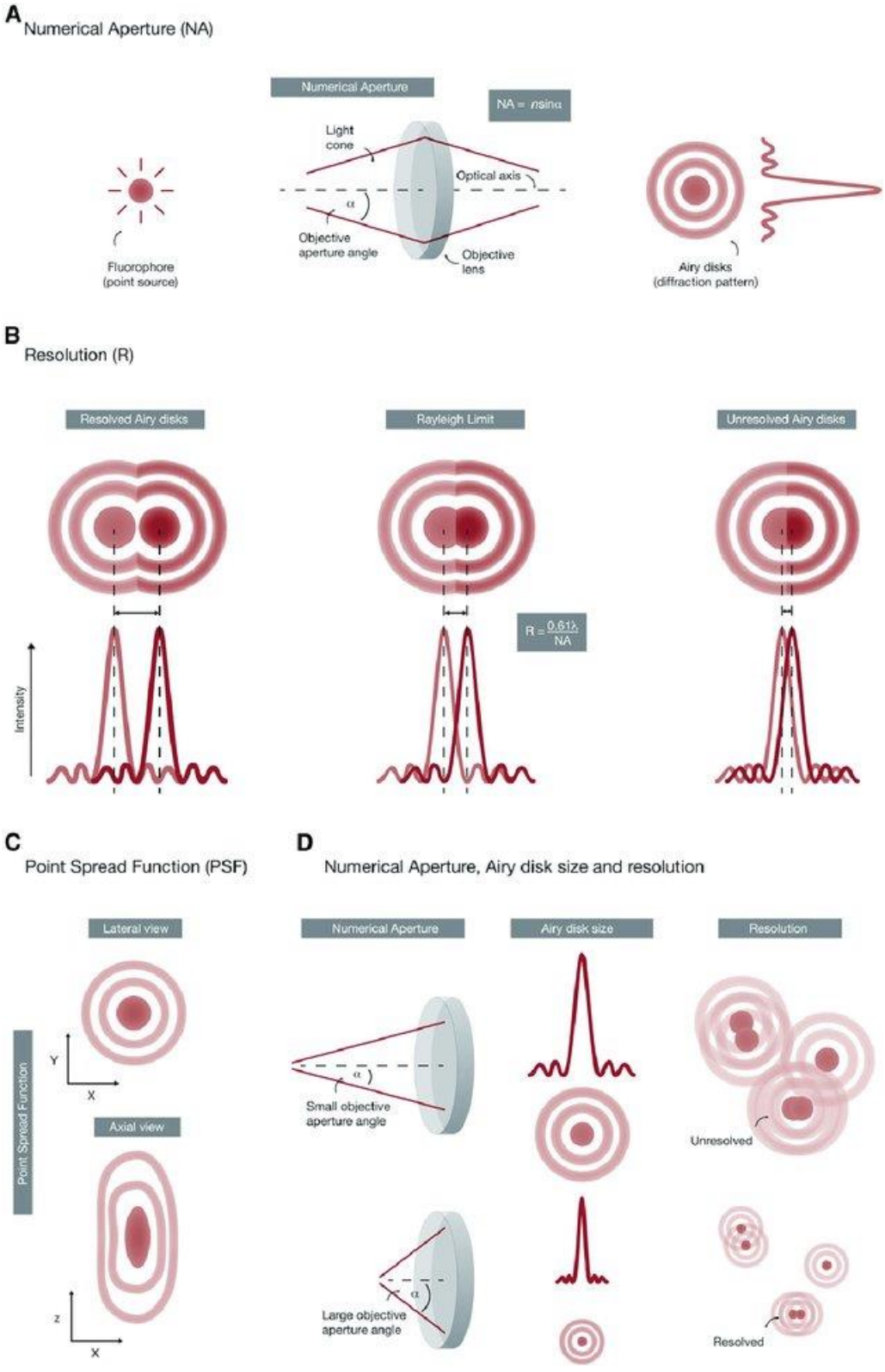

Fig. 7 Schematic representation of light emitted by a point-like source generating an Airy disk traversing an objective with a given numerical aperture (A). Representation of the concept of resolution (B). Axial and lateral view of the Point Spread Function (PSF) generated by the optical system (C). The effect of NA on Airy disk dimension and resolution power (D). Image adapted from (Dunst & Tomancak, 2019), CC BY 4.0

4.1. Super Resolution Microscopy

In 1955, Giuliano Toraldo di Francia introduced the concept of super-resolution microscopy (SRM) as the capability of a microscope to image with a level of detail smaller than the Abbe diffraction limit (Toraldo di Francia et al., 1955). This limitation can be bypassed by incorporating supplementary information in the process of creating an image.

4.1.1. Confocal Microscopy

Confocal microscopy offers significant advances compared to conventional wide-field optical microscopy, improving image contrast and resolution (Fig. 8). This laser scanning technique uses point-by-point illumination, supplying the optical system with the additional information provided by the precise positioning of the scanning beam (T. Wilson, 1984). The principle behind the confocal is to selectively gather the signals from the focal plane of the lens by using a small opening, known as a pinhole, to exclude out-of-focus light during image generation and effectively reduce background noise (Jonkman, 2020).

Moreover, a confocal microscope can perform three-dimensional (3D) imaging by sequentially shifting the focal plane across the depth of the sample, in a process referred to as optical sectioning, enabling the construction of intricate 3D models of complex structures within biological specimens (Amos & White, 2003).

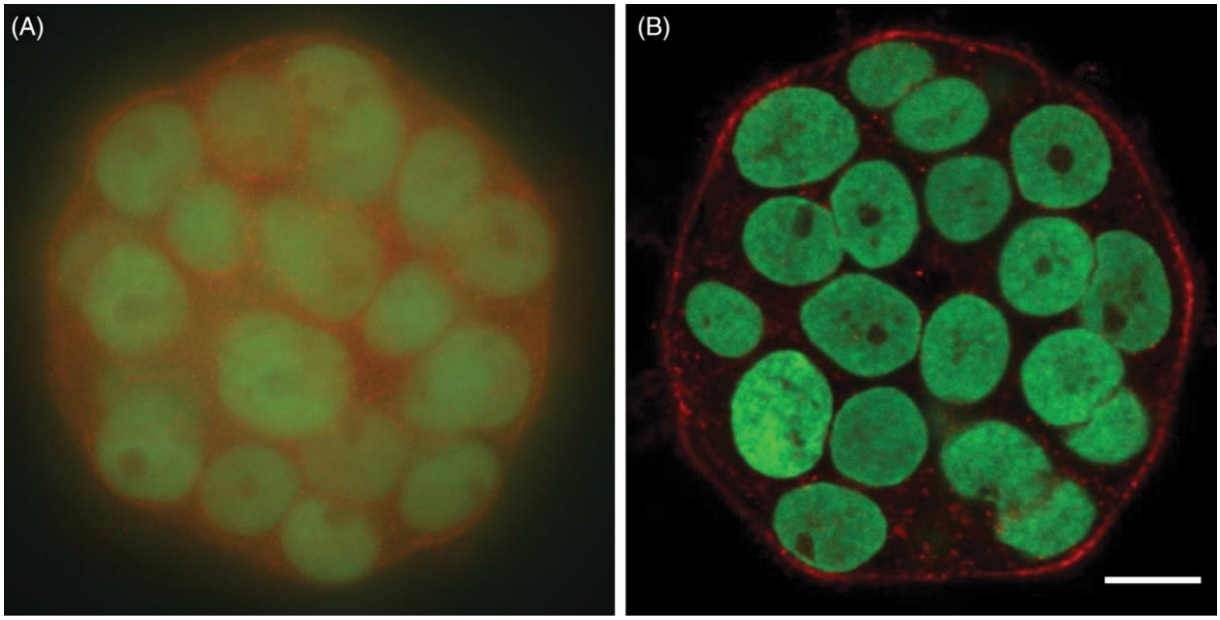

Fig. 8 Comparison between Widefield (A) and Confocal (B) imaging of an organoid expressing nuclear GFP and RFP on membranes. Scalebar 10 μm- Reproduced from Jonkman, 2020.

4.2. Optical Nanoscopy

The nomenclature “optical nanoscopy” has been attributed to certain SRM techniques due to their capability to visualize biological structures at the nanometer scale (Diaspro & Bianchini, 2020). These super-resolution techniques can be broadly categorized into two groups:

- Deterministic super-resolution: in this group, resolution beyond the diffraction limit is achieved by locally physically controlling the fluorescent emission of fluorophores through the utilization of REversible Saturable Optical Fluorescence Transitions (RESOLFT, Hell, 2005)). STimulated Emission Depletion (STED, Hell & Wichmann, 1994) falls under this category.

- Stochastic super-resolution: in this group, super-resolution relies on the temporal dynamics of specific fluorescent molecules. Within this set of approaches, the concept involves the temporal separation of two neighboring fluorophores by the stochastic alternation between a state of darkness and a state of brightness. Single-Molecule Localization Microscopy (SMLM) methods such as PhotoActivated Localization Microscopy (PALM, Betzig et al., 2006) and Stochastic Optical Reconstruction Microscopy (STORM, Rust et al., 2006) are examples of this family of techniques.

4.2.1. Stimulated Emission Depletion Microscopy

Stimulated Emission Depletion (STED) microscopy is a cutting-edge technique pioneered by Stefan Hell during the 1990s (Hell & Wichmann, 1994) that has revolutionized the field of optical microscopy by enabling imaging at spatial resolutions beyond the diffraction limit (Hell et al., 2003). This innovative super-resolution microscopy method led Eric Betzig, Stefan W.Hell, and William E.Moerner to win the Nobel Prize in Chemistry in 2014 “for the development of super-resolution fluorescence microscopy”.

Similarly to a confocal microscope, STED microscopy is based on a scanning setup that employs point-by-point illumination and a pinhole to remove out-of-focus signals. In addition to the confocal setup, STED uses a coalignment of the Gaussian excitation beam with a second doughnut-shaped beam at a longer wavelength, known as a depletion beam, to

force fluorophores to the dark state via stimulated emission (SE, Fig. 10 A). This approach is based on the principle of RESOLFT (Hell, 2005), exploiting the reversible and saturable transition of fluorescent molecules between two states: an 'on' state where they emit fluorescence and an 'off', non-fluorescent state. Thus, the sub-diffraction spatial resolution is achieved by preventing the simultaneous emission of fluorophores that are closer together than the diffraction limit by transiently moving fluorophores between these two states (Heilemann, 2010).

In order to quench the fluorescence around the focal point effectively, the PSF of the depletion beam should possess an intensity distribution with null intensity at its core and maximum intensity at its periphery (Fig. 9). For this reason, a doughnut-shaped beam is created by placing an optical component, known as a vortex phase plate, in the path of the depletion laser, allowing the process of SE to saturate exclusively the outer region of the excitation volume (Vicidomini et al., 2018). Consequently, the spontaneous fluorescence emission will only happen at the central region of the excited volume (Fig. 10 B).

Therefore, for STED microscopy, we can revise the definition of diffraction limit as:

$$d = \frac{\lambda}{nsin\alpha\sqrt{1+\frac{I}{I_{sat}}}} \tag{4.4}$$

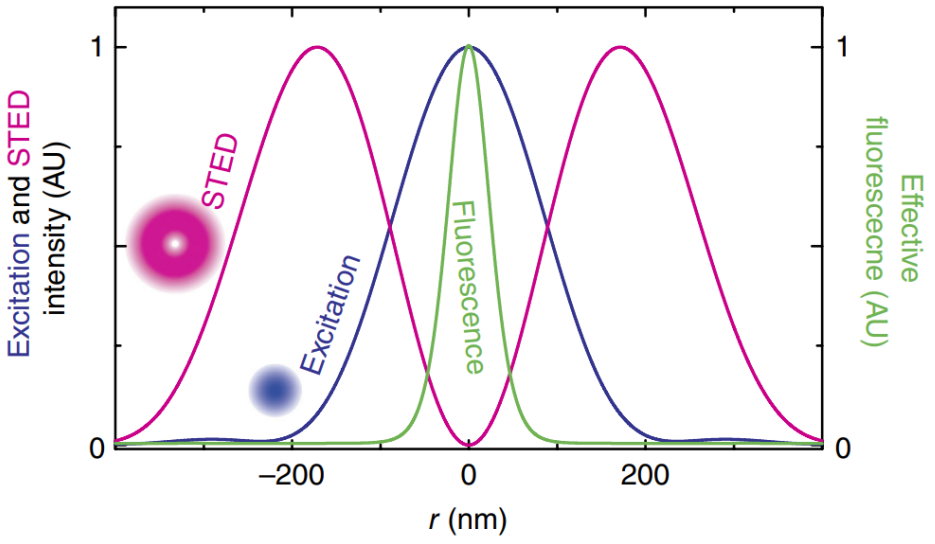

Fig. 9 Schematic representation of fluorescence excitation and STED intensity distribution with subsequent effective fluorescent emission. Adapted from Vicidomini et al., 2018.

Where I is the maximum depletion laser intensity and I_{sat} is the saturation intensity, defined as the power needed to decrease the spontaneous fluorescence emission intensity by half.

Although all the fluorescence emission in the outer scanning area should be depleted, there are always fluorophores that are unaffected by the depletion laser and continue to emit fluorescence, worsening the achievable resolution. A possible solution to this drawback is to filter photons based on their arrival time, selectively excluding the ones emitted during the initial, more intense phase of fluorescence, which usually contains a higher proportion of photons originating from the outer region of the focal area, in a process known as gating. Gated STED (g-STED) temporal filtering effectively narrows the region from which the fluorescence signal is collected, allowing for nanoscale resolution (Vicidomini et al., 2013).

The primary limitation of STED is the requirement for a high-intensity depletion laser, which can potentially cause photodamage and photobleaching. Therefore, extreme caution is required in performing live-cell imaging. Finally, careful planning of STED experiments is needed, especially in choosing a suitable fluorophore, which should have a large Stokes shift and an emission spectrum whose tail is matched by the depletion laser.

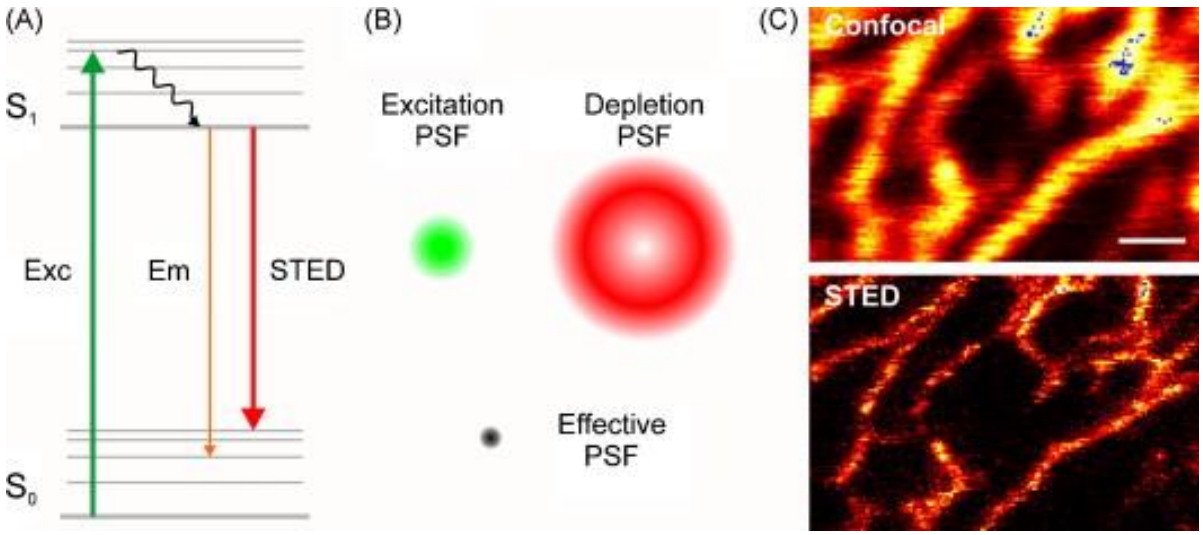

Fig. 10 Schematic representation of the Jablonski diagram showing the relevant energy transitions for STED (A). The two laser PSFs and the resultant effective PSF of the fluorescence emission (B). Comparison between confocal and STED imaging of mammalian cell´s endoplasmatic reticulum. Scale bar 1 μm (C). Reproduced from Heilemann, 2010

4.2.2. Stochastic Optical Reconstruction Microscopy

Stochastic Optical Reconstruction Microscopy (STORM) is a super-resolution imaging technique first described by Rust, Bates, and Zhuang in 2006 (Rust et al., 2006). STORM relies on the precise localization of individual fluorescent molecules activated in a stochastic manner. In this technique, subsets of fluorophores emit intermittently and are imaged over a specific period of time, ensuring that individual molecules, separated by distances smaller than the diffraction limit, can be distinctly localized *via* temporal separation. By localizing these molecules over multiple cycles and compiling these localizations, STORM can reconstruct a high-resolution image (van de Linde et al., 2011).

In its first presentation, STORM utilizes a unique method involving a fluorophore pair, a reporter and an activator dye, such as Cy5-Cy3. The reporter dye's ability to photoswitch under specific conditions, triggered by the activator dye's absorption wavelength, is the basic principle behind STORM functionality (Bates et al., 2005, Fig. 11). A high-intensity 633-nm red laser is used to force the Cy5 probes into a state of darkness. Next, a secondary laser pulse with a wavelength of 532 nm is employed to excite the Cy3 dye, which subsequently reactivates a portion of the Cy5, obtaining a significantly reduced signal density. By iteratively repeating this process, it becomes possible to generate super-resolution images. Direct STORM (dSTORM, Heilemann et al., 2008) streamlines this process by using

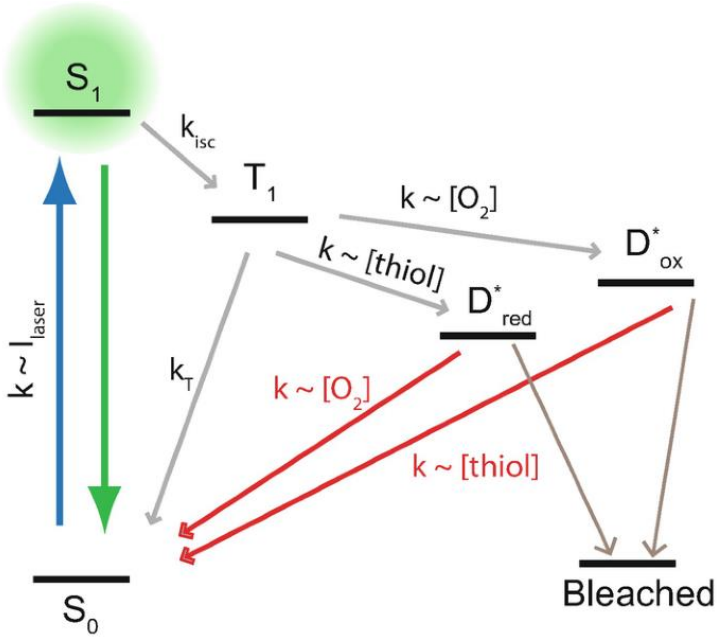

Fig. 11 Schematic representation of the Jablonski diagram showing the relevant energy transitions for STORM with their constants. Adapted from Soeller & Jayasinghe, 2018.

conventional photoswitchable fluorescent carbocyanine dyes such as Alexa Fluor 647 and Cy5, as well as rhodamine class dyes like Alexa Fluor 488 and Atto 532. These fluorophores can reversibly switch between on and off states in a controlled chemical environment without the need for an activator dye, allowing for more straightforward implementation. Precise control over the photoswitching process, enabling the transition between bright and dark states, is crucial for achieving accurate dSTORM imaging (Fig. 12). The transition to a dark state is believed to occur by the photochemical reduction of the excited triplet state, resulting in the formation of radical anions. This process is promoted by high-laser powers and by the presence of reducing agents like thiols, such as β-mercaptoethanol, in an oxygen-free environment. The process of returning to a bright state entails the addition of oxygen to the reduced radical, which brings it back to its original ground state (Soeller & Jayasinghe, 2018). Optimal spatial separation of active fluorophores beyond the diffraction limit is achieved by adjusting the laser intensity, thiol, and oxygen concentrations (van de Linde & Sauer, 2014). Furthermore, in order to achieve nanoscopic resolution, it is also essential to have a sufficient labeling density to ensure accurate spot detection and fitting, depending on the chosen reconstruction software (Small & Stahlheber, 2014). Multiple open-source packages are accessible and provide dependable fitting algorithms. The software ThunderSTORM (Ovesný et al., 2014) was used in this work.

4.2.3. Other Super Resolution Microscopy Methods

Among the large family of SRM techniques, it is worth also mentioning Structured Illumination Microscopy (SIM, Gustafsson et al., 2008), which enables detailed visualization of cellular structures at the nanoscale by using patterned light, creating moiré interference patterns that can later be reconstructed into a super-resolved image (Guerra, 1995). Another innovative approach is Expansion microscopy (ExM, Chen et al., 2015), a technique in which the sample is physically expanded, making structures smaller than the diffraction limit resolvable under conventional microscopes. The next chapter will be dedicated to this novel SRM method.

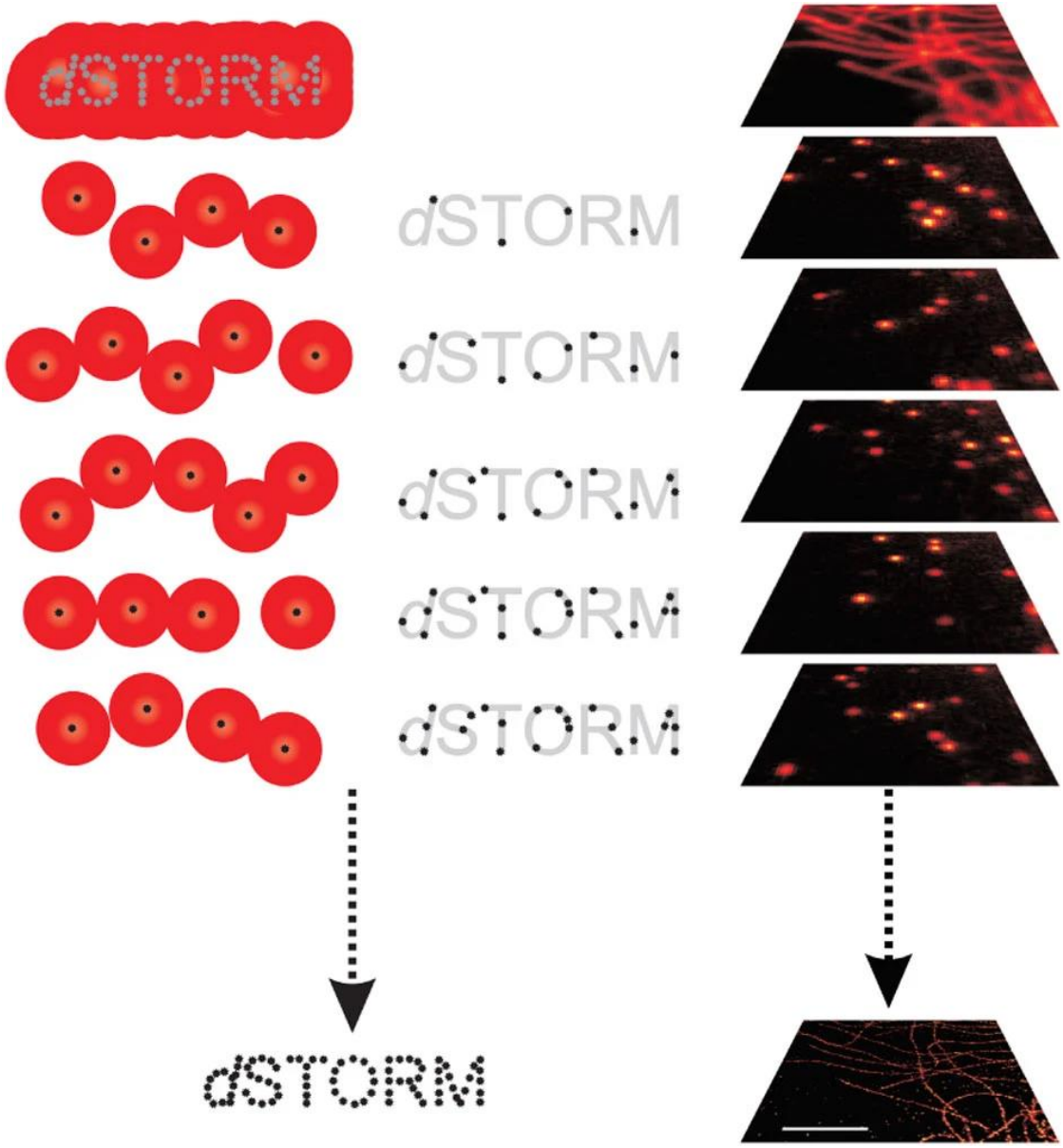

Fig. 12 The dStorm concept. Mammalian cell microtubules labeled with photoswitchable probe. In the initial stage of the experiment, the fluorophores undergo a transition to the OFF state. A small number of fluorophores are then reactivated and spaced out wider than the diffraction limit, allowing for exact localization of their positions. The iterative process allows for the reconstruction of the super-resolved image. Scale bar 2 μm.

Table 1. SRM techniques and their main characteristics

	Confocal	*STED*	*STORM*	*SIM*	*ExM*
WF/Scanning	Scanning	Scanning	WF	WF	WF/Scanning
Concept	Pinhole	Stimulated Emission Depletion	Photo switching Localization	Structured Illumination	Physical magnification
Resolution *xy [nm]*	~200	~30	~20	~100	~60
Resolution *z [nm]*	~600	~130	50-90	~320	~150
Speed	High	Medium	Very Low	Low	Medium
Difficulties		System optimization and complexity	Data reconstruction Stringent choice of fluorophores	Data reconstruction Skilled operator	Sample preparation
Live/Fixed	*Live/Fixed*	*Live/Fixed*	*Live/Fixed*	*Live/Fixed*	*Fixed*
Fluorophores	Conventional	Conventional/high photo stability and depletion efficiency	Photo switchable	Conventional	Conventional
Multicolor	4+	2/3	2/3	4+	4+
3D	yes	hard	yes	yes	yes

5. EXPANSION MICROSCOPY: A PARADIGM SHIFT IN SUPER-RESOLUTION IMAGING

Expansion microscopy stands as a transformative breakthrough in the field of super-resolution imaging, revolutionizing our ability to explore biological structures with an unprecedented level of detail. This innovative method, pioneered by Ed Boyden's research group in 2015 (Chen et al., 2015), is based on the physical expansion of biological specimens, allowing for increased spatial resolution and enhancing our ability to visualize complex subcellular structures using conventional optical setups (Fig. 13).

This method involves infusing biological samples with a high salinity monomer solution (MS) based on sodium acrylate and acrylamide to generate a swellable sodium polyacrylate hydrogel (Fig. 13). The MS also contains a crosslinker like N-N'-methylenebisacrylamide, an initiator such as ammonium persulfate (APS) able to generate free radicals to start the polymerization reaction, and an accelerator like N,N,N',N'-tetramethylethylenediamine (TEMED). For thick biological samples, the addition of the polymerization inhibitor 4-hydroxy-TEMPO (4-HT) facilitates the diffusion of monomers throughout the sample volume before the beginning of the polymerization.

Subsequently, the composite material made of the biological sample embedded and covalently bonded to the hydrogel must undergo mechanical homogenization to achieve

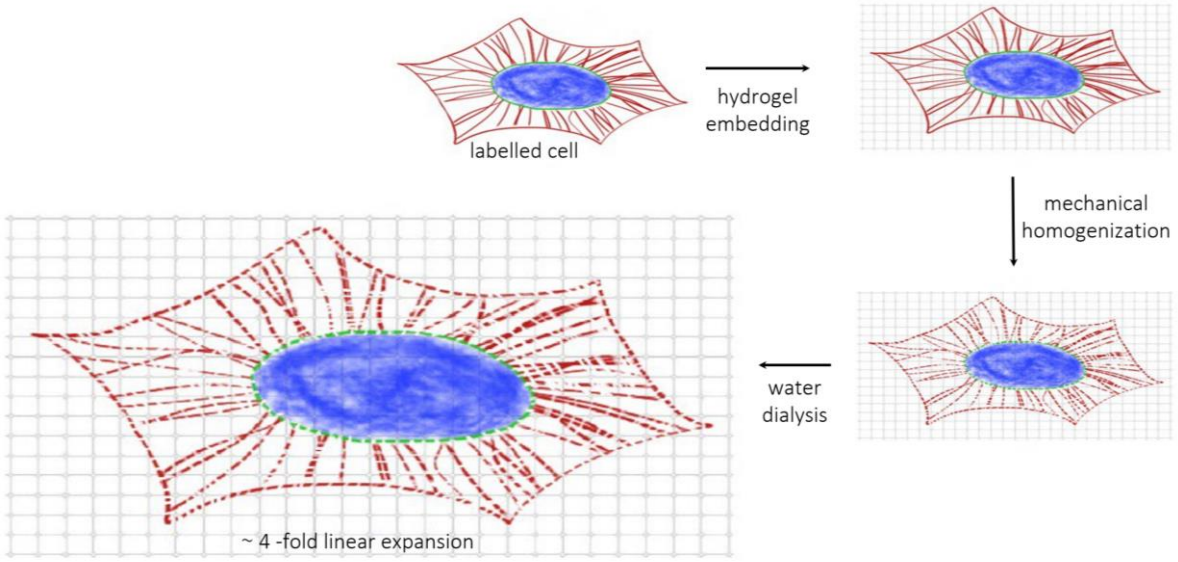

Fig. 13 Schematic representation of the expansion process in ExM.

isotropic expansion. The homogenization of the mechanical properties can be achieved by treating the sample with protease (e.g., proteinase K) or by denaturation with detergents, such as sodium dodecyl sulfate (SDS), at high temperatures. Finally, the proper expansion of the sample is achieved by water dialysis. The sample is washed in deionized water several times to remove the positively charged sodium ions that keep the polymer network in a collapsed state through Coulomb attraction with the negatively charged carboxyl groups of the polymer (Fig. 14). In the first ExM protocol (Chen et al., 2015), the expansion of the polymer leads to a fourfold isotropic magnification of the sample.

The hydrogel is synthesized to form a highly dense matrix around the sample, with a mesh size of roughly 2 nm (Cohen et al., 1992), allowing for the accurate preservation of the relative position of biomolecules within the specimen post-expansion, minimizing distortion and enabling accurate three-dimensional reconstructions (Pesce et al., 2021). The increased size of the sample allows for improved discrimination of molecular features previously beyond conventional microscopy's reach. Considering two biomolecules initially separated by 100 nm, a diffraction-limited confocal microscope with a resolution of ~200 nm would be unable to resolve them. However, after a 4-fold expansion, which increases the distance between the two objects to approximately 400 nm, the confocal microscope can effectively resolve them.

This ability to resolve previously indistinguishable structures with conventional microscopes is the principal advantage of ExM, which, together with its versatility and ease of implementation, makes it a prevalent technique and particularly valuable for imaging

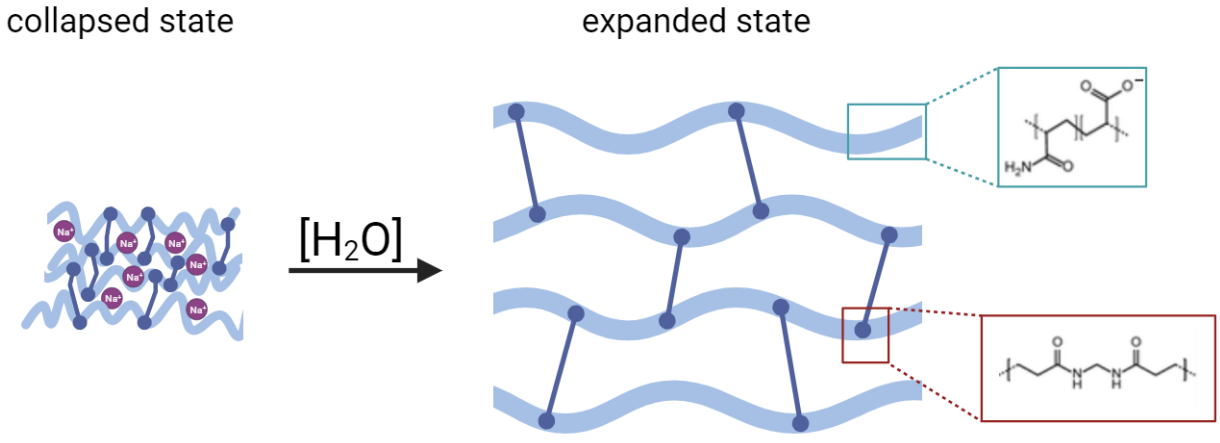

Fig. 14 Schematic illustration of polyacrylate network (green box) expansion due to water dialysis. The crosslinker is shown in the red box. Created with Biorender.com

biological tissues. This groundbreaking technique has become very popular in the last few years, giving rise to multiple developments and adaptations. The following paragraphs will provide a more comprehensive analysis of the available ExM protocols, including their applications, advantages, and disadvantages.

5.1. Protocols

Several versions of Expansion Microscopy techniques have emerged to address various biological challenges. All these techniques are based on the core concept of physically expanding biological samples to enhance the final resolution (Wassie et al., 2019). The different protocols can be categorized into several groups based on the labeling strategy and homogenization process employed during the sample treatment, the achievable expansion factor (EF), the coupling with other super-resolution microscopy methods, and possible applications (Fig. 15).

5.1.1. Pro-ExM

Some of these modifications are developed to allow imaging proteins labeled with conventional antibodies in both in vitro 2D-cell cultures and ex vivo tissue slices. In 2016, Tillberg et al. developed Protein retention ExM (ProExM) to render ExM compatible with commercially available fluorescent labels and ensure a dense bonding of proteins with the expandable polymer matrix, effectively allowing for either pre- or post-expansion staining. ProExM introduced an additional cross-linking step before MS sample infusion, using small molecules such as 6-((acryloyl)amino)hexanoic acid (AcX) or methacrylic acid hydroxysuccinimidyl ester (MA-NHS, Chozinski et al., 2016). Thanks to the presence of the N-hydroxysuccinimide (NHS) ester terminal groups, these molecules covalently bond proteins of the sample and exogenous labels via amide links, leaving free chemical handles for the attachment to the polymer (Lim et al., 2014). For post-expansion staining, the mechanical homogenization step does not include protease digestion. In order to ensure that epitopes remain intact and capable of binding to antibodies after expansion, a more gentle denaturation protocol is used. The potential of post-expansion staining of specimens is the ability to enhance the accessibility of protein complexes, therefore increasing staining density, by decrowding proteins through the expansion process. This method proved successful for most of the antibodies tested, although not every one of them yielded to the

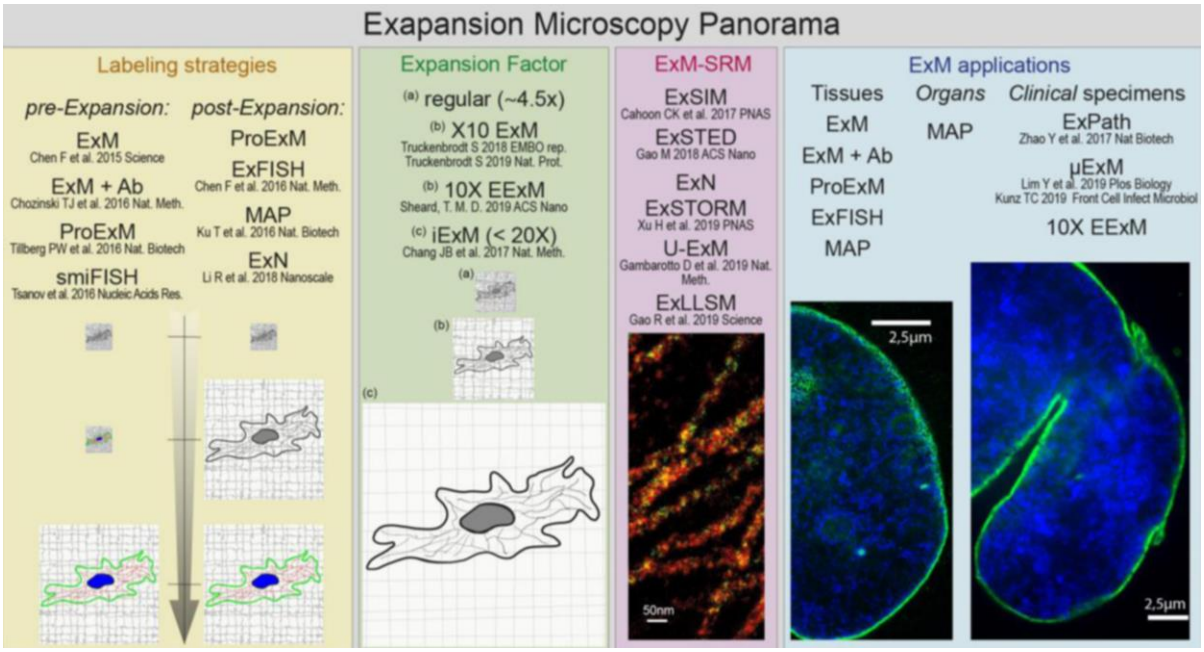

Fig. 15 Overview of available Expansion Microscopy methods grouped depending on different parameters: labelling strategy, achievable Expansion Factor, possible coupling with other super resolution microscopy methods and applications. Reproduced from Pesce et al., 2021

desired results, with some epitopes damaged during the process. In general, the majority of fluorescent labels frequently used with antibodies can be utilized with ProExM, aside from cyanine dyes and bacteriophytochromes-derived infrared fluorescent proteins, which lose their fluorescence during the sample processing.

5.1.2. MAP

The Magnified Analysis of the Proteome (MAP) was developed by Ku et al. in 2016 in order to render ExM compatible with proteomic studies in tissue slices and entire organs. The concept behind MAP is based on the inhibition of cross-linking among native proteins during formaldehyde fixation, achieving four-fold linear expansion after the proteins undergo denaturation.

In order to reduce protein-protein cross-linking, a high concentration of acrylamide, creating covalent bonds with formaldehyde, is added during fixation. The presence of acrylamide serves the additional function of leaving free molecular handles for the gel to anchor to, eliminating the need for an extra cross-linking step. After hydrogel synthesis, the gel-tissue composite is mechanically homogenized using a detergent solution at 95°C, leading to protein denaturation. After water dialysis, the sample is expanded four times, and the process

can be tuned and reversed utilizing buffers of varying salinity. The MAP protocols can be applied to thick biological tissues, such as whole murine organs and tissues (Fig. 16).

The ability of MAP to retain the sample proteome allows the performance of successive cycles of immunostaining using standard antibodies and imaging, enabling 3D super-resolution proteomic studies. Native epitopes preservation led to an 82% success rate of the 122 commercially available antibodies tested in the study.

5.1.3. Other protocols

As seen in Fig. 15, the family of ExM techniques is broad and expanding over time. Some techniques are explicitly developed for specific applications, such as imaging RNAs tagged with fluorescent in situ hybridization probes (ExFISH, Chen et al., 2016), or super-resolution imaging of clinical pathology specimens (ExPath, Zhao et al., 2017). Additionally, some of these protocols were developed to push the achievable resolution even forward by iteratively expanding the sample 10 or more times (iExM, Chang et al., 2017).

Another intriguing possibility is combining multiple protocols for comprehensive biomolecular imaging. A combined approach for RNA visualization and concurrent DNA and protein labeling could have the capability to unveil the structural arrangement of various biomolecular complexes.

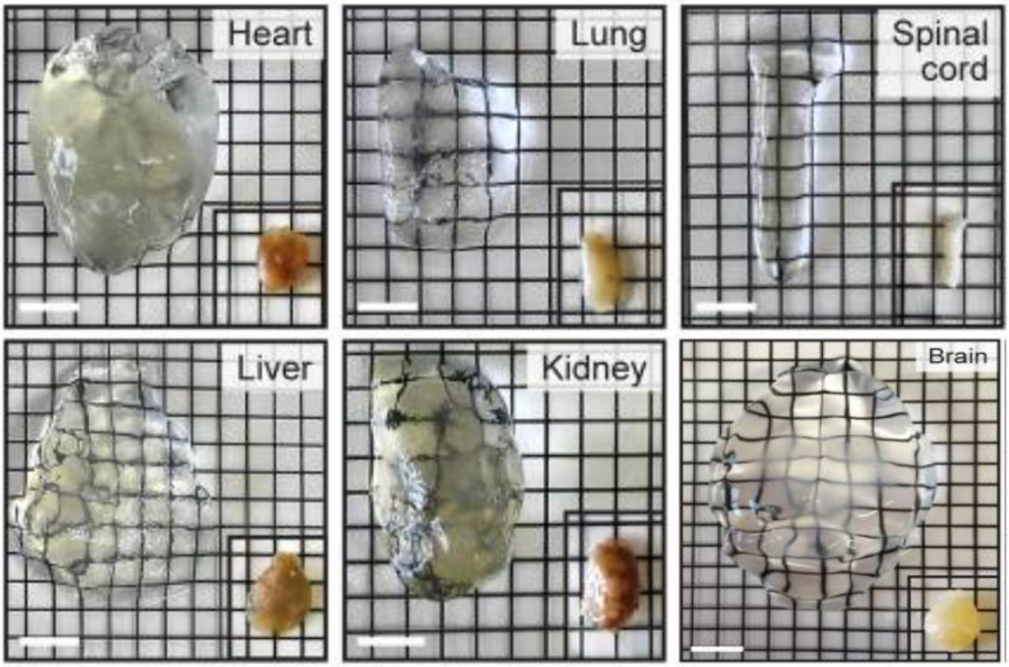

Fig. 16 Magnified Analysis of the Proteome (MAP) applied to entire murine organs. Scale bar 10 mm. Reproduced from Ku et al. 2016

5.2. Expansion Factor measurements and the question of validation

In the context of expansion microscopy, the EF is a critical parameter that quantifies the degree of sample magnification occurring during the process. It is essential to guarantee accurate scaling and interpretation of the experimental data. Nevertheless, the process of quantifying and validating this coefficient can be challenging. In addition, it involves ensuring that the expansion is consistent throughout the sample and does not distort the initial spatial relationships of the biological structures under investigation.

While the EF at a macroscale level can be first approximated by simply measuring the dimension of the hydrogel before and after the expansion (Fig. 18 D), a more thorough validation is needed to corroborate the expansion protocol, especially if the experimental conditions change. This validation is typically performed by comparative analysis between images of a sample before the expansion, possibly visualized using SRM such as SIM or STED, with post-expansion confocal microscopy images of specific structures, often microtubules (Fig. 17). Then, these images are aligned using a non-rigid registration, and distortion analysis is performed using an image processing software such as ImageJ. In most ExM variations, the distortion across the sample was less than 4%, showing a Root Mean Square (RMS) in the order of the PSF of the used imaging method (Chen et al., 2015; Ku et al., 2016; Chozinski et al., 2016).

Although this method proved effective, it requires the ability to image the same cells before and after expansion, making it very time-consuming. Furthermore, this method implies the possibility of performing SRM imaging on the non-expanded sample, which is

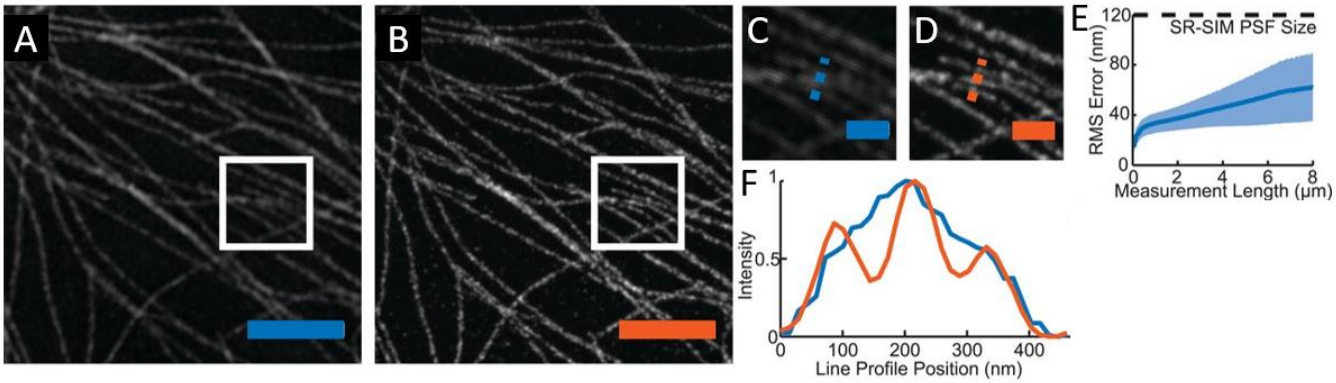

Fig. 17 ExM comparative analysis of HEK293 microtubules. SIM pre-expansion image, scale bar 2 μm (A).Confocal image post-expansion,scabe bar 9.1 μm (B). Magnified box in (A), scale bar 500nm (C). Magnified box in (B), scale bar 2.27 μm (D). Root Mean Square (RMS) error of expanded vs. SIM images (E). Microtubule intensity profiles obtained along the blue and orange dotted lines in images (F) and (G). Adapted from Chen et al., 2015.

not a given for many research laboratories. For these reasons, another possibility is the use of intrinsic reporters for isotropy validation and EF measurements.

In 2019, Pesce et al. exploited the NPC's well-characterized and preserved symmetry and dimension to use it as an intrinsic reporter. The NPC possesses an octagonal symmetry around the transport axis and a pseudo-planar symmetry across the nuclear envelope surface. In addition, both the internal and external diameters of the transport channel are known, being respectively ~120 and ~45 nm in humans (Lin & Hoelz, 2019). In their work, Pesce et al. labeled the Nup153 subunit of the NPC in HEK293T cells and combined ExM and STED microscopy (ExSTED, Gao et al., 2018, Fig. 18 A). They statistically measured the angular difference among the single Nup subunits (Fig. 18 B), finding it to be a multiple of 45° within the error (Fig. 18 C) and confirming the isotropy of the expansion process. Then, they determined the EF at the nanoscale by measuring the pore radius before the expansion, after the protease digestion, and after the expansion (Fig. 18 D). Finally, they compared the macroscale EF, measured on the gel diameter variation during expansion, with the nanoscale one, finding a good correlation between the two coefficients therefore confirming the validity of the macroscale EF calculation.

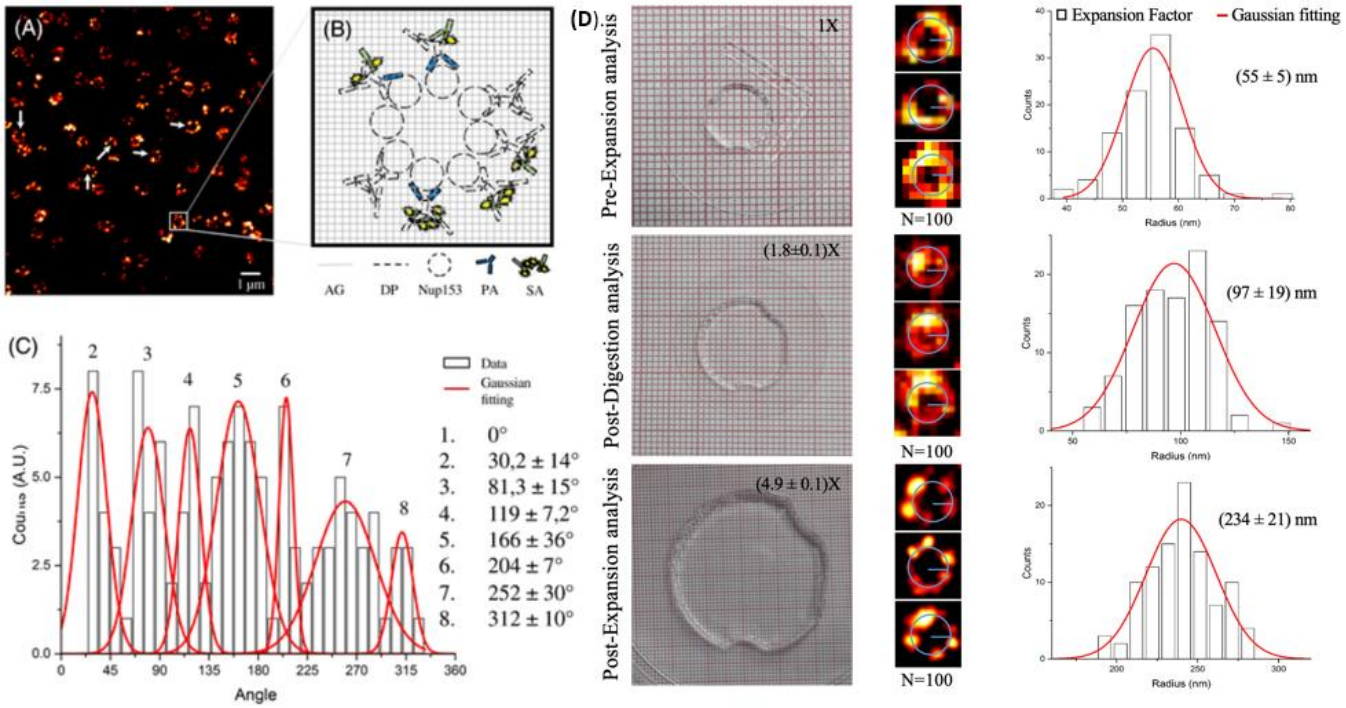

Fig. 18 Expansion isotropy determination using the NPC. STED post-expansion image of HEK293T Nup153, scale bar 1 µm (A) Schematic representation of Nup153 subunit symmetry and interaction with labels and gel monomers (B). Angular difference among the single Nup subunits and the reference one at 0° (C). EF measurement radius at the macro- and nanoscale before expansion, after digestion, and after expansion (D). Adapted from Pesce et al., 2019.

A similar approach was used by Gambarotto et al. in 2021, who developed Ultrastructure Expansion Microscopy (U-ExM). This technique is specifically designed to retain the ultrastructure of centrioles and was validated using dSTORM to compare the ninefold symmetry of non-expanded isolated centrioles with the expanded ones.

5.3. Advantages and disadvantages

In the previous sections, we have presented an overview of different ExM protocols and their current directions. Now, we will discuss its fundamental capabilities and limitations.

Besides the aforementioned advantage of offering nanoscale-resolution imaging using diffraction-limited microscopes, ExM provides several notable technical advantages. These include the capability to perform 4-color multiscale SRM imaging of thick specimens with the most cost-effective methodology compared to other super-resolution techniques. Furthermore, ExM naturally clears the sample with a hydrogel primarily composed of water, almost entirely homogenizing its refraction index and making it transparent and free from optical aberrations (R. Gao et al., 2017). Additionally, the tunability of the EF and the possibility to perform iterative processes of expansion, together with the combinability with other SRM methods, open the road to unprecedented optical resolutions.

The main drawback of ExM is its incompatibility with live sample imaging, making it incompatible with the study of dynamic biological processes. Being an almost entirely sample preparation-based technique, ExM can be time-consuming, especially for thick samples, with infusion times lasting up to a week (Ku et al., 2016). Furthermore, the heavy sample processing involved in this technique can lead to a significant loss of fluorescent signal, lowering the signal-to-noise (SNR) of the imaging and creating the need for protocol optimization for each protein under investigation. Finally, although the expansion achieved through ExM results in minimal distortions, as supported by various isotropy measurements, validation is required whenever the protocol is modified.

Overall, ExM techniques offer remarkable imaging capabilities. Nevertheless, they are limited by practical constraints and need careful handling of the samples.

6. MATERIAL AND METHODS

6.1. Cell culture, seeding and fixation

Both the HEK 293T and HeLa cell lines were cultured in high glucose Dulbecco's Modified Eagle's Medium (DMEM, Sigma-Aldrich), which was supplemented with 10% Fetal Bovine Serum (Euroclone) and 1% Penicillin-Streptomycin (Life Technologies). MCF-10A cells were cultured in DMEM: Ham's F12K (1:1) (Sigma-Aldrich), which was supplemented with 5% Horse Serum (Euroclone), 1% Penicillin-Streptomycin (Life Technologies), 2mM L-Gltamine, 50 ng/mL Cholera Toxin (Sigma-Aldrich), 10 µg/mL Insulin (Sigma-Aldrich), 0.5 µg/mL Hydrocortison (Sigma-Aldrich) and 20 ng/mL of human Epidermal Growth Factor (Sigma-Aldrich). All cells were subcultured in T-75 flasks and incubated at 37°C in 5% CO_2.

For ExM, confocal and STED microscopy cells were seeded on 18 mmmm 1.5H high precision coverslips treated with a 0.01% poly-L-lysine solution (Sigma-Aldrich) in 12-well plates. For dSTORM imaging, cells were seeded in 8-well glass bottom chamber slides (ibidi GmbH). In all cases, cells were fixed at ~80% confluence with 4% formaldehyde (FA)solution at room temperature for 10 minutes and rinsed three times with Phosphate-Buffered Saline (PBS, Sigma-Aldrich).

6.2. Bacteria transformation and transfection

The transformation of two plasmids encoding eGFP- Wild Type Lamin A and eGFP-LAΔ50 (Addgene, Scaffidi & Misteli, 2005), for LMNA 1824 C>T gene mutation, into competent bacteria, using Kanamycin selective agar plates (Fig. 19) was carried out through a heat shock (15 min at 0°C, 1 min at 42 °C). The NucleoBond Xtra Midi kit (Macherey-Nagel) was used for DNA plasmid purification. The DNA was then quantified by measuring its absorbance at 260 nm using the NanoDrop spectrophotometer (Thermo Scientific). For transient transfections, HEK293T seeded on 18 mm coverslips were transfected using Effectene Transfection Reagent (Qiagen) and fixed with 4% FA solution after a 24 h incubation.

In order to develop a cellular model of HGPS for further experiments, a stable HEK293T

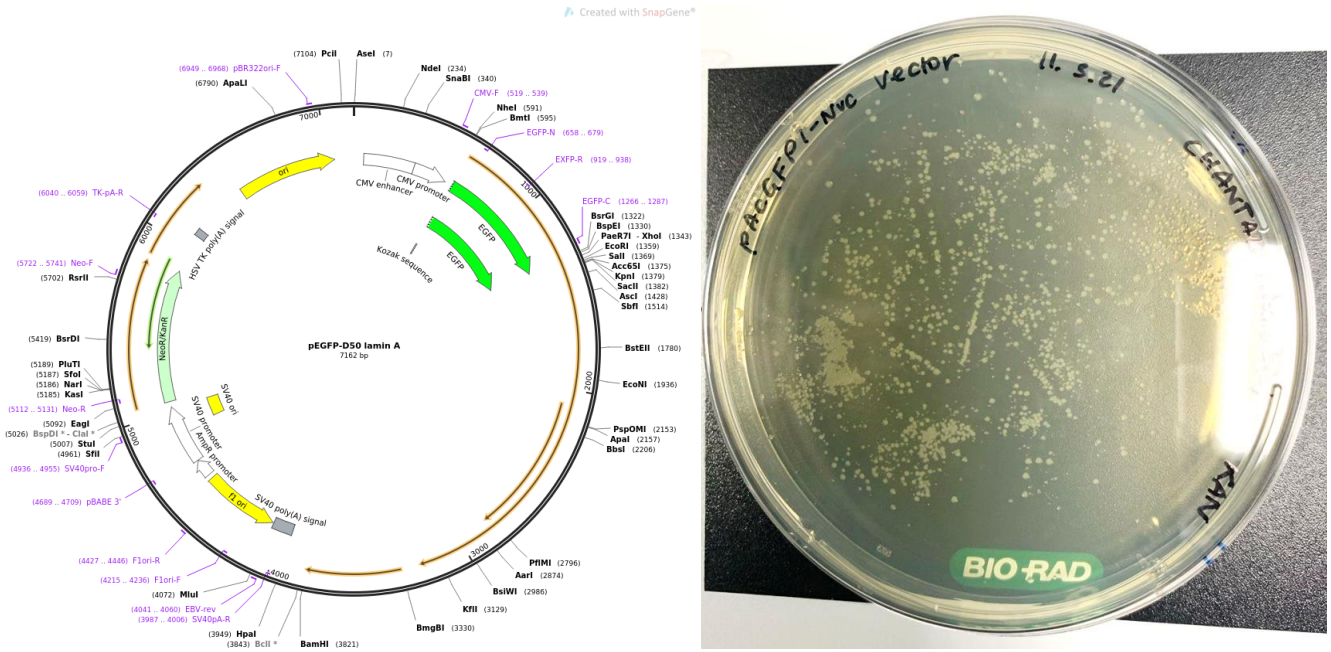

Fig. 19 Schematic representation of a plasmid encoding for LMNA 1824 C>T gene mutation. Adapted from Scaffidi & Misteli, 2005. (left). Bacteria transformation on agar plate (right).

cell line expressing eGFP-LAΔ50 was selected using G418 0.9 mg/ml. Finally, eGFP-positive cells were separated with Fluorescence-activated Cell Sorting (FACS SH800, Sony) using a 487 nm laser and a 524/50 BP emission filter and then subcultured for imaging and biomolecular essays. Unless otherwise specified, non-transfected HEK293T cells were used as a control group (CTRL) in this thesis work.

6.3. Immunostaining and DNA labeling

For all fluorescence microscopy experiments, following the FA fixation process, the cells were blocked and permeabilized for 1 hour at room temperature using a Blocking Buffer (BB) solution composed of PBS supplemented with 5% Bovine Serum Albumin (BSA, Sigma Aldrich) and 0.5% Triton X-100 (Sigma Aldrich). For indirect immunostaining, the cells were incubated overnight at 4°C with the primary antibodies diluted in BB. The next day, cells were washed three times for 10 min in a Washing Buffer (WB), composed of BB diluted in PBS 1:10, and then incubated with the secondary antibodies solution in BB at room temperature for 1 hour. Subsequently, cells were washed in WB thrice for 10 min, followed by three 5-min washes in PBS. When needed, DNA counterstaining was performed by subsequently incubating the label in PBS at room temperature for 20 min. All the labels and antibodies used in this work with their concentrations can be found in Table 2.

Table 2. List of labels and antibodies used in this work for fluorescence microscopy

	Type	*Host/target*	*Abs/Em [nm]*	*Dilution from stock solution*	*Brand*
Hoechst33342	DNA stain	-	355/465	1:2000	Everbright
SPY650-DNA	DNA stain	-	652/674	1:500	Spirochrome
SiR-DNA	DNA stain	-	652/674	1:500	Spirochrome
H3K9me2 - Ab1220	Primary antibody	Mouse	-	1:200	Abcam
H3K9ac - 710293	Primary antibody	Rabbit	-	1:200	Invitrogen
Nup153 - Ab84872	Primary antibody	Rabbit	-	1:100	Abcam
Nup107 - MA1-10031	Primary antibody	Mouse	-	1:100	Invitrogen
PCNA - MA5-11358	Primary antibody	Mouse	-	1:50	Invitrogen
PRR14 - PA5- 65696	Primary antibody	Rabbit	-	1:30	Invitrogen
HP1α - MA1-218	Primary antibody	Mouse	-	1:200	Invitrogen
RNApol2se2 - 61083	Primary antibody	Rabbit	-	1:500	Active Motif
γH2AX - PA5-77995	Primary antibody	Rabbit	-	1:1000	Invitrogen
Tubulin ß - Ab6046	Primary antibody	Rabbit	-	1:200	Abcam
Atto 532	Secondary antibody	Mouse/Rabbit	532/553	1:200	Atto-Tec
Atto 594	Secondary antibody	Mouse/Rabbit	601/626	1:200	Atto-Tec
Atto 647N	Secondary antibody	Mouse/Rabbit	644/669	1:200	Atto-Tec
Abberior Star 580	Secondary antibody	Mouse/Rabbit	587/607	1:100	Abberior
Abberior Star Red	Secondary antibody	Mouse/Rabbit	638/655	1:100	Abberior
Alexa Fluor 488	Secondary antibody	Mouse/Rabbit	494/517	1:250	Invitrogen
Alexa Fluor 647	Secondary antibody	Mouse	648/671	1:250	Invitrogen

For STED and confocal imaging, the coverslips containing the labeled cells were then mounted on a microscope glass slide using ProLong™ Diamond Antifade Mountant (Life Technologies) and left to polymerize overnight in the dark at room temperature prior to imaging. Labeled cells were kept unmounted for ExM and dSTORM experiments to proceed with the subsequent steps.

The labeling of nascent DNA replication sites using 5-ethynyl-2'-deoxyuridine (EdU) was performed using the Click-iT™ EdU Imaging Kit with Alexa Fluor 594 Azide (Invitrogen). 10 μM EdU was introduced in the culture media of ~80% confluent seeded cells and incubated for 25 minutes at 37°C in 5% CO_2. Subsequently, cells underwent regular FA fixation protocol. The click reaction with Alexa Fluor 594 Azide was carried out according to the manufacturer´s instructions. In order to use the same reagents to label all DNA instead of only the nascent one, the same protocol was followed, with the sole difference that seeded cells were, in this case, left to incubate with EdU for 24 hours prior to fixation.

6.4. Expansion Microscopy

In this work, the expansion microscopy protocol developed by Chozinski et al. to render ExM compatible with conventional antibodies and the ProExM protocol developed by Tillberg et al. in 2016 were both initially tested.

For the Chozinski protocol, a 25 mM solution of MA-NHS in PBS was used as a cross-linker. Labeled cells plated on coverslips were incubated for 1 hour at room temperature. For the ProExM technique, the AcX (0.1 mg/mL in PBS) cross-linker was used on labeled cells and left to incubate for three hours at room temperature. The subsequent steps proceed in the same way for both protocols.

After cross-linking, the samples were washed three times in PBS for 10 min. The polymerization chamber was built by attaching a 9 mm diameter (d_i), 0.12 mm deep Secure-Seal spacer (Invitrogen) onto a Parafilm sheet inside a glass petri dish. The chamber was then filled with the MS (composed of sodium acrylate 8.6%, acrylamide 2.5%, N-N'-methylenebisacrylamide 0.15%, NaCl 2M, 8.6% TEMED, 2.5% APS in PBS), and the coverslip was used as a chamber lead with the cells facing the MS. The solution was kept on ice, and TEMED and APS were supplemented immediately before infusing the sample. The

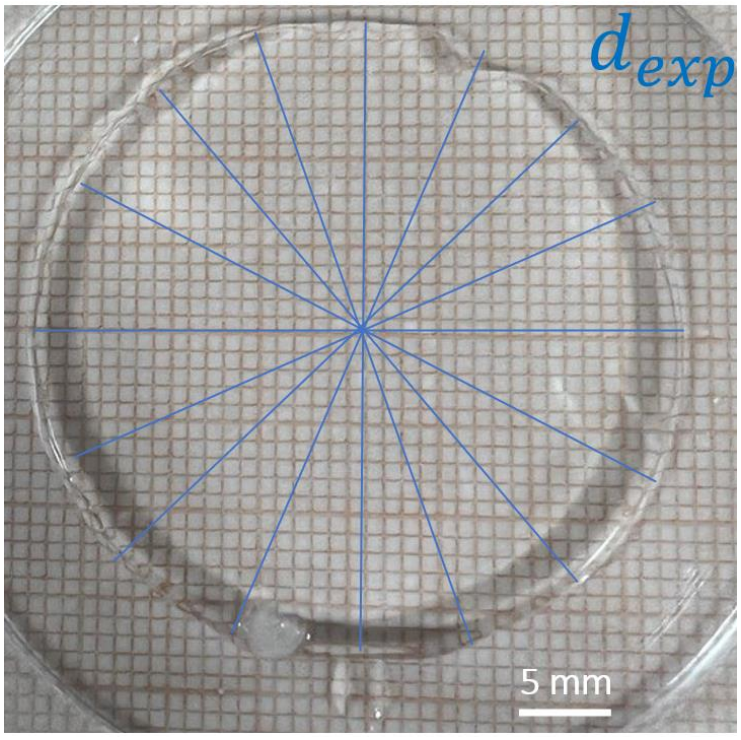

Fig. 20 Fully expanded hydrogel with embedded cells on a graph millimeter grid. The blue lines represent line profiles along different orientations to calculate the expanded diameter d_{exp}.

specimen was then incubated for 1 hour at 37°C to ensure complete gel polymerization. The hydrogels were subsequently incubated with a Digestion Buffer (DB, composed of Triton X-100 0.5%, NaCl 1M, disodium EDTA, and Tris-Cl to reach pH=8) supplemented with Proteinase K 8 U/mL right before adding it to the sample. The digestion proceeded for 30 min at 37°C. Finally, the gels were allowed to fully expand in DI water, with 3x20 min immersion at room temperature.

In order to calculate the macroscale EF, the fully expanded gels were imaged on a graph millimeter grid (Fig. 20), and then multiple line profiles along different orientations were measured using ImageJ to measure the expanded gel diameter d_{exp}. Finally the EF was calculated as:

$$EF = \frac{d_{exp}}{d_i} \tag{6.1}$$

6.4.1. Restaining of secondary antibodies and DNA labels after expansion

In order to compensate for the loss of fluorescence signal due to the expansion process and the protease digestion, the secondary antibodies were restained (2ABR) after the expansion in some cases. The ability of this process to effectively increase the fluorescence

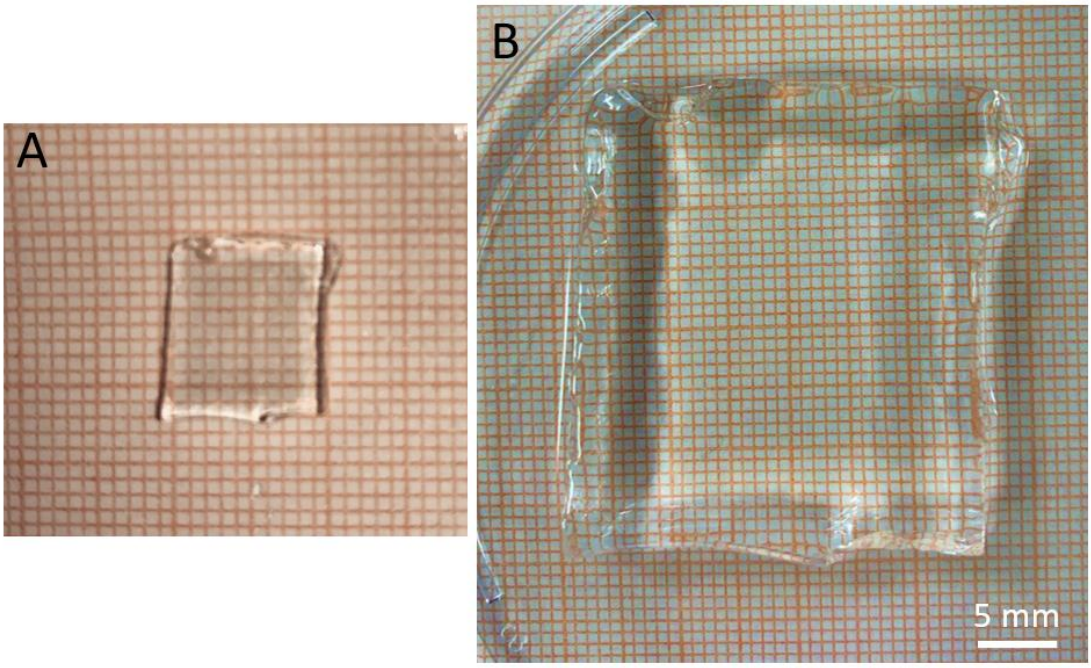

Fig. 21 Secondary antibodies restaining (2ABR) of cut gel portion on a graph millimeter grid. Shrunk gel after immersion in blocking buffer (A). Fully expanded hydrogel (B).

signal is based on the native sample epitope and the primary antibody´s survival to the digestion process. For this reason, the 2ABR succeeded in increasing the SNR and the Signal to Background ratio (SBR) of some target proteins, like Nup153, but not others, like PRR14. In order to test this new protocol, pieces of the expanded gel were cut and incubated in BB for 1 hour at room temperature. Subsequently, the partially shrunk gels (Fig. 21 A) were incubated with the secondary antibodies in BB for 2 to 3 hours to let the labels diffuse inside the volume of the gel. After three 20-minute washes in WB, the gels were left to re-expand in DI water thrice for 20 min until full expansion (Fig. 21 B). When needed, a fluorescent DNA probe was added at this point by supplementing the probe at the desired concentration in the last DI water immersion, which was prolonged for 1 hour at room temperature or overnight at 4°C.

6.4.2. Sample mounting

Stained and fully expanded hydrogels were cut into squares and mounted between two 24 mm × 50 mm, 0.17mm thickness high precision glass coverslips (Corning) using Picodent Twinsil (Picodent) silicon resin (Fig. 22 A). This mounting agent creates a sealing around the gels, effectively preventing dehydration, which would lead to shrinking during sample imaging. In addition, using this method, the sample can be imaged from both sides

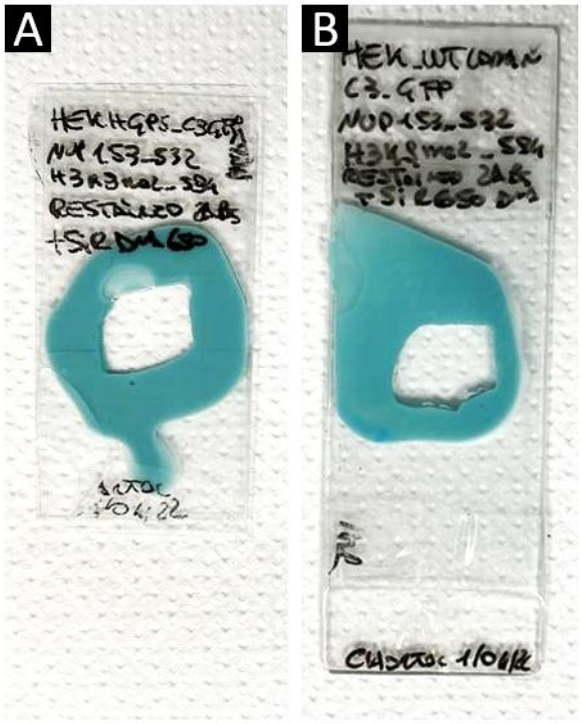

Fig. 22 Mounted expanded samples. Sample mounting between two 24 mm × 50 mm, 0.17mm thickness coverslips (A). Mounted sample taped to a traditional microscope slide to increase imaging stability (B).

to understand which one is closer to the cells. Due to the gel thickness and the limited objective working distance, it is not always possible to image the cells from both sides of the sample. Finally, once the correct imaging side is found, the sample can be mounted onto a thicker glass slide on the non-imaging side using tape to increase imaging stability and ensure better fitting in the microscope sample holder (Fig. 22 B).

6.5. Optical Microscopy

6.5.1. Confocal

Confocal imaging was performed using a Leica TCS SP5 gated STED-CW microscope (Leica Microsystems). The microscope is equipped with a White Light Laser (WLL) 470 - 670 nm laser. Imaging was conducted using a 100×, 1.4 NA oil immersion objective (Leica Microsystems). The pinhole size was adjusted to 0.9 airy unit (AU). The

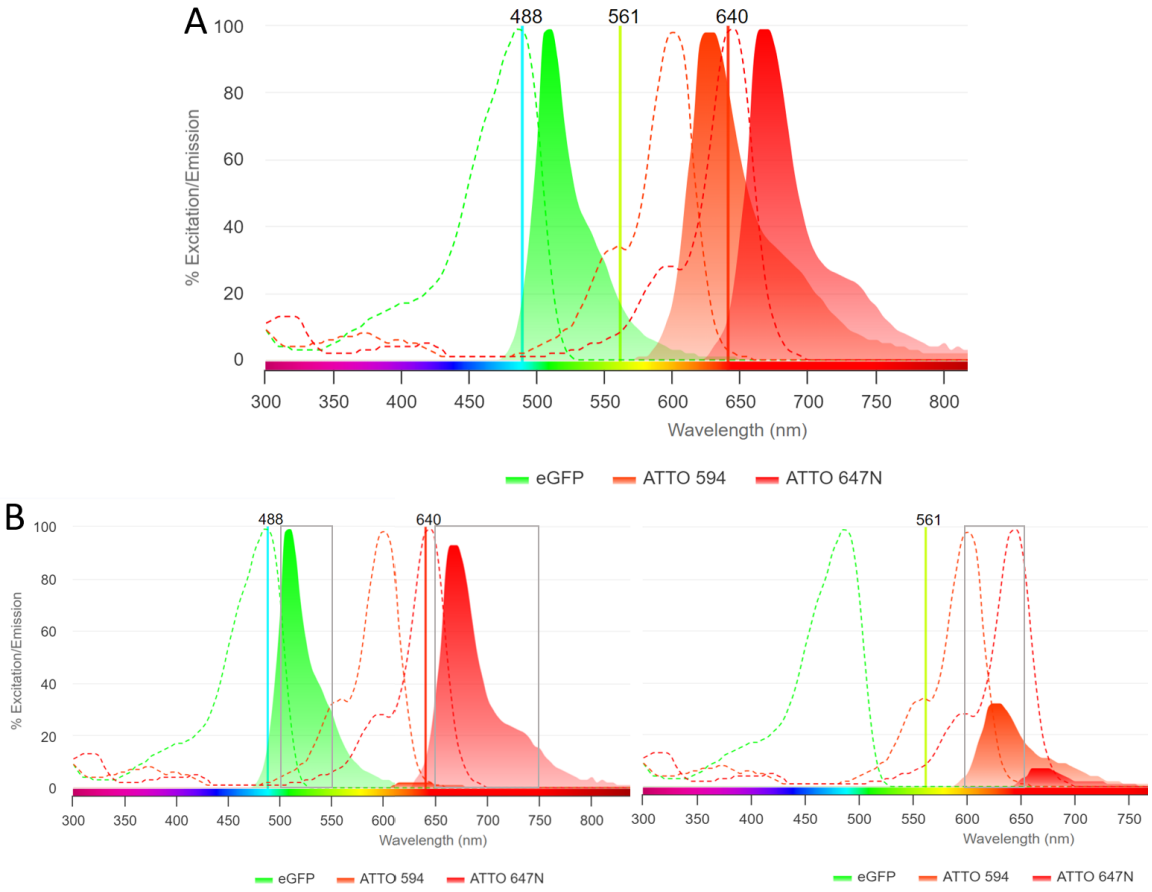

Fig. 23 Example of fluorescence microscopy multi-color experiment design. For each fluorophore, the dotted profile represents the absorption spectra, while the solid-colored profile denotes the emission one. The solid lines indicate the excitation lasers (466, 561, and 640 nm). Combined fluorophore spectra (A). Line separation to avoid signal cross-talking, the grey boxes represent the detection windows (B). Created using https://app.fluorofinder.com.

Table 3. Excitation and acquisition parameters used in this work for confocal imaging

Fluorophore	*Excitation line [nm]*	*Notch filter band-stop [nm]*	*Detection window [nm]*
eGFP	488	488/10	500-550
Alexa Fluor 488	488	488/10	500-550
Atto 532	514	514/10	542-600
Atto 594	561	561/10	600-650
Atto 647N	640	640/10	650-750
Abberior Star 580	561	561/10	600-650
Abberior Star Red	640	640/10	650-750
SPY650-DNA	640	640/10	650-750
SiR-DNA	640	640/10	650-750

acquisition was carried out at 1000-1400 Hz, with 32-64 line repetitions, and the pixel size used was 75 nm. Different combinations of fluorescent dyes were tested in this work, and the experiment was specifically designed for each multi-color combination (Fig. 23 A). When necessary, the signal was captured sequentially line by line to avoid cross-talking between different channels (Fig. 23 B). For each fluorophore used, the excitation laser wavelength, the Notch filter band-stop, and the detection window of the Leica HyD hybrid detectors can be found in Table 4.

6.5.2. STED

The STED experiments were performed using a Leica STELLARIS 8 STED microscope (Leica Microsystems) with WLL 440 - 790 nm excitation and a 775 nm depletion laser. The four-color experiments proceeded as follows: Hoechst33342, eGFP, Abberior Star 580, and Abberior Star Red were respectively excited at 440 nm, 488 nm, 561 nm, and 640 nm. The detection windows used for the Leica hybrid HyD detectors were respectively 440-500 nm, 500-550 nm, 600-650 nm, and 650-700 nm, with sequential acquisition line by line. Each acquisition was performed both in confocal and STED mode, with a pixel size of 25 nm. For the 561 nm and 640 nm lines, the 2 W 775 nm depletion laser was activated during STED acquisition with 30% power. The two Abberior dyes were selected for their high efficiency with a depletion laser wavelength between 750 - 800 nm. The TauSTED imaging modality of Leica STELLARIS 8 was used for image rendering of these two red colors. This imaging mode exploits the software TauSense (Roberti et al., 2020), which pushes forward the concept of gated STED by analyzing for each pixel the arrival times of photons and uses this lifetime information to obtain a more precise selection of signal and background photons, generating a high SNR image.

The optical resolution was calculated using the Fourier Ring Correlation (FRC) feature of the BIOP (Nieuwenhuizen et al., 2013) plugin of ImageJ using the Fixed 1/7 threshold method (Fig. 24 B). The resolution at 647 nm using the 775 nm depletion laser, calculated on the two subsequently collected images in Fig. 24 A, resulted to be 124 nm for the STED imaging and 232 nm for the confocal one.

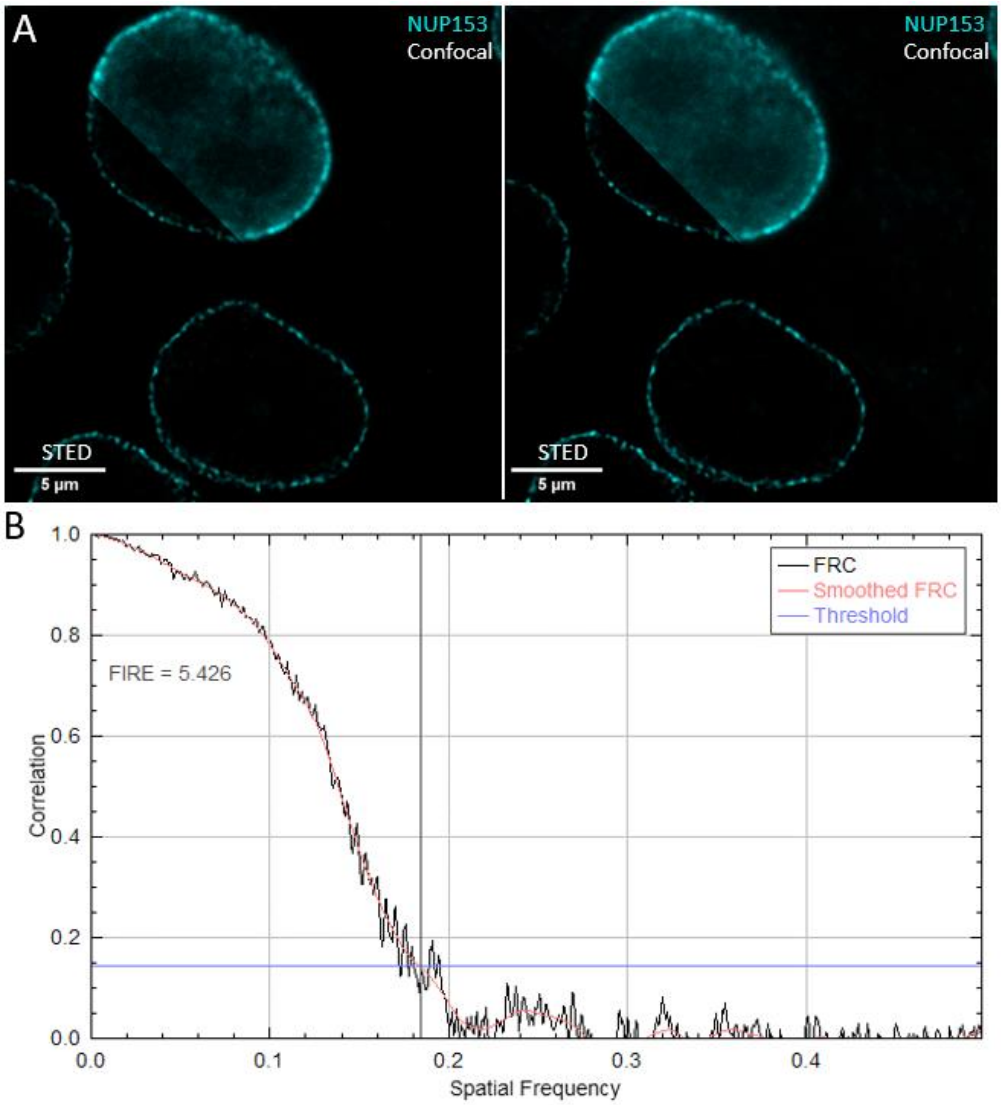

Fig. 24 Optical resolution calculation using the Fourier Ring Correlation (FRC) method of the BIOP plugin of ImageJ. Subsequently collected images of HEK 293T immunostained for NUP153 and labeled with Abberior Star Red (A). Plot of the FRC courve for the STED resolution determination at 647 nm .

6.5.3. STORM

In this work, all the 3D-dSTORM acquisitions were conducted using the Nikon N-SIM N-STORM Super-Resolution Microscope (Nikon Instruments) with a 100×, 1.49 NA oil immersion objective (CFI SR HP Apochromat TIRF 100XAC Oil, Nikon Instruments). The z calibration was performed using 100 nm TetraSpeck™ Fluorescent Microspheres (Invitrogen), mounted on an 18 mm coverslip using poly-L-lysine and ProLong™ Diamond Antifade Mountant. In order to perform drift correction using fiducial markers, 150 nm Gold Nano Particles (GNPs, Sigma Aldrich) were added to the samples before imaging. Subsequently, the ibidi wells containing the immunostained cells were filled with the STORM imaging buffer Abbelight Smart Kit (Abbelight) to induce optimal Alex Fluor 647 photoswitching and sealed using Parafilm to reduce Oxygen exchange. For each field of view imaged, 60.000-80.000 frames were captured with an exposure time of 20 ms, using the Nikon Perfect Focus System and an illumination incident angle $\theta = 60°$. The excitation laser wavelength of 647 nm was selected using the microscope dichroic mirrors (ZET405/488/561/647; Chroma), while the signal detection was selected using the quad band emission filter (ZT405/488/561/647, Chroma). A low-power activation laser with a wavelength of 405 nm was used during the entire acquisition. Laser intensities at the objective, assessed using an optical power meter (Thorlabs), were 58.6 mW for the 647 nm excitation line and 1.5 mW for the 405 nm activation line, corresponding to an illumination density of 9.4 kW/cm^2 and 1.5 kW/cm^2, respectively. Image detection utilized a Complementary Metal-Oxide-Semiconductor camera (CMOS Orca-Flash 4.0 C13440, Hamamatsu). The ImageJ plugin ThunderSTORM (Ovesný et al., 2014) was used for single-molecule fitting and localization from the collected dSTORM stacks, using the GNPs signal to correct xy image drifting. The localizations were filtered by uncertainty_xy<100 or uncertainty_z<500. The rendered maps were constructed using Gaussian functions centered on each localization, with a sigma value corresponding to the obtained localization precision of 20 nm.

6.6. Western Blot

For each group (HGPS and CTRL), 0.5×10^6 FACS-sorted pelleted cells were resuspended in 100 µl of RIPA Buffer (Bio-Rad Laboratories) enriched with 1:100 protease inhibitor on ice and then subjected to three 10-second rounds of sonication to eliminate all DNA and RNA. The samples were then supplemented with Laemmli Sample Buffer (Bio-Rad Laboratories) enriched with β- mercaptoethanol (Sigma-Aldrich) was added to the samples, and subsequently incubated for 5 min at 96°C, followed by storage on ice. For each sample, 15 µl of the total cellular protein extract was concurrently loaded onto a NuPAGE 10% Bis-Tris Gel (Invitrogen). A PageRuler Plus Protein Ladder (Thermo Scientific) served as a reference standard. Following electrophoresis separation using NuPAGE MOPS SDS Running Buffer (Novex, Life Technologies), the proteins were transferred onto nitrocellulose membranes using Trans-Blot Turbo Transfer Buffer (Bio-Rad Laboratories) and Trans-Blot Turbo Transfer Stacks (Bio-Rad Laboratories). Afterward, they were rinsed with Milli-Q water and exposed to Ponceau S total protein staining (Thermo Scientific Subsequently, the membranes were sectioned to isolate the target proteins, rinsed in Tris-buffered saline with Tween 20 (TBST), and blocked using a 5% solution of nonfat dried milk powder (PanReact ITW Reagents) in TBST for 1 hour. The membranes were subjected to overnight incubation with primary antibodies at 4°C (see Table 4), followed by 3 washing of 5 min in TBST. Subsequent incubation with secondary antibodies (see Table 4) in 5% milk occurred for 1 hour at room temperature. Following another series of three 5-minute washes in TBST, the membranes were exposed to ECL Western Blotting Substrate (Abcam) for 3 min at room temperature. The protein blots were visualized utilizing the ChemiDoc MP chemiluminescence detection system (Bio-Rad Laboratories), with subsequent image analysis conducted using the Gel feature of ImageJ.

Table 4. List of primary antibodies used in this work for Western Blot

Name	*Host/target*	*Dilution from stock solution*	*Brand*
Lamin A - AB8980	Mouse	1:1000	Abcam
Progerin – AB66587	Mouse	1:1000	Invitrogen
Actin	Mouse	1:10000	Invitrogen
PRR14 - 22819-1-AP	Rabbit	1:1000	Proteintech
HP1a - MA1-218	Mouse	1:200	Invitrogen
H3K9me2	Mouse	1:200	Abcam
H3k9ac - 710293	Rabbit	1:1000	Invitrogen
RNApol2s2 - 61083	Rat	1:500	Active Motif

6.7. RNA extraction and real-time q-PCR

Cellular total RNA extraction was conducted for the HGPS and CTRL group using the Quick-RNATM Miniprep Kit (ZYMO Research). The isolation of cellular total RNA was performed with Trizol reagent (Invitrogen). In order to quantify mRNA expression levels, four technical replicates were carried out for quantitative real-time PCR (qPCR) using the 1x IQTMSybrGreen SuperMix and the Chromo4TM System equipment (Bio-Rad Laboratories). The primer pairs were designed based on human coding sequences and can be found in Table 5.

6.8. Global genomic DNA methylation analysis

For each group (HGPS and CTRL), 5×10^6 live cells were isolated from the culturing media through centrifugation inside 1.5 mL Eppendorf tubes. The pellets were then rinsed in PBS and stored at -80°C. Upon thawing, the cell pellets underwent lysis in PBS and incubation with 20mg/ml Proteinase K to eliminate nuclease contamination. Genomic DNA was isolated utilizing the GeneAll ExgeneTM Cell SV mini kit (GeneAll Biotechnology Co. Ltd) under the manufacturer's instructions. The quality and quantity of the extracted DNA were evaluated at 260 nm through spectrophotometric analysis employing the Varian Cary50 spectrophotometer (Agilent).

For the assessment of the global genomic DNA methylation levels of HGPS and CTRL groups, the MethylFlash™ Global DNA Methylation (5-methylcytosine, 5-mC) ELISA Easy Kit (Epigentek) was employed, following the manufacturer's protocol. In order to ensure accurate and precise quantification, a standardized 100 ng input of DNA was employed for each essay, with four technical replicates conducted for both CTRL and HGPS groups.

Table 5. List of primer pairs used for real-time q-PCR

Primer Name	*Primer Sequence 5' - 3'*	*Annealing T [°C]*	*Accession ID*
GAPDH Fwd	ACCCACTCCTCCACCTTTGACGC	60°C	DQ403053
GAPDH Rev	CTCTTGTGCTCTTGCTGGGGCTG		
DNMT1 Fwd	TGGCTTTGAGAGTTATGAGG	60°C	NC_000082.6
DNMT1 Rev	GGGTCATCATCATAGATTGG		
EHMT2 Fwd	TCAGAGGAGTTAGGTTCTGC	60°C	NC_000072.6
EHMT2 Rev	AGCTTCAACTTCAGACTTGC		
KAT2A Fwd	GTCTGTTCACAAGGAAGAGG	56°C	NC_000077.7
KAT2A Rev	GCAAGAACATCTTTGAGAGC		

6.9. Data analysis

6.9.1. Distance analysis

Average Lamin-Chromatin distance h

The first method to determine the Lamin-Chromatin distance was based on the analysis of the two signal intensity profiles at their interface at the nuclear periphery. For each set (N=15), expanded cells (ProExM) confocal imaging was performed at the equatorial plane. ImageJ software was then used to draw equally distributed line profiles on each cell (N=20) perpendicular to the tangent of the lamin signal (Fig. 25 A), and the intensity profiles were acquired using the Plot Profile function. The intensity profiles of WT Lamin A (CTRL set) or LAΔ50 (HGPS set) signals and the DNA signals were exported and interpolated as Boltzmann sigmoids using the software Origin (OriginLab Corporation), and the Lamin-Chromatin distance h was calculated as the distance between the two sigmoids flex points (Fig. 25 B). Finally, the data were normalized on the EF=4.0±0.1 and analyzed using the software Prism (GraphPad).

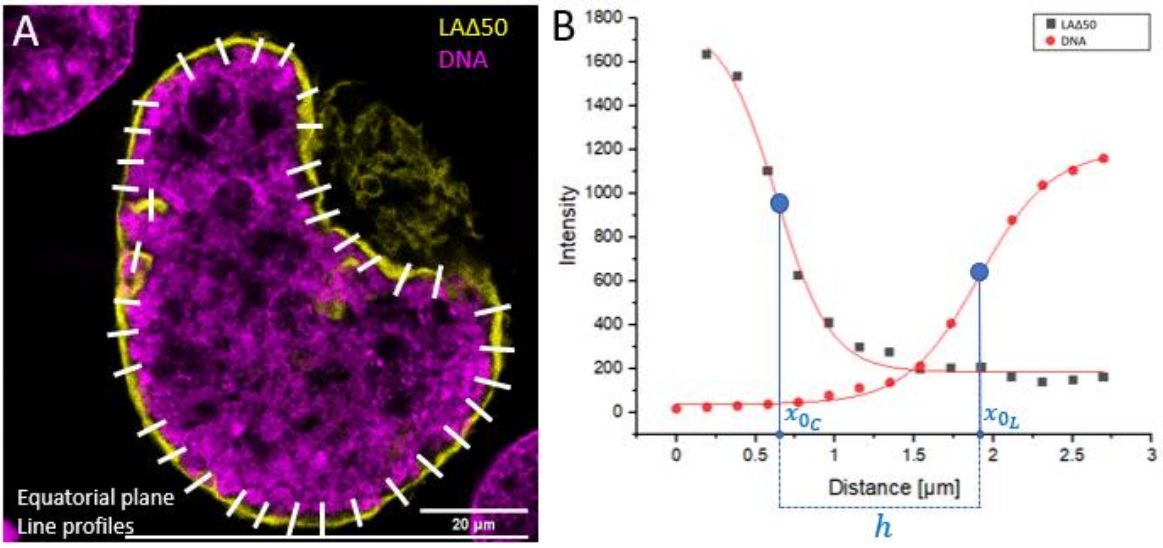

Fig. 25 Example of Lamin-Chromatin distance h analysis. Confocal ProExM image of HEK293T expressing LAΔ50-eGFP with line profiles at the interface between LAΔ50 and chromatin (A). Intensity profiles of the two signals interpolated as Boltzmann sigmoids. The distance h is calculated as the difference between the two sigmoids flex points (indicated as blue dots) x_{0_C} and x_{0_L} (B). The second scale bar in image A is normalized by the EF=4.0±0.1.

Average area difference ΔA

In order to increase reproducibility, ImageJ was used to calculate the difference between the WT Lamin A (CTRL set) or LAΔ50 (HGPS set) area and the DNA area on the same sets (N=15) used for the measurements of the Lamin-Chromatin distance h. A Gaussian blur (sigma=2 pixels) filtering was applied for each imaged cell, and the two signals were adjusted using the Auto Threshold. Signal segmentation was performed on the thresholded signals using the Magic Wand tool (Fig. 26 A). The signal areas were measured, and the area difference ΔA was then calculated as the difference between the two (A_{Lamin} , A_{DNA}, Fig. 26 B) and then normalized at a single-cell level on the A_{Lamin}. Finally, the results were analyzed using Prism (GraphPad).

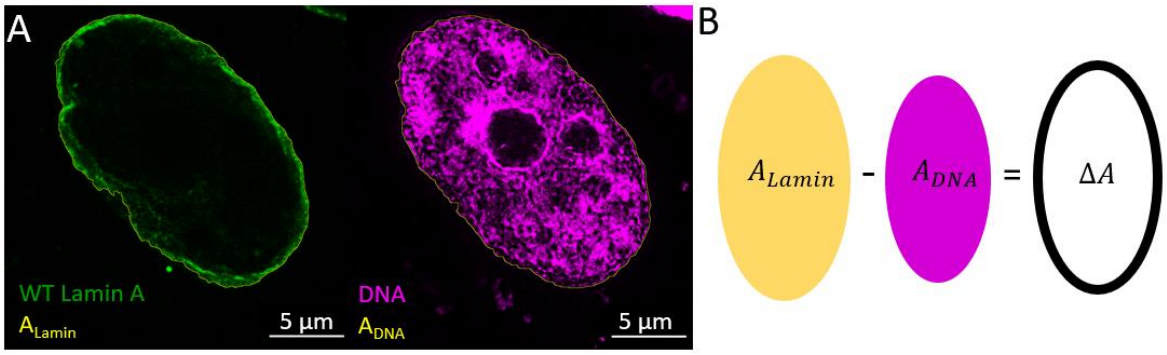

Fig. 26 Example of area difference ΔA analysis. Confocal ProExM image of HEK293T, the yellow border indicates the segmented area for the two signals A_{Lamin} , A_{DNA} (A). Schematic representation of single-cell ΔA calculation (B).

6.9.2. Particle analysis

The particle analysis was performed using ImageJ. First, images were filtered using a Gaussian blur (sigma=2 pixels), and a background subtraction (rolling ball radius=50 pixels) was applied (Fig. 27 A). Images were then converted to 8-bit, and the Auto Local Threshold was applied using the Bernsen method (Bernsen, 1986). Subsequently, watershed segmentation was performed on the thresholded image. Finally, Analyze Particles was used, and the generated binary mask image (Fig. 27 B) and results (area, centroid coordinates, perimeter, min & max grey value, mean grey value) were saved and processed using the software Prism (GraphPad).

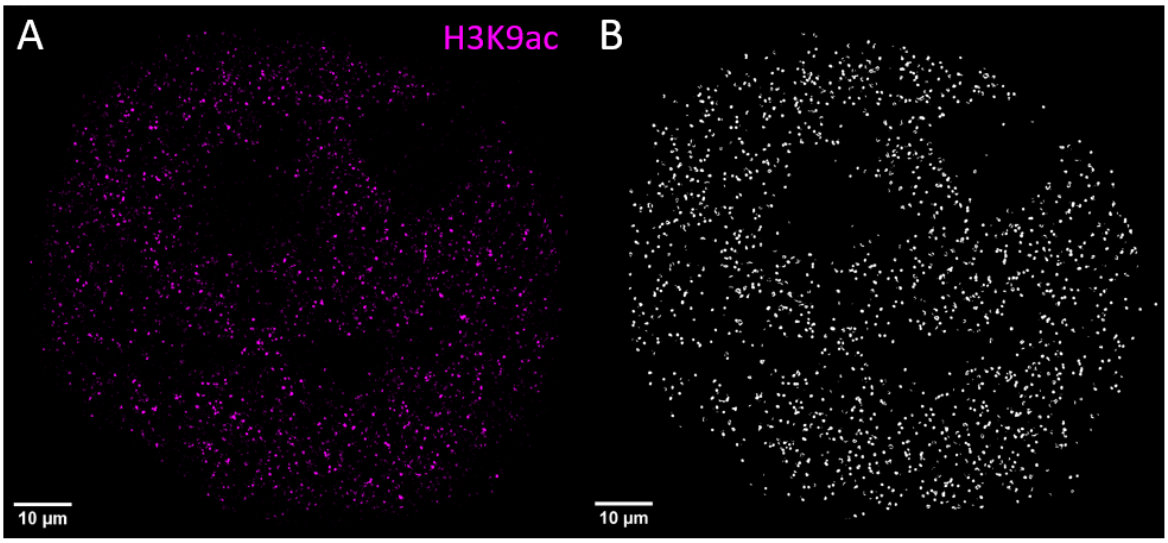

Fig. 27 Particle analysis example.. Confocal ProExM image of HEK293T labeled for H3K9ac (A). Binary mask image generated by image A particle analysis (B).

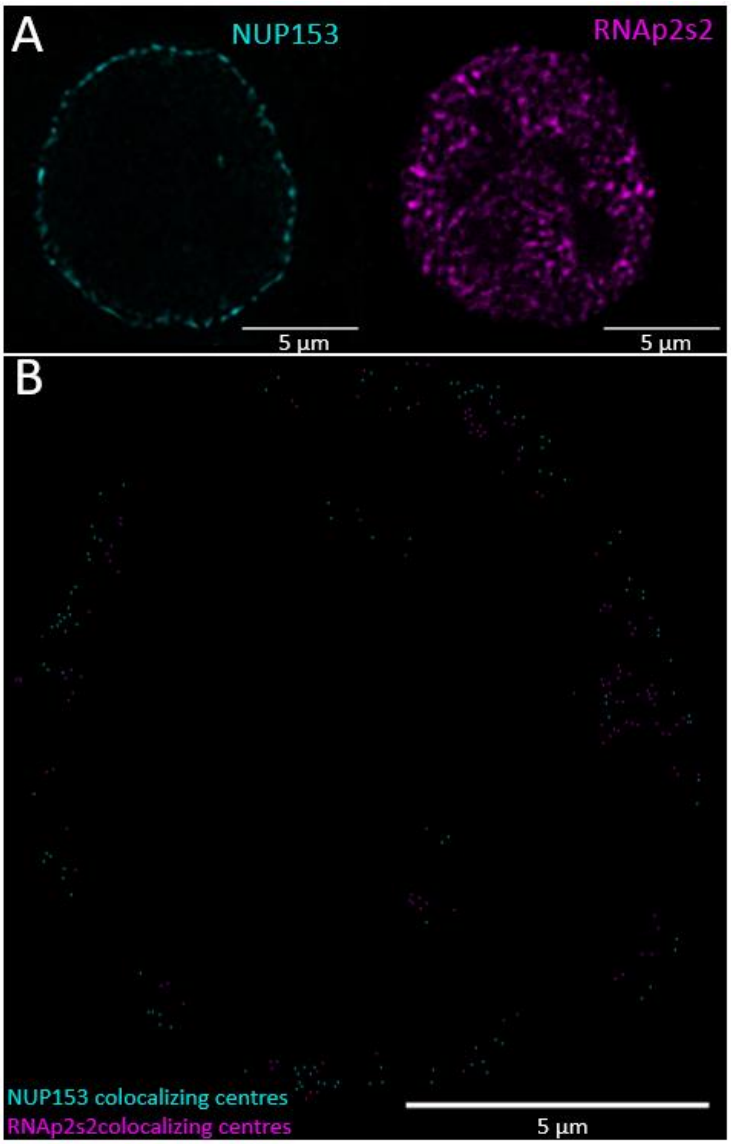

Fig. 28 Example of JACoP colocalization analysis. STED image of HEK293T labeled for NUP153 and RNApol2s2 (A). JACoP colocalization map (B).

6.9.3. Colocalization analysis

The particle analysis was carried out using ImageJ. Initially, the images underwent a Gaussian blur with a sigma value of 2 pixels. Subsequently, a background subtraction was performed using a rolling ball radius of 50 pixels. The processed images were then used to perform colocalization analysis using the plugin JACoP (Just Another Colocalization Plugin, Bolte et al., 2006), for object-based analysis using automatic thresholding (Costes et al., 2004) to determine which intensity values are considered significant for colocalization. The generated Pearson's correlation coefficient R, the overlap coefficient, and colocalization maps (Fig. 28) were then saved. Finally, statistical analysis was performed using the software Prism (GraphPad).

6.9.4. Cluster analysis

In order to investigate the spatial distribution of NPCs on nuclear membranes, we performed a cluster analysis. For each group (CTRL and HGPS), dSTORM imaging of NUP107 labeled cells was performed (N=10). Under our experimental conditions, NPCs appear as clusters of individual NUP107 localizations. Therefore, we designed a custom MATLAB (MathWorks) algorithm to generate density maps through the Getis and Franklin method (Getis & Franklin, 1987). One advantage of this technique over other methods, such as DBSCAN, is that it does not rely on user-defined parameters (Khater et al., 2020). In our analysis, the parameter related to the spatial size of the cluster can be identified through a global analysis of the Ripley function.

For each point, the number of localizations within the designated cluster radius ($r_{cluster} = 60\ nm$) centered at that particular localization is calculated. This value is then subtracted from the number of localizations that would be expected in the case of a uniform distribution. This process creates a three-dimensional graph in which, for each localization in z, the number of molecules l is represented. Finally, the number of clusters is counted through a procedure for identifying peaks, and the graph is interpolated throughout space and filtered with a Gaussian blur with a sigma equal to the average localization uncertainty of 20 nm to generate a 2D density map of l (Fig. 29).

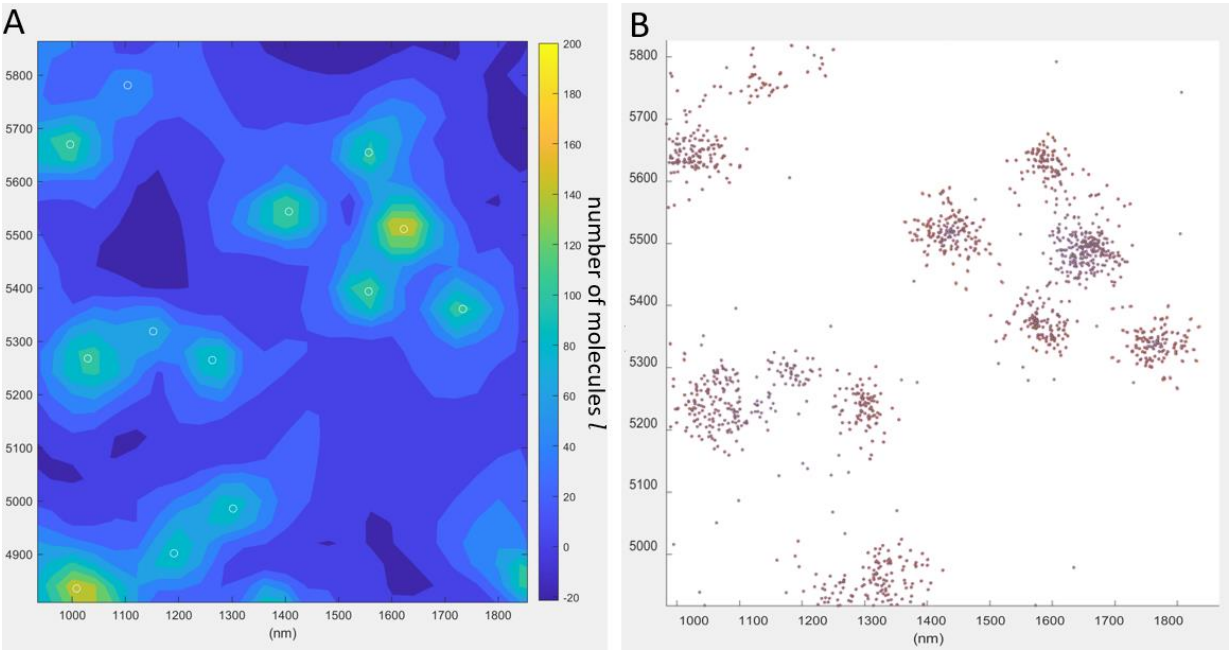

Fig. 29 Example of our cluster analysis generated with custom MATLAB algorithm. Getis and Franklin density map (r= 60 nm) (A) with corresponding NUP107 localization map (B). The white circles in image A indicate the identified clusters, corresponding to individual NPCs.

6.9.5. First neighbor distance analysis

The particle distribution analysis was performed using a custom MATLAB (MathWorks) algorithm designed to analyze spatial relationships and neighbor distances in biological data starting from the CSV files containing the positions of the centroids generated by the particle analysis. The X and Y positions of particles are extracted from the data and converted into distance units (nm). For each particle, the program calculates the distances to all other particles using Euclidean distance calculations. It filters out distances exceeding the maximum distance ($R_{max} = 5000\ nm$). Subsequently, the program calculates histograms of distances for each particle, categorizing them into four groups (I, II, III, IV) based on the cumulative number of neighbors within certain distances, and finally generates an image containing histograms for each category of neighbors showing the mean distance (Fig. 30). The exported data were then analyzed using the software Prism (GraphPad).

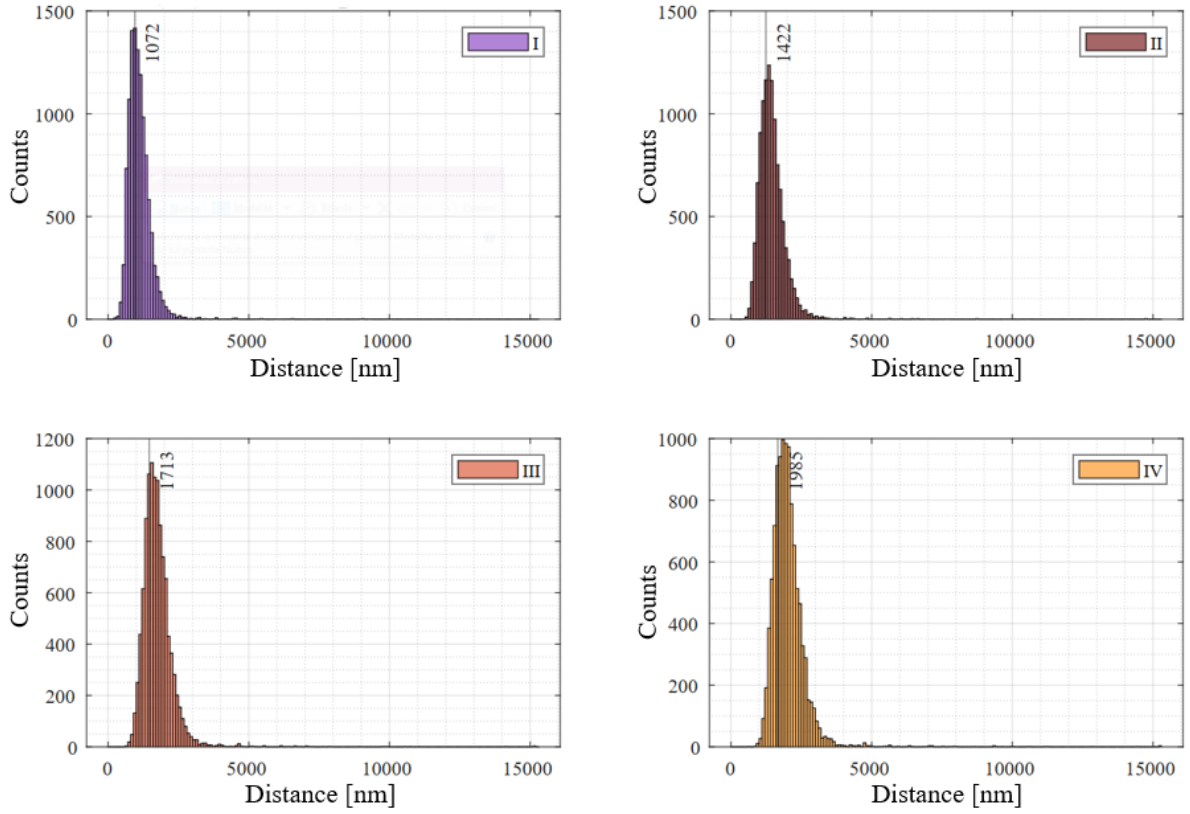

Fig. 30 Example of image output of the MATLAB neighbor distance analysis algorithm, calculating the first four neighbors. (HP1α, HGPS set).

7. RESULTS AND DISCUSSION

7.1. Protocol optimization

7.1.1. Achieving super-resolution imaging with Expansion Microscopy

As a first test for the super-resolution capability of ExM, we decided to image HeLa cells immunolabeled for microtubules and clathrin-coated pits. The nanoscale structure of these plasma membrane proteins involved in endocytosis makes them a widely used model in the field of super-resolution imaging and single-molecule localization microscopy (Gambarotto et al., 2021; Ma et al., 2022).

We performed confocal imaging of the non-expanded (Fig. 31 A) and the expanded (Fig. 31 B) cells.

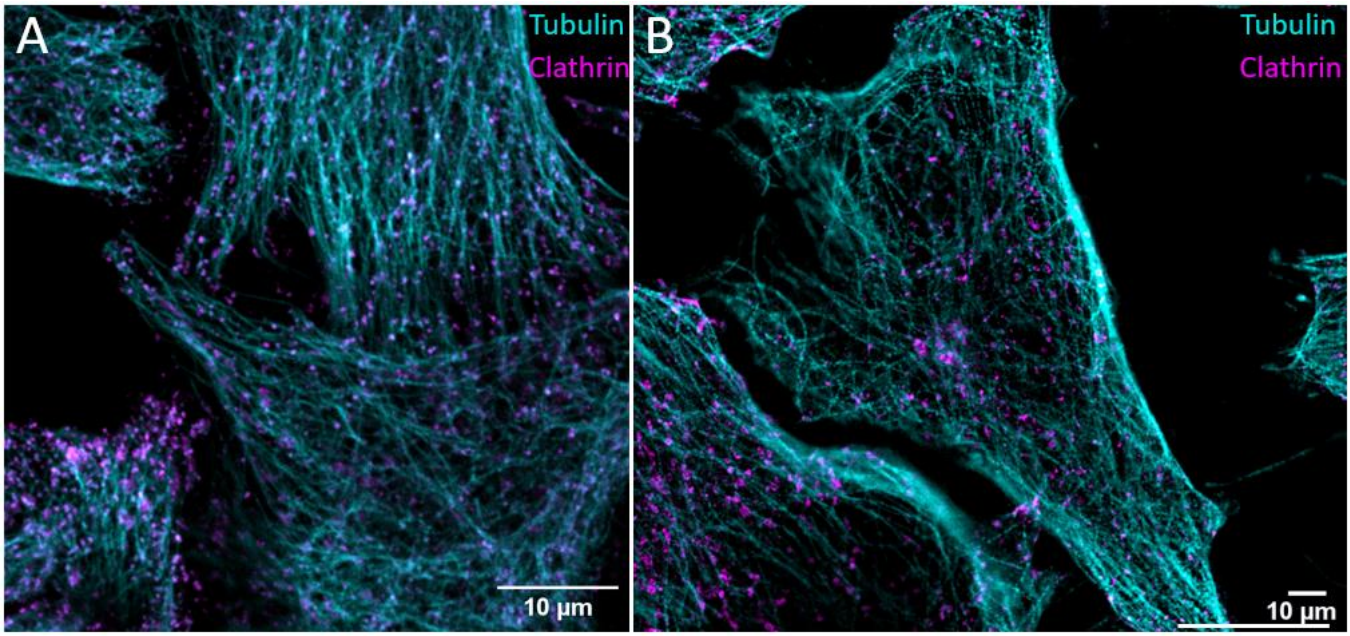

Fig. 31 Confocal imaging of clathrin-coated pits in HeLa cells. Pre-expansion (A) and post- expansion with ExM (B). The second scale bar in image B is normalized by the EF=4.1±0.2.

Then, we compared the imaging of single clathrin-coated pits between pre- and post-expansion and analyzed the relative intensity profiles. As shown in Fig. 32, in the confocal imaging of the non-expanded ones the hollow central part of the pits is not resolved (Fig. 32 A, B, C), while in the ExM images is visible the internal hole (Fig. 32 D, E, F).

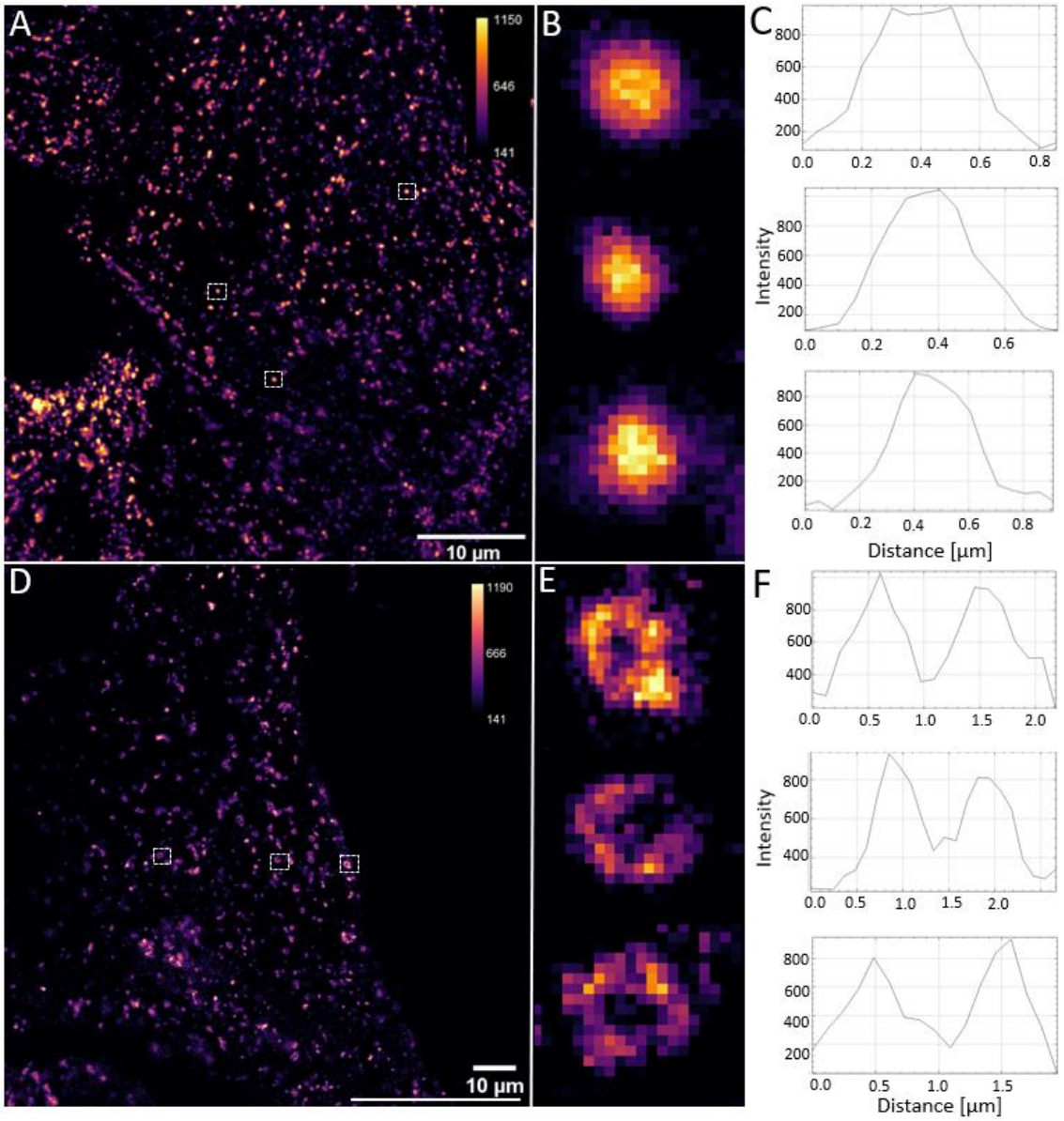

Fig. 32 Confocal imaging of clathrin-coated pits in HeLa cells. Pre-expansion (A) and post- expansion with ExM (D). Images B and E are the magnification of the dotted squares in images A and D. C and F are the intensity profiles of images B and E. The second scale bar in image D is normalized by the EF=4.1±0.2.

Finally, we analyzed the intensity profiles using the software OriginPro (OriginLab). The unresolved images were fitted as a single Gaussian peak, and the pit external diameter d_{ext} was calculated as the peak Full Width Half Maximum $FWHM$ (Fig. 33 A). The resolved ExM images were interpolated using a double Gaussian fit, measuring the internal diameter d_{int} as the distance between the two peaks and d_{ext} as (Fig. 33 B):

$$d_{ext,ExM} = \left(x_{c,2} + \frac{FWHM_2}{2}\right) - \left(x_{c,1} - \frac{FWHM_1}{2}\right) \tag{7.1}$$

Where $x_{c,1}$ and $x_{c,2}$ and are the positions of the two peaks.

We obtained the following results (N=10):

- $d_{ext,non-exp} = 330 \pm 20\ nm$
- $d_{int,ExM} = 1000 \pm 40\ nm$
- $d_{ext,ExM} = 1420 \pm 140\ nm$

Although the variability of clathrin-coated pits during the cell life does not make it an ideal reporter for the calculation of the EF, we can estimate the nanoscale EF from the pre- and post-expansion d_{ext} as:

$$EF_{nano} = \frac{d_{ext,non-exp}}{d_{ext,ExM}} = 4.2 \pm 0.2 \tag{7.2}$$

The obtained EF_{nano} is in accordance with the measured macroscale $EF_{macro} = 4.1 \pm 0.2$.

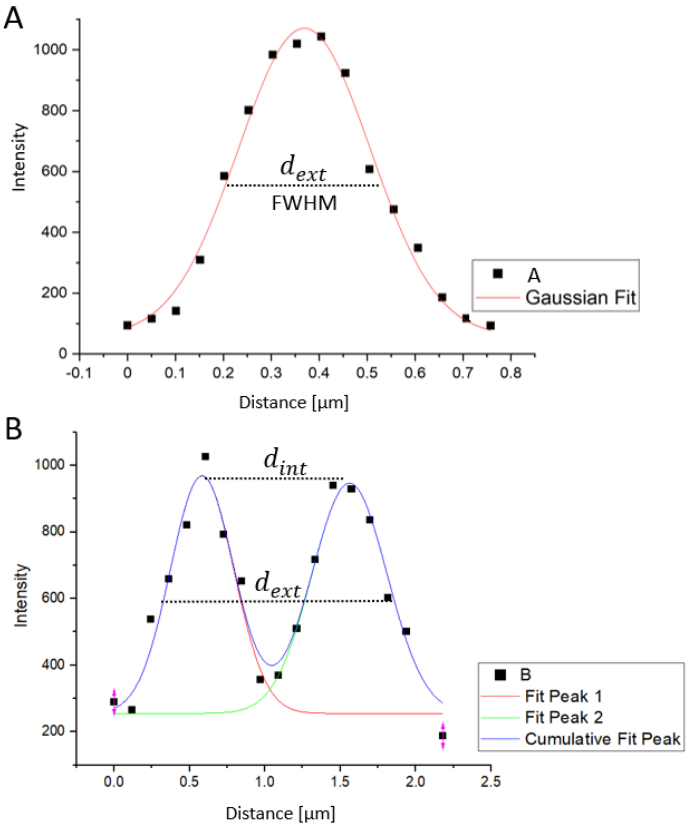

Fig. 33 Fitting of clathrin-coated pits intensity profiles. Gaussian fit of non-expanded clathrin-coated pits (A). *FWHM=0.32±0.01.* Fit equation: $y = y_0 + \frac{A}{w\sqrt{\frac{\pi}{4\ln(2)}}} e^{-\frac{4\ln(2)\,(x-x_c)^2}{w^2}}$

Double Gaussian fit of expanded clathrin-coated pits (B). $FWHM_1$*=0.42±0.05,* $FWHM_2$*=0.50±0.06.* Cumulative fit equation: $y = y_0 + \frac{A}{w\sqrt{\frac{\pi}{2}}} e^{-\frac{2\,(x-x_c)^2}{w^2}}$

Analysis performed using OriginPro.

7.1.2. ExM and Pro-ExM Protocol Comparison

In order to compare the standard ExM protocol (Chen et al., 2015) and the Pro-ExM (Tillberg et al., 2016), we tested both techniques on a sample based on MCF-10A cells. We decided to label nascent DNA using EdU and the protein Proliferating cell nuclear antigen (PCNA) to test the two expansion protocols both on DNA and a model protein. The confocal imaging on the non-expanded MCF-10A cells is visible in Fig. 34.

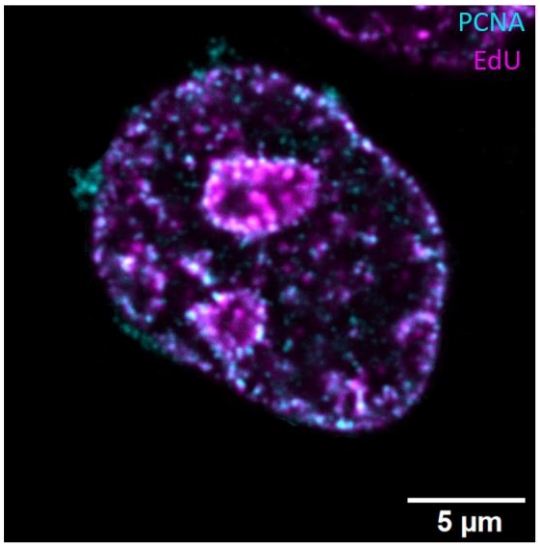

Fig. 34 Confocal imaging of MCF-10A cells labeled for PCNA and replicating DNA using EdU.

Next, we expanded two different parts of the sample using the two expansion protocols and then imaged them in the same conditions using a confocal microscope. The expanded images

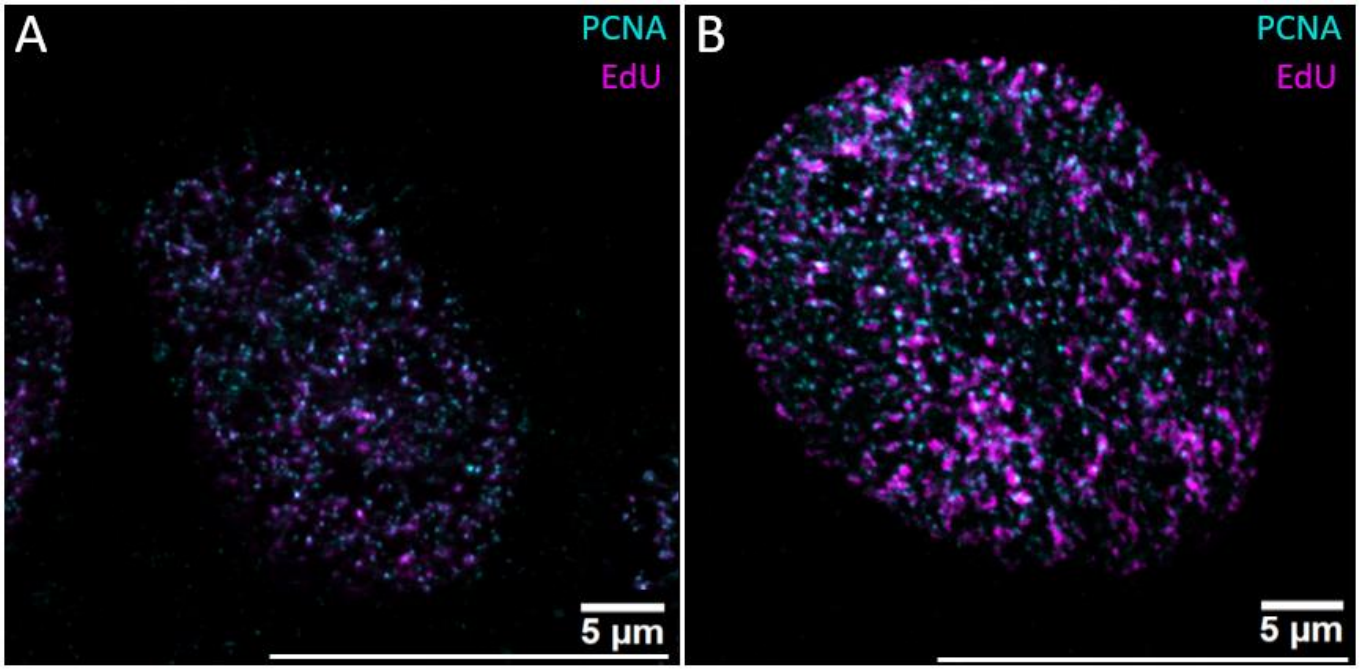

Fig. 35 Expansion protocols comparison. Confocal imaging of expanded MCF-10A cells labeled for PCNA and replicating DNA using EdU. The second scale bar in the images is normalized by the EF. ExM protocol, EF=4.1±0.1 (A). Pro-ExM protocol, EF=4.3±0.1 (B).

are shown in Fig. 35.

Using the ExM protocol (Fig. 35A), we achieved an $EF = 4.1 \pm 0.1$, while with the Pro-ExM protocol, the reached EF was 4.3 ± 0.1.

The signal intensity I for the labeled biological structures was analyzed using ImageJ, with the following results:

- $Average\ I_{\ \mathrm{ExM},\ EdU} = 29 \pm 6\ a.u.$
- $Average\ I_{\ \mathrm{ExM},\ PCNA} = 161 \pm 30\ a.u.$
- $Average\ I_{\ \mathrm{Pro-ExM},\ EdU} = 550 \pm 69\ a.u.$
- $Average\ I_{\ \mathrm{Pro-ExM},\ PCNA} = 284 \pm 46\ a.u.$

Overall, the Pro-ExM protocol performed better in our comparative test. For this reason, we decided to use it in this work for our experiments.

7.1.3. Secondary antibodies restaining (2ABR)

In order to compensate for the reduction of fluorescence signal caused by the expansion protocol, we tested a new method based on the restaining of the secondary antibodies used during the indirect immunostaining. This method is based on the assumption that the primary antibodies used to label the biological structures of interest in the sample, anchored to the hydrogel due to the cross-linking step, will resist the proteinase digestion.

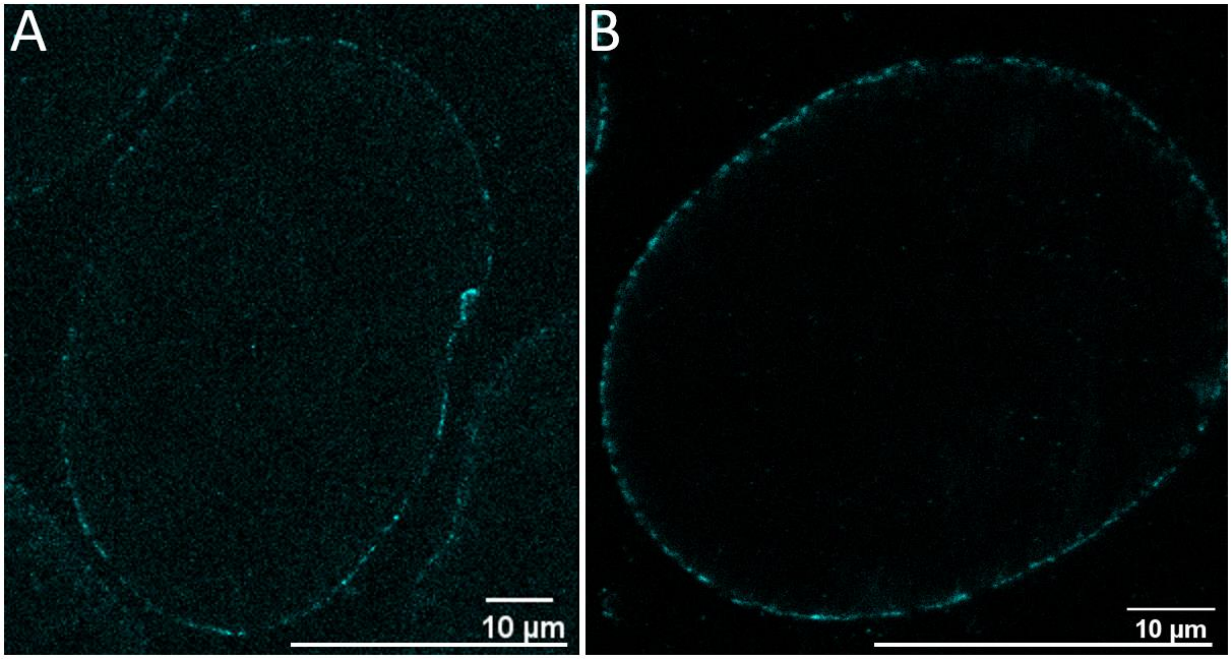

Fig. 36 Secondary antibodies restaining (2ABR). Confocal ProExM image of HEK293T labeled for NUP153 (A). Same sample after 2ABR (B). The second scale bar in the images is normalized by the EF=4.0 ± 0.1.

The 2ABR method was tested on HEK293T immunolabeled for NUP153 and expanded using the ProExM with subsequent confocal imaging, shown in Fig 36. The visible fluorescence signal increase has been assessed by calculating both the Signal-to-Noise Ratio (SNR) and the Signal-to-Background Ratio (SBR).

The signal intensities were quantified using ImageJ, and then the SNR was calculated as the ratio between the mean signal intensity and its standard deviation, while the SBR was calculated as the ratio between the mean signal intensity and the mean background intensity, with the following results:

- $SNR_{ProExM} = 1.78 \pm 0.05$
- $SNR_{2ABR} = 2.8 \pm 0.1$

- $SBR_{ProExM} = 1.18 \pm 0.03$
- $SBR_{2ABR} = 1.52 \pm 0.01$

2ABR-ProExM has proven effective in increasing both the SNR and the SBR of immunostained target proteins fluorescent signal, with a respective 58% and 29% increase.

7.2. Progerin-Induced Alterations in Nuclear Architecture: Insights from an HGPS Model

7.2.1. HGPS cellular model validation

In order to validate our cellular model of HGPS, we first verified that our stable cell line expressing LAΔ50-eGFP presented the phenotypical characteristics distinctive of the disease at a cellular level.

We performed confocal imaging that revealed that the accumulation of LAΔ50 caused the expected structural abnormalities in the nuclear lamina, with the presence of nuclear blebbing and invaginations within the nuclear membrane (Fig. 37).

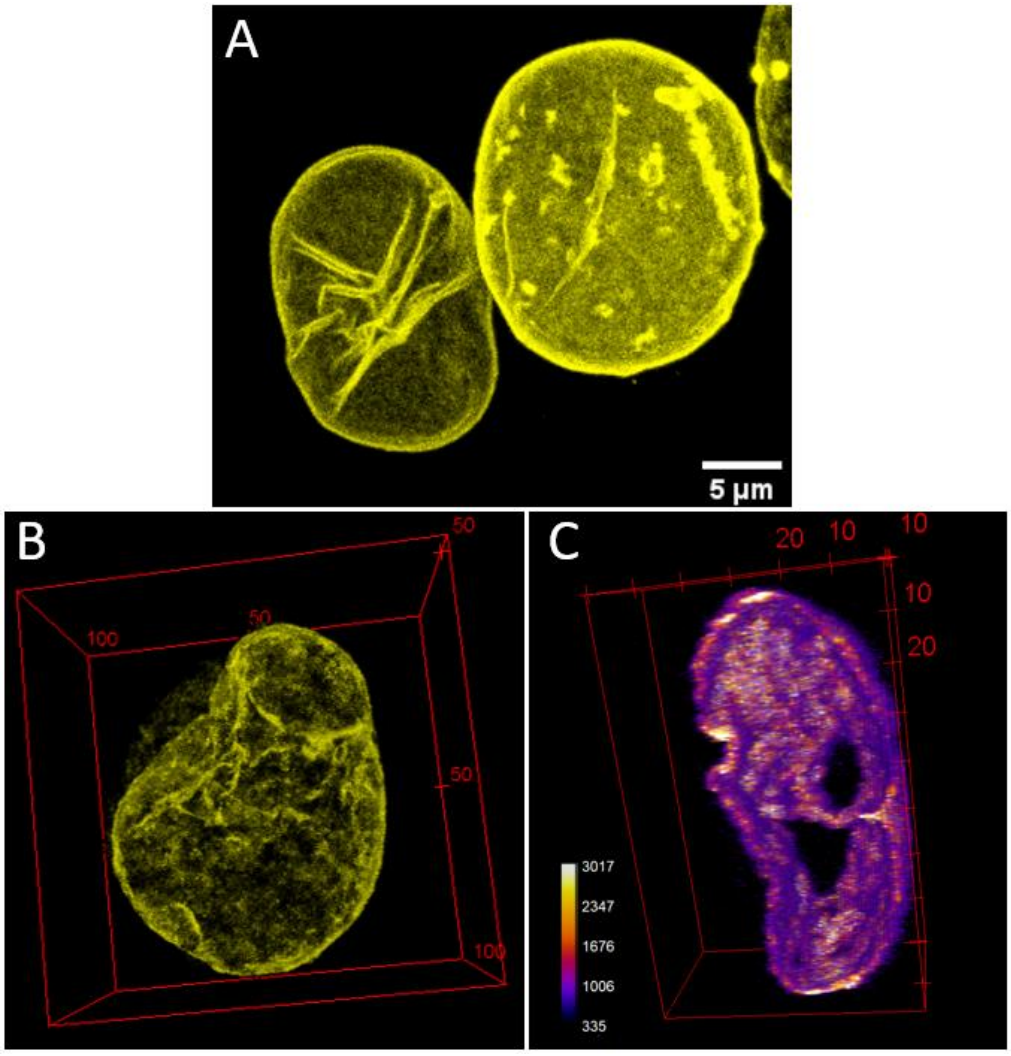

Fig. 37 . Confocal imaging of HEK293T expressing LAΔ50-eGFP showing the typical structural abnormalities of the nuclear lamina related to HGPS, characterized by the presence of irregular bulges and invaginations. Maximum z-projection of non-expanded cell (A). Post-expansion (ProExM) 3D reconstruction of LAΔ50-eGFP organization (B). Cross section of image B showing details of the nuclear invagination (C). B and C grid units µm, EF=4.0 ± 0.1.

To quantify and compare the expression of LAΔ50 and Lamin A in our cellular model of HGPS, we performed a Western Blot analysis (Fig. 38, N=2).

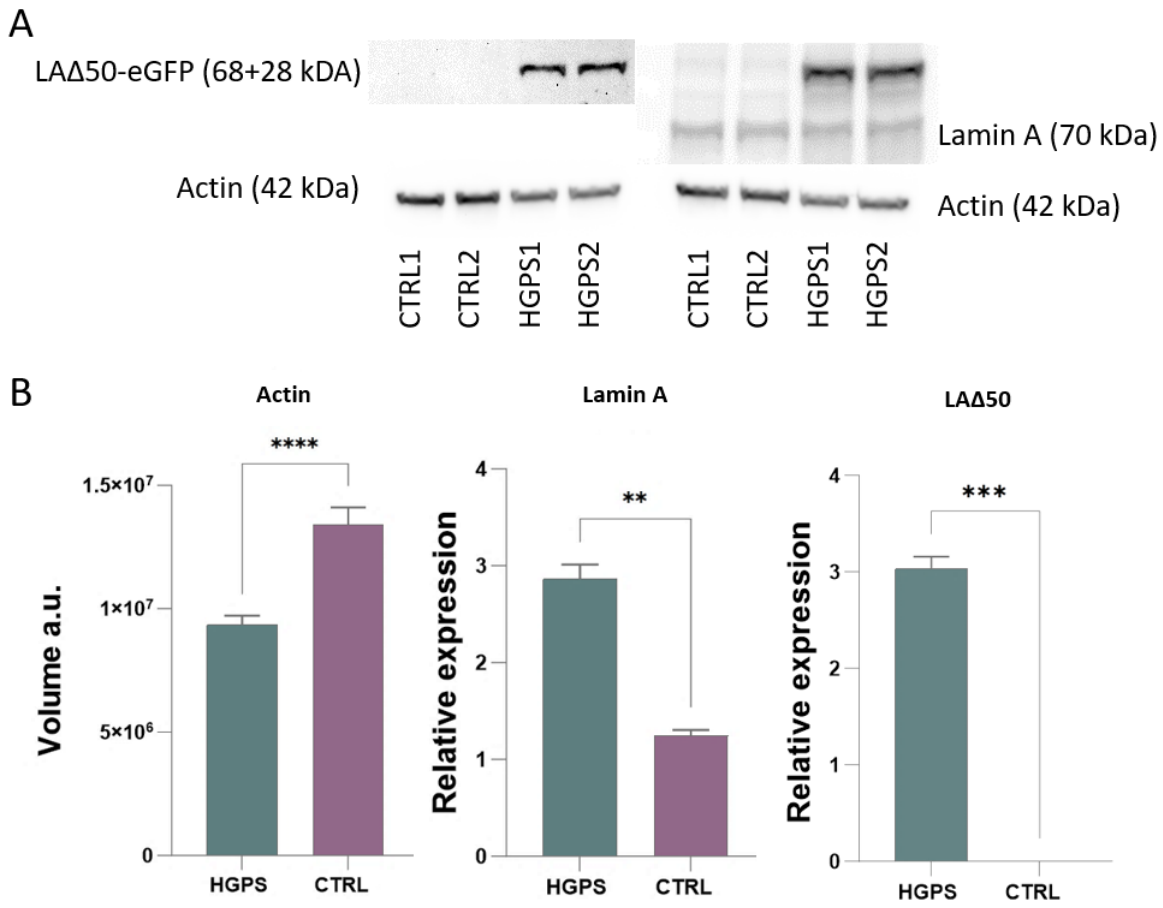

Fig. 38 Western Blot analysis of Lamin A and LAΔ50. Actin was used as a reporter. Chemiluminescence images of the protein blots (A). Quantification plots (B). Significance evaluated with Kolmogorov-Smirnov test using Prism. N=2

In our HGPS model, the Lamin A protein expression was significantly increased compared to the CTRL set. Furthermore, as expected, LAΔ50 was expressed only in the HGPS set.

Phosphorylated histone H2AX (γH2AX) expression

Next, to assess that the sole induced expression of LAΔ50 was able to simulate the pathological conditions of HGPS, we evaluated the expression of the DSB biomarker γH2AX, known to be upregulated in fibroblast from HGPS patients (Musich & Zou, 2011).

For both sets (HGPS, CTRL), we performed confocal imaging of non-expanded cells labeled for γH2AX and the actively transcribed chromatin marker H3K9ac (Fig. 39).

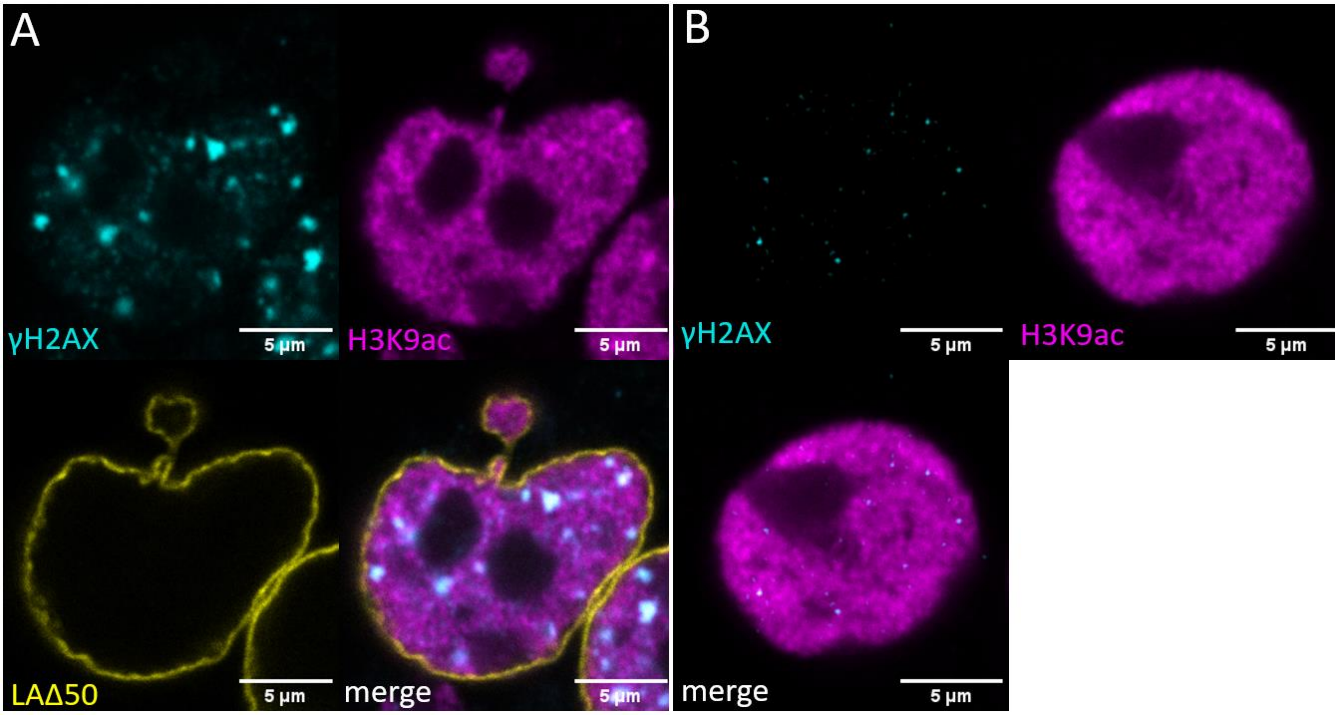

Fig. 39 Confocal imaging of non-expandend HEK293T labeled for the DSB biomarker γH2AX . HGPS model expressing LAΔ50-eGFP (A) and CTRL (B). Image A shows the typical accumulation of γH2AX nuclear foci related to HGPS.

Subsequently, to quantify the nuclear foci of γH2AX, unresolved in the non-expanded sample, we performed ProExM on the same sample batch. The confocal images of the expanded cells are visible in Fig. 40.

Finally, we performed particle analysis (number of analyzed cells N=15), as illustrated in section 6.9.2, on the ProExM images to compare the expression of γH2AX between the HGPS and the CTRL set. The two distributions were compared using the Kolmogorov-Smirnov test. As shown in Fig. 41, there is a significant increase in nuclear γH2AX foci in the HGPS set due to the cellular accumulation of DBS caused by Progerin expression, confirming the validity of our model in simulating the pathological conditions related to HGPS disease.

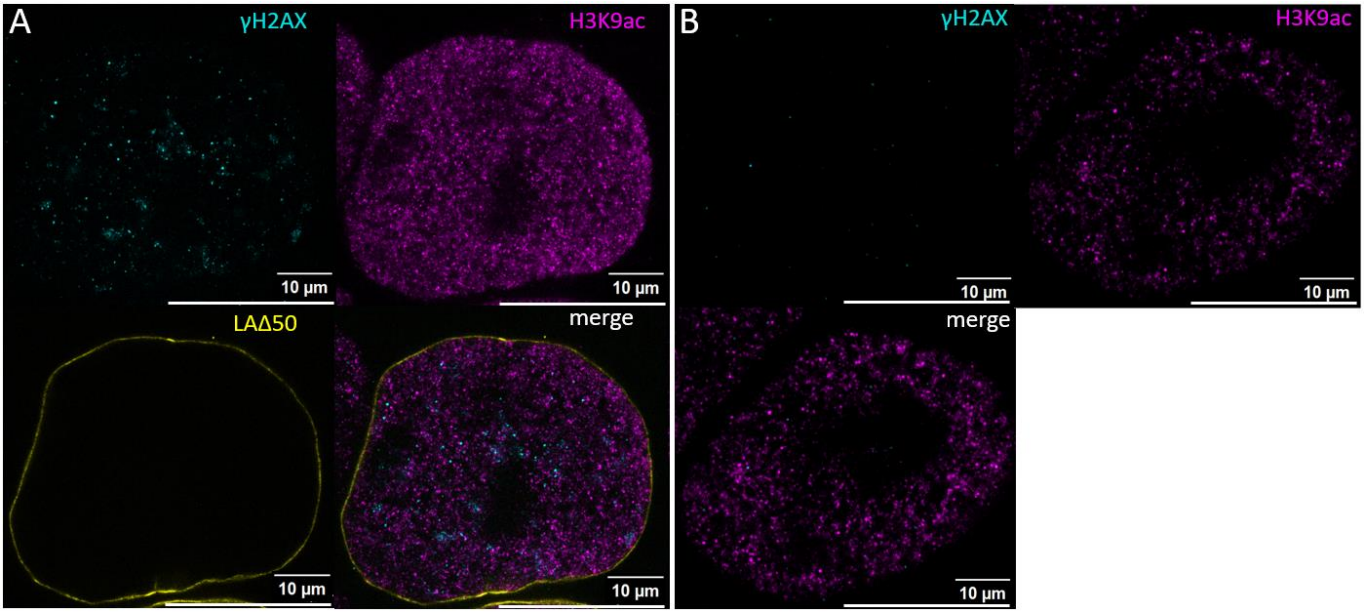

Fig. 40 Confocal ProExM imaging of HEK293T labeled for the DSB biomarker γH2AX . HGPS model expressing LAΔ50-eGFP (A) and CTRL (B). The second scale bar in the images is normalized by the EF=4.1±0.1.

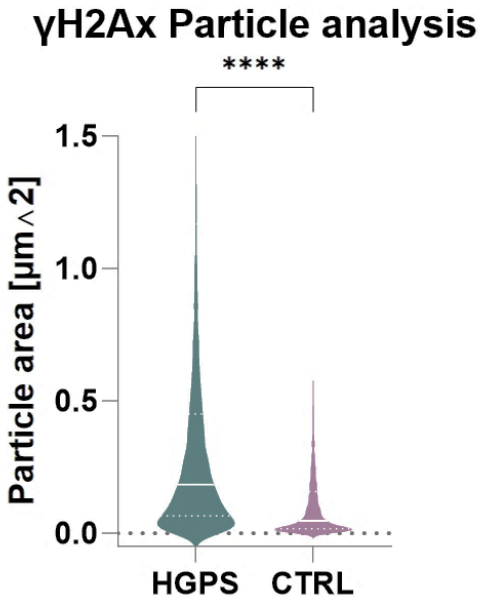

Fig. 41 Particle analysis of the γH2AX nuclear foci. Significance evaluated with Kolmogorov-Smirnov test using Prism. N=15.

7.2.2. Spatial relationship between DNA and lamin at the nuclear periphery

In order to evaluate the spatial relationship between nuclear lamina and chromatin, we prepared a set of samples labeled for DNA with SPY650-DNA. For this experiment, to quantitively compare the two sets of cells, the CTRL set was constituted by HEK293T transiently transfected to induce the expression of WT Lamin A-eGFP.

As shown in Fig. 42, in the HGPS set, there is a considerable variation in chromatin compaction at the nuclear periphery compared to the CTRL. This loss of chromatin compaction appears to disrupt the physical association with the lamin, leading to what seems to be a spatial separation between the two structures, as visible in Fig. 42 C.

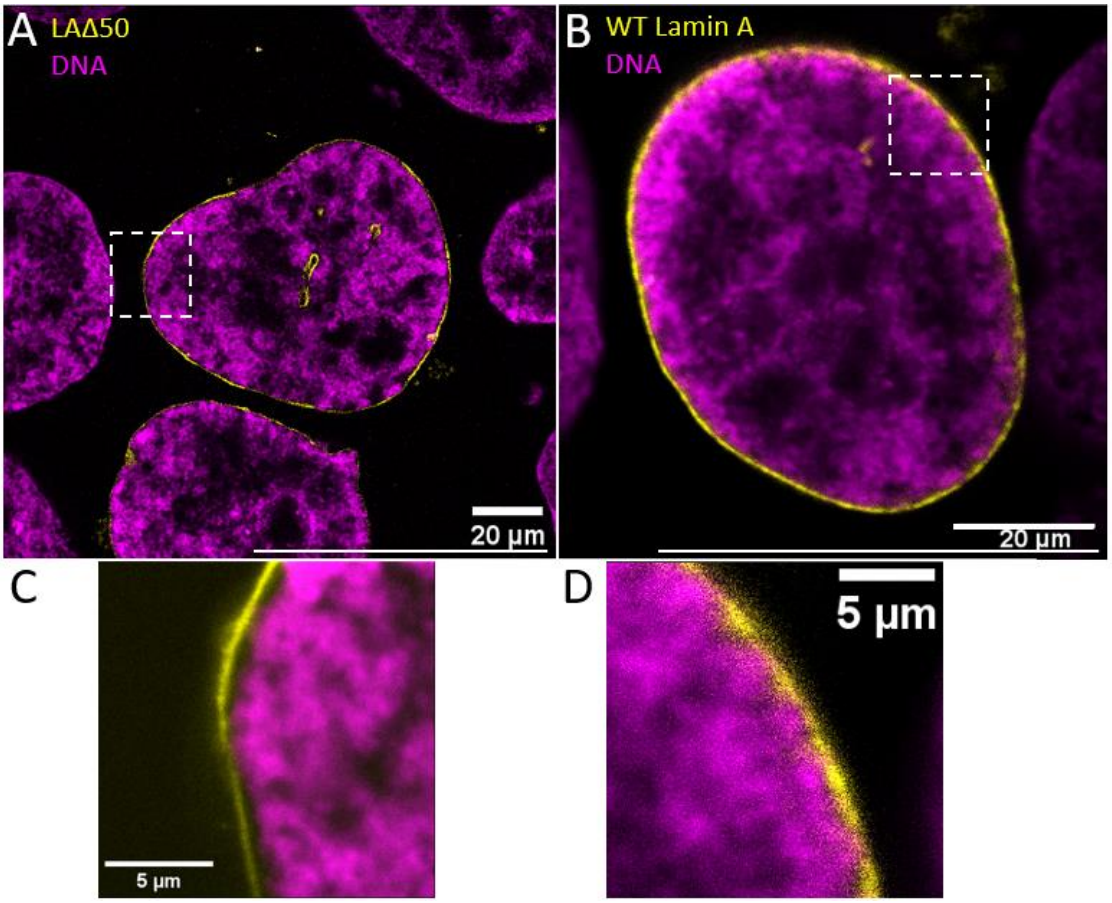

Fig. 42 Confocal ProExM imaging of HEK293T. The DNA is labeled with SPY650-DNA. HGPS model expressing LAΔ50-eGFP (A) and CTRL expressing WT Lamin A-eGFP (B). Images C and D are a magnification of the insets in images A and B, respectively. The second scale bar in the images is normalized by the EF=4.0±0.1.

Average Lamin-Chromatin distance h

We decided to quantify this separation by measuring the distance h between the labeled DNA and the nuclear lamin, as explained in section 6.9.1.

Our first approach, based on the manual analysis of the two signal intensity profiles explained in section 6.9.1, led to the following results:

- $h_{HGPS} = 200 \pm 90\ nm$
- $h_{CTRL} = 40 \pm 30\ nm$

The results are normalized by the EF=4.0±0.1. For our confocal imaging of expanded samples, the estimated effective resolution R_{ef} is given by our optical resolution (230 nm at 647 nm) normalized by the EF. So, in our case, $R_{ef} \approx 60\ nm$.

Considering the h distance results (Fig. 43) and our optical resolution, we can say that there is a significant difference between the two sets.

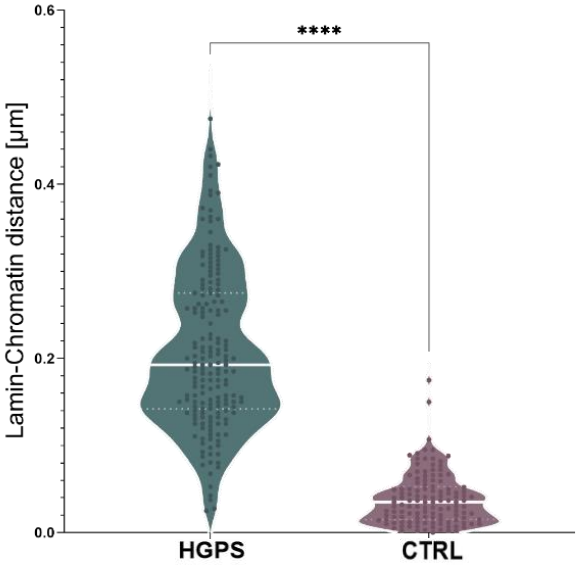

Fig. 43 Lamin-Chromatin distance. Significance evaluated with Kolmogorov-Smirnov test using Prism. N=15.

Average area difference ΔA h

Next, we decided to quantify this separation by measuring the area difference between the two segmented structures to increase reproducibility and reduce the error due to the manual signal elaboration used in the previous method, as illustrated in section 6.9.1.

The resulting ΔA, expressed as normalized on the single lamin area to be comparable, are shown in Fig. 44.

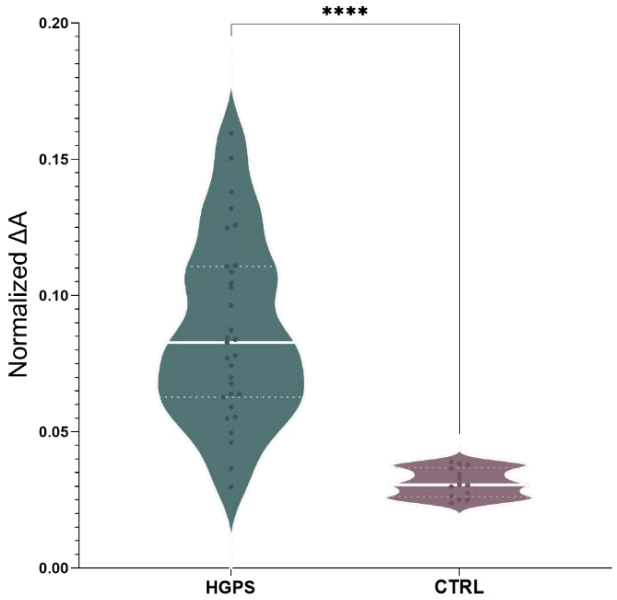

Fig. 44 Normalized Lamin-Chromatin area difference. Significance evaluated Kolmogorov-Smirnov test using Prism, N=20.

The resulting distributions are similar to the Lamin-Chromatin distances visible in Fig. 43, showing a significant difference between the two sets. These analyses revealed that the accumulation of LAΔ50 led to an abnormal spatial separation between DNA and lamin at the nuclear periphery in our HGPS model.

7.2.3. Heterochromatin Protein 1 (HP1α) and Proline-Rich Region Protein 14 (PRR14)

In order to understand the possible mechanisms behind this abnormal spacing between lamin and chromatin, we decided to investigate the possible deregulation of two proteins, HP1α and PRR14. These proteins are responsible for tethering peripheral heterochromatin to the nuclear lamina. Specifically, PRR14 acts as a bridge by binding the nuclear lamina and HP1-tagged heterochromatin (Poleshko et al., 2013; Ashapkin et al., 2019).

To compare the distributions of the proteins, we immunostained HP1α and PRR14 on both sets (HGPS, CTRL) and performed confocal microscopy. The non-expanded cells are shown in Fig. 45.

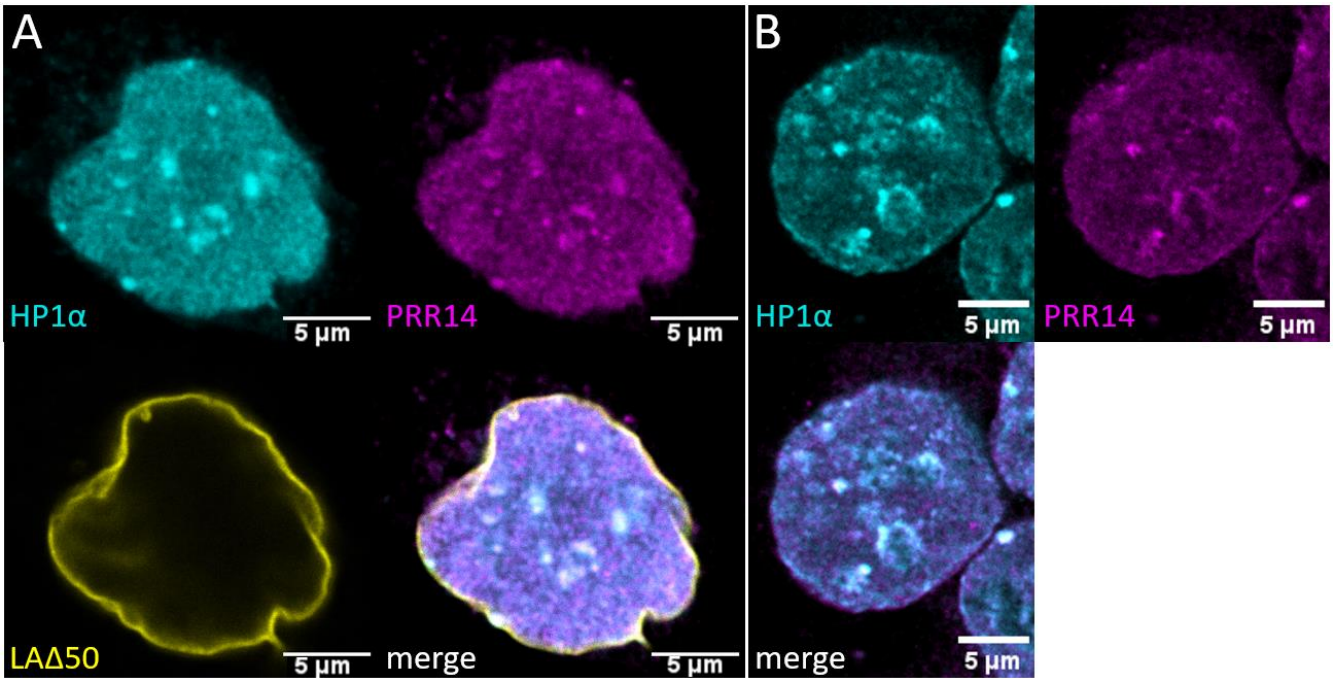

Fig. 45 Confocal imaging of non-expanded HEK293T labeled for HP1α and PRR14. HGPS model expressing LAΔ50-eGFP (A) and CTRL (B).

We then performed 2ABR-ProExM to resolve the nuclear foci of the two proteins. The super-resolved images are visible in Fig. 46.

On the 2ABR-ProExM images, we performed an object-based colocalization analysis (Fig. 47) that showed a significant decrease in the colocalization between HP1α and PRR14.

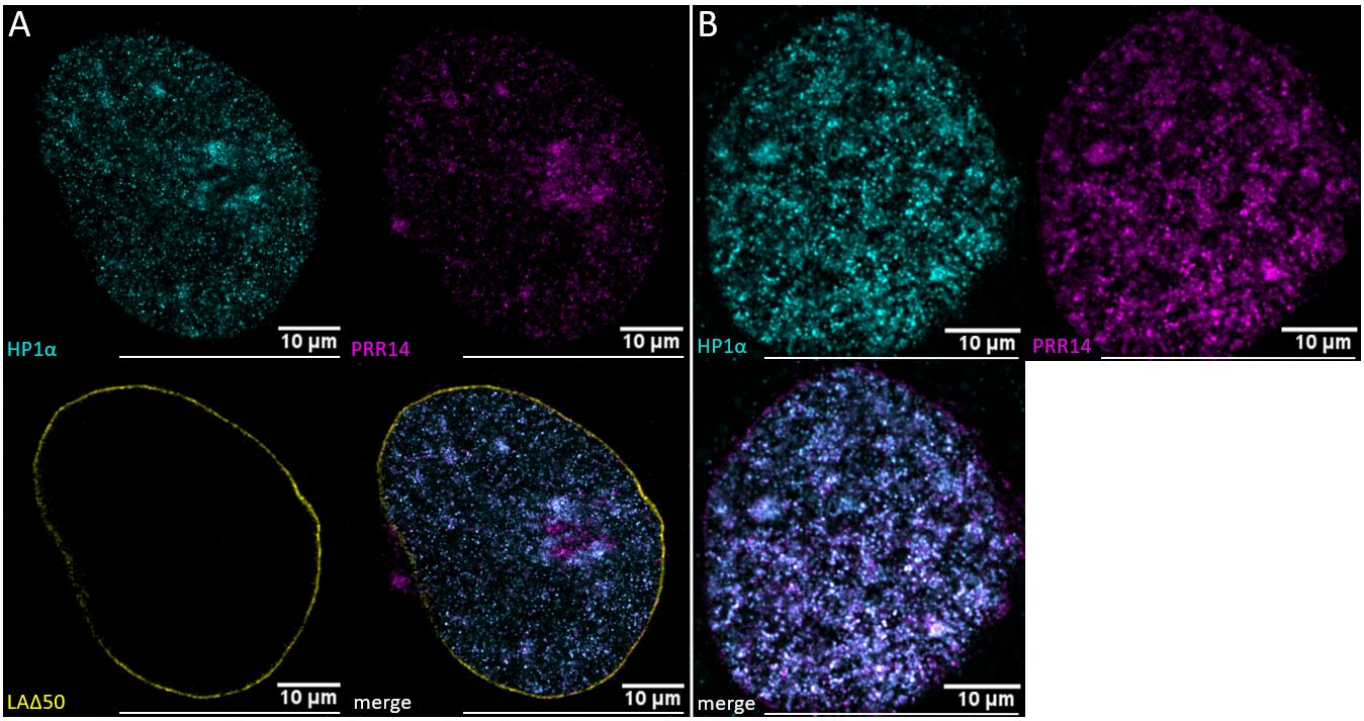

Fig. 46 Confocal 2ABR-ProExM imaging of HEK293T labeled for HP1α and PRR14. HGPS model expressing LAΔ50-eGFP (A) and CTRL (B). The second scale bar in the images is normalized by the EF=4.1±0.1.

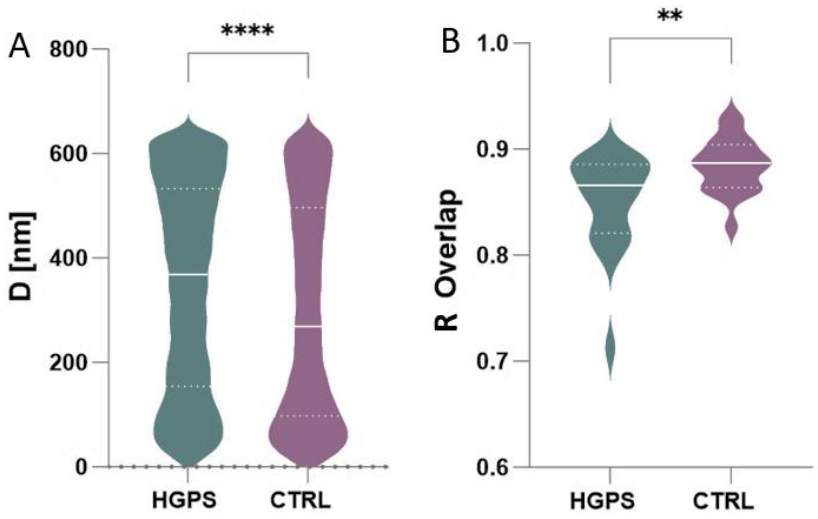

Fig. 47 JACoP object-based colocalization analysis of HP1α and PRR14. Distance distribution (A). Overlap coefficient distribution (B). Significance evaluated Kolmogorov-Smirnov test using Prism. EF=4.1±0.1, N=30.

Next, we performed particle analysis (N=30, Fig. 48) to compare the expression of HP1α and PRR14 between the HGPS and the CTRL set, which revealed a significant decrease in nuclear foci dimension in the HGPS set for both proteins.

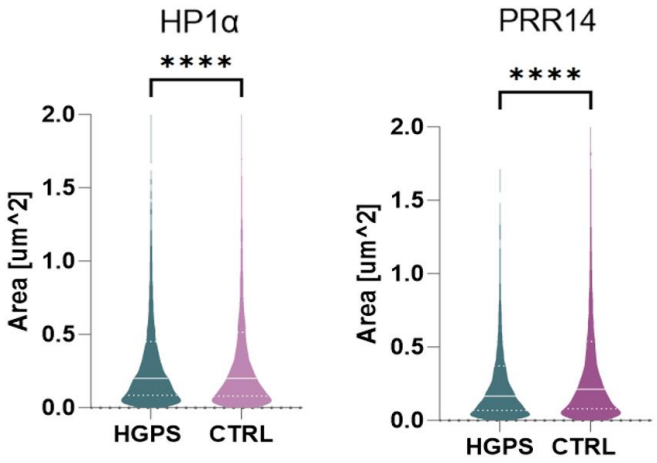

Fig. 48 Particle analysis of HP1α and PRR14. Significance evaluated Kolmogorov-Smirnov test using Prism. $EF = 4.1 \pm 0.1$, *N=30.*

To better evaluate and compare the expression of HP1α and PRR14, we then performed a Western Blot analysis (Fig. 49) that showed a decrease in the expression of the two proteins in our HGPS model.

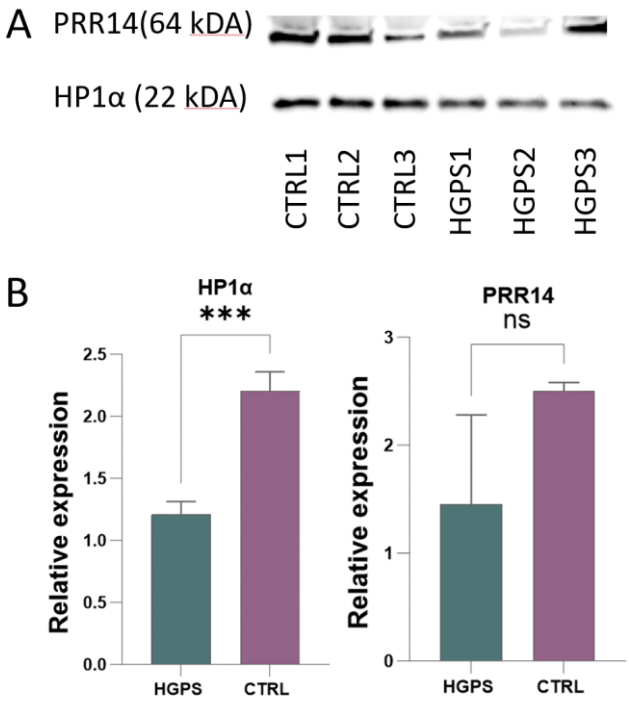

Fig. 49 Western Blot analysis of HP1α and PRR14. Actin was used as a reporter. Chemiluminescence images of the protein blots (A). Quantification plots (B). Significance evaluated Kolmogorov-Smirnov test using Prism, N=3.

Finally, we carried out a first neighbor distance distribution (FND) analysis (N=30, Fig. 50) to compare the distribution of HP1α and PRR14 between the two sets, which led to the following results:

- $Average\ FND\ _{HP1,\ HGPS} = 1072 \pm 5\ nm \equiv 261 \times EF \pm 5\ nm$
- $Average\ FND\ _{HP1,\ CTRL} = 1024 \pm 4\ nm\ \equiv 249 \times EF \pm 4\ nm$
- $Average\ FND\ _{PRR14,\ HGPS} = 1155 \pm 5\ nm \equiv 281 \times EF \pm 5\ nm$
- $Average\ FND\ _{PRR14,\ CTRL} = 1219 \pm 5\ nm \equiv 297 \times EF \pm 5\ nm$

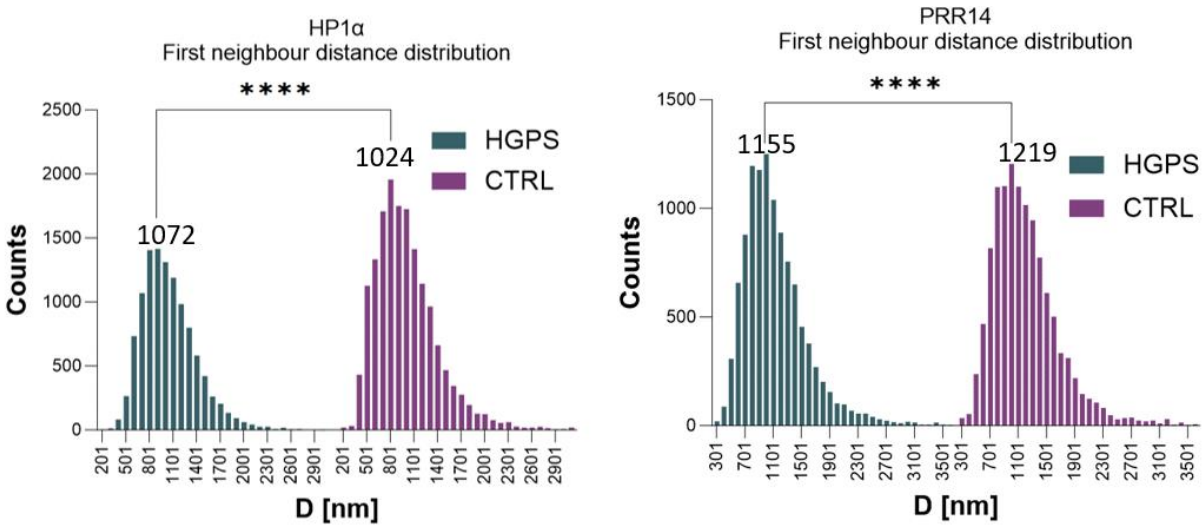

Fig. 50 First neighbor distance distribution analysis of HP1α and PRR14. $EF = 4.1 \pm 0.1$, N=30.

The distribution analysis shows a significant difference between the two sets for the two proteins, with an increased inter-foci distance for HP1α and a decreased one for PRR14 in the HGPS model.

Overall, our analyses demonstrate that the accumulation of LAΔ50 in HGPS affects the expression of HP1α and PRR14 and their ability to interact. The reduced expression of these two proteins, which translates into an increased inter-foci distance, could significantly reduce the connection between peripheral heterochromatin and nuclear lamina, leading to deregulation in the lamin-chromatin tethering mechanism.

7.2.4. NUP153 and RNA polymerase II

As previously reported by Al-Haboubi et al. in 2011, Lamin A mutations specifically impact the binding of NUP153. The subsequent mislocalization of NUP153 found in laminopathies such as HGPS could lead to genomic instability and altered transcription due to its association with actively transcribing chromatin regions (Cobb et al., 2016; Martins et al., 2020).

To investigate the possible alterations in the interaction between NUP153 and the DNA-dependent enzyme responsible for active gene transcription RNA polymerase II in HGPS, we decided to perform STED imaging, using the phosphorylation of Serine 2 within the RNA Polymerase II (RNAp2s2) as an active gene transcription marker (Fig. 51).

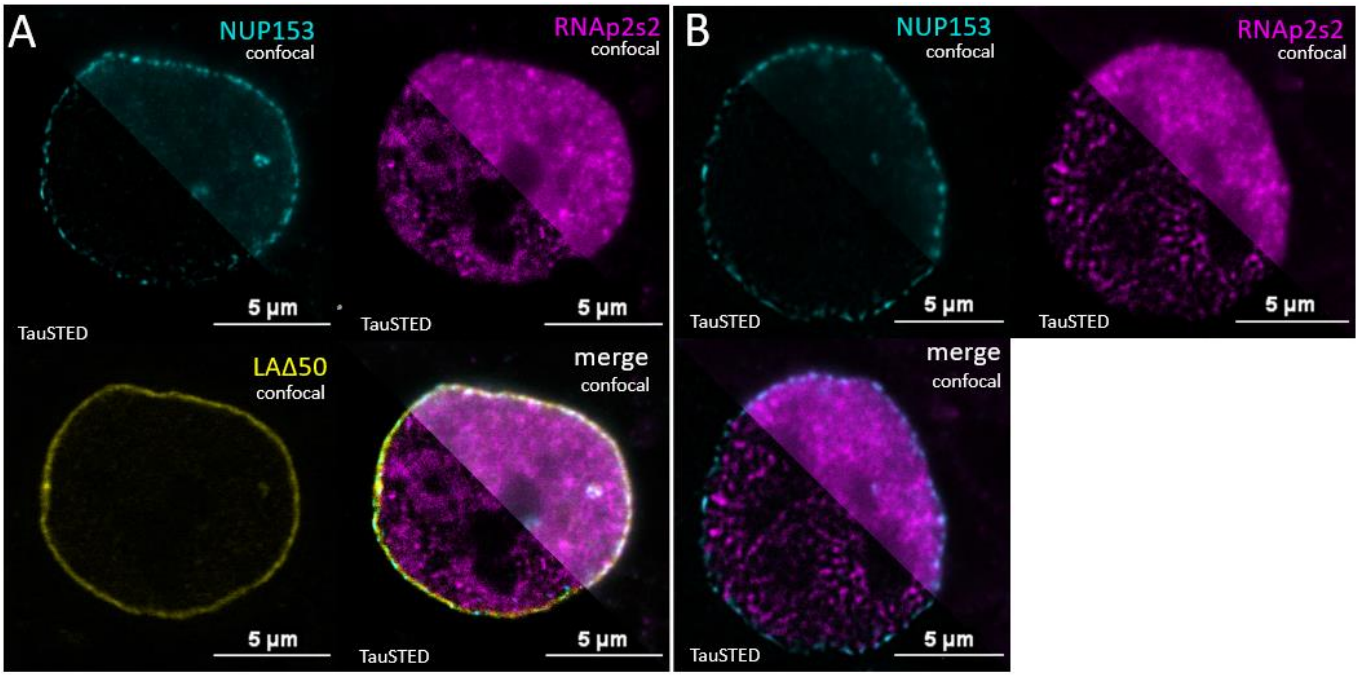

Fig. 51 Confocal and STED imaging of HEK293T labeled for NUP153 and RNAp2s2. HGPS model expressing LAΔ50-eGFP (A) and CTRL (B).

The object-based colocalization analysis (Fig. 52, N=30) showed a significant increase in the colocalization between NUP153 and RNAp2s2, which could potentially play a role in the increased transcriptional activity reported in previous works for HGPS (Arancio et al., 2014).

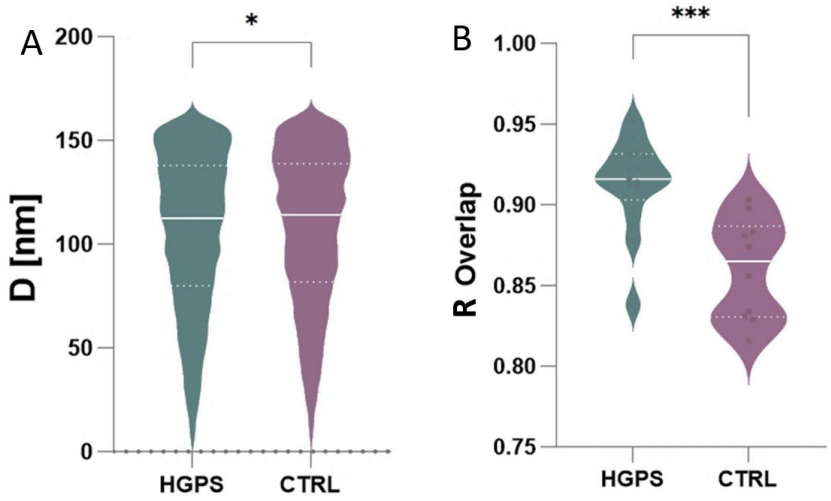

Fig. 52 JACoP object-based colocalization analysis of NUP153 and RNAp2s2. Distance distribution (A). Overlap coefficient distribution (B). Significance evaluated Kolmogorov-Smirnov test using Prism, N=30.

The observation of the STED imaging also suggests an apparent alteration in the distribution of RNAp2s2. The resolution provided by our STED imaging, calculated as explained in section 6.5.2, (R=124 nm for 647 nm laser excitation, depletion laser 775 nm) was insufficient for the detailed study of the RNAp2s2 nuclear foci. For this reason, 2ABR-ProExM experiments and their distribution analysis are reported in the next paragraph.

7.2.5. H3K9ac and RNAp2s2

In order to evaluate the transcriptional activity in our HGPS model, the epigenetic modification associated with active transcription H3K9ac was immunostained together with RNAp2s2 on both sets (HGPS, CTRL), and confocal microscopy was performed (Fig. 53).

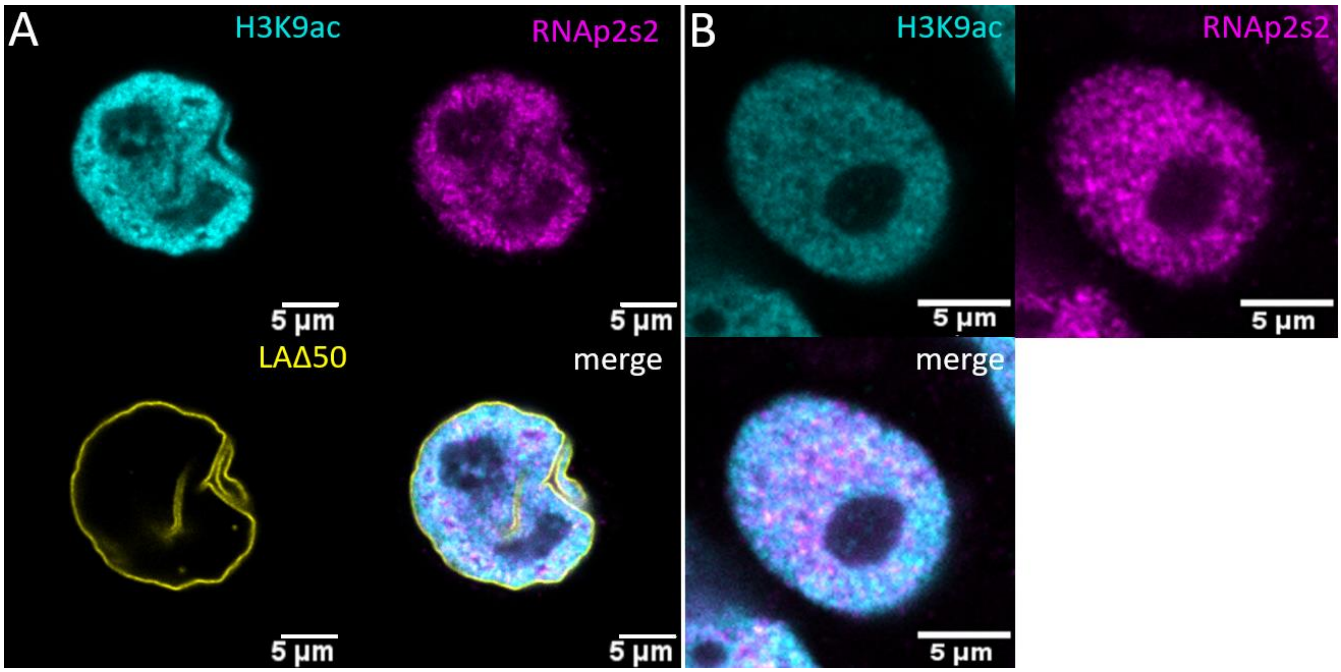

Fig. 53 Confocal imaging of non-expanded HEK293T labeled for H3K9ac and RNAp2s2. HGPS model expressing LAΔ50-eGFP (A) and CTRL (B).

Next, we performed 2ABR-ProExM to increase the resolution capability of the protein´s nuclear foci. The confocal images of the expanded cells images are shown in Fig. 54.

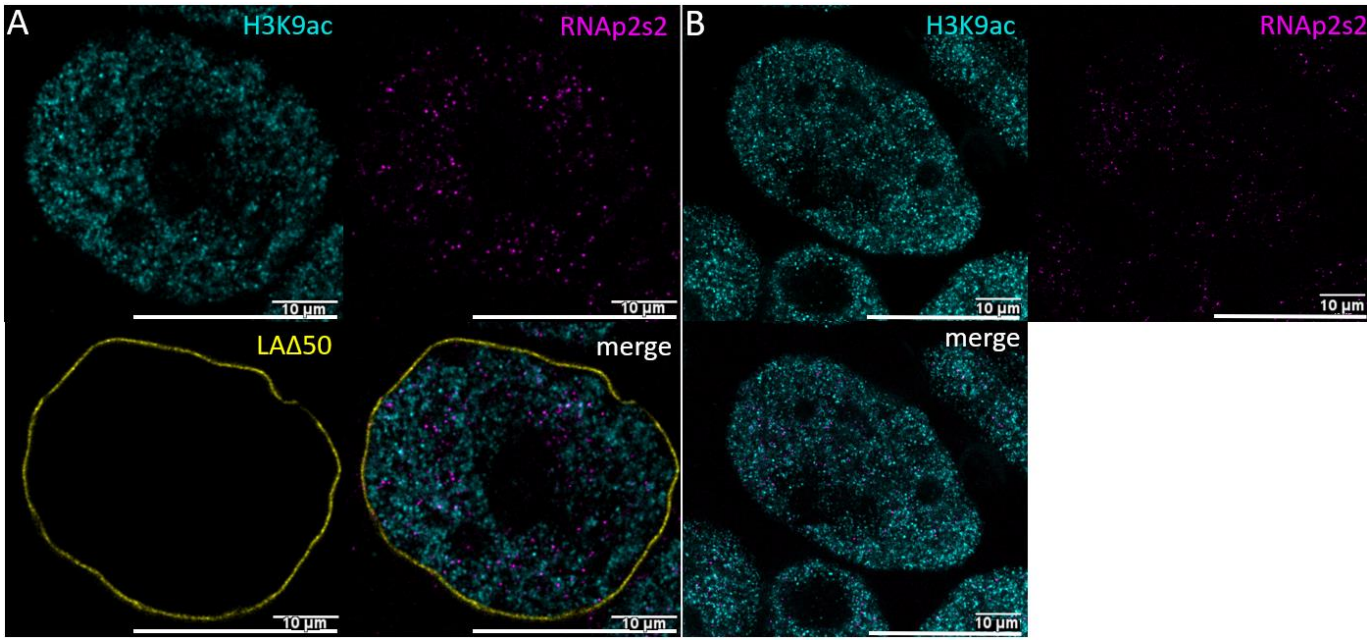

Fig. 54 Confocal 2ABR-ProExM imaging of HEK293T labeled for H3K9ac and RNAp2s2. HGPS model expressing LAΔ50-eGFP (A) and CTRL (B). The second scale bar in the images is normalized by the $EF = 4.2 \pm 0.1$

We then performed an object-based colocalization analysis (Fig. 55, N=20) to assess whether the interaction between H3K9ac and RNAp2s2 was altered in our HGPS model, but our analysis did not show any significant difference between the two sets.

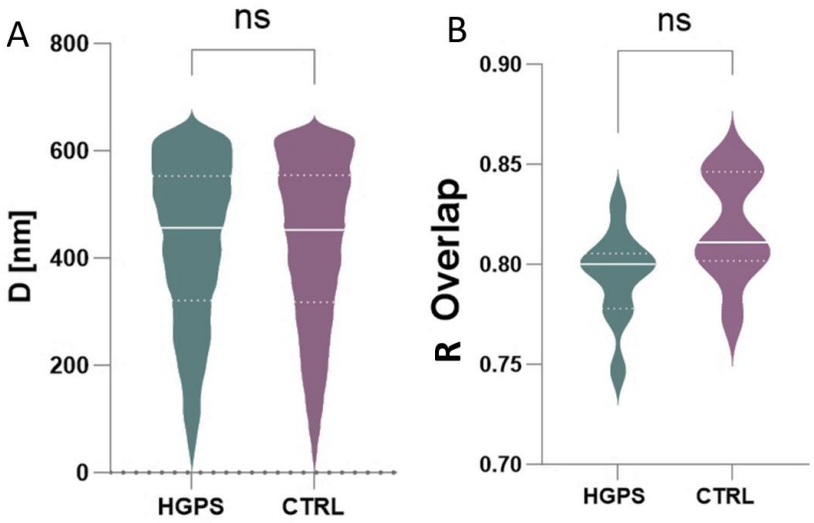

Fig. 55 JACoP object-based colocalization analysis of H3K9ac and RNAp2s2. Distance distribution (A). Overlap coefficient distribution (B). Significance evaluated Kolmogorov-Smirnov test using Prism. EF=4.2±0.1, N=20.

Subsequently, we performed particle analysis (Fig. 56, N=20) to compare the expression of the two markers. Our analysis showed a significant difference between sets for both proteins, with a decrease in H3K9ac and an increase in RNAp2s2 nuclear foci dimension in the HGPS model.

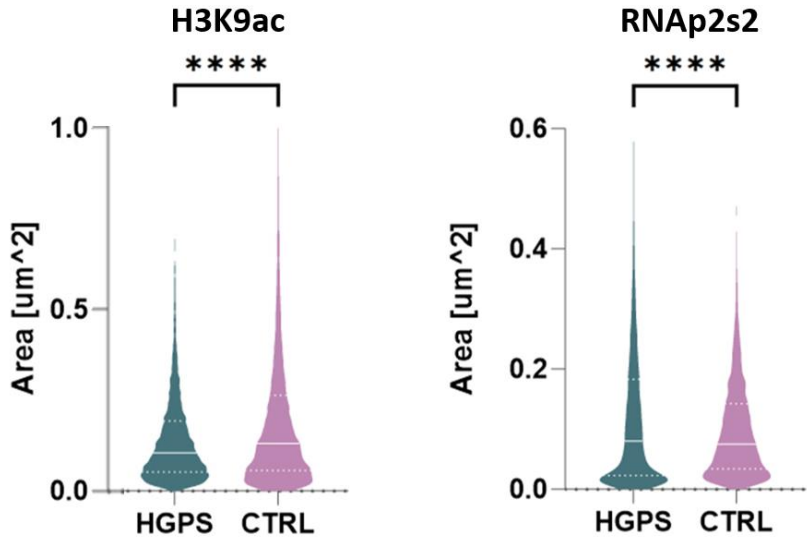

Fig. 56 Particle analysis of H3K9ac and RNAp2s2. Significance evaluated Kolmogorov-Smirnov test using Prism.EF=4.2±0.1, N=20.

Next, we performed a Western Blot (Fig. 57) to evaluate the expression of the two proteins, finding an increased expression for both proteins.

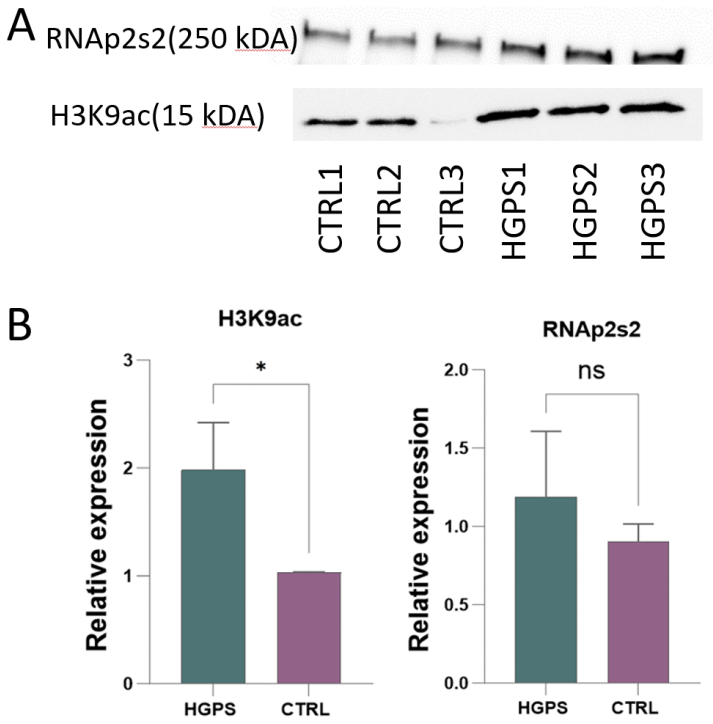

Fig. 57 Western Blot analysis of H3K9ac and RNAp2s2. Actin was used as a reporter. Chemiluminescence images of the protein blots (A). Quantification plots (B). Significance evaluated Kolmogorov-Smirnov test using Prism., N=3.

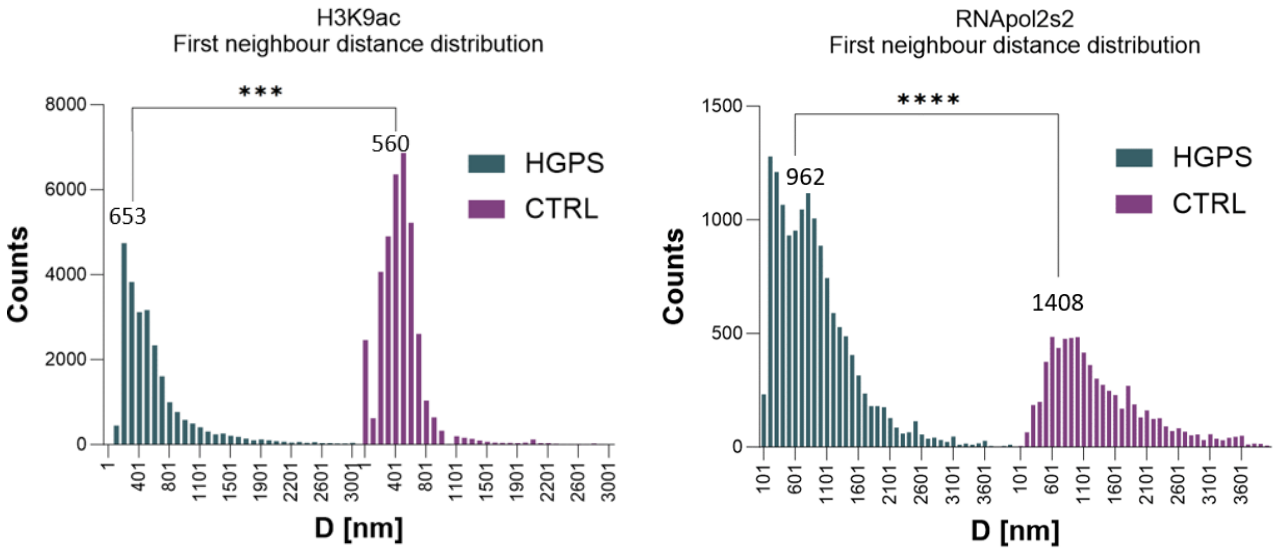

Fig. 58 First neighbor distance distribution analysis of H3K9ac and RNApol2s2. EF=4.2±0.1, N=20.

Finally, we performed a first neighbor distance distribution analysis (Fig. 58, N=20) with the following results:

- $Average\ FND_{\ \mathrm{H3K9ac},\ HGPS} = 653 \pm 4\ nm \equiv 155 \times EF \pm 4\ nm$
- $Average\ FND_{\ \mathrm{H3K9ac},\ CTRL} = 560 \pm 5\ nm\ \equiv 133 \times EF \pm 5\ nm$
- $Average\ FND_{\ \mathrm{RNAp2s2},\ HGPS} = 962 \pm 7\ nm \equiv 229 \times EF \pm 7\ nm$
- $Average\ FND_{\ \mathrm{RNAp2s2},\ CTRL} = 1408 \pm 12\ nm \equiv 335 \times EF \pm 5\ n\mathrm{m}$

Our results show a significant alteration in the distribution of both proteins, with a diminished FND for RNAp2s2 and an increased FND for H3K9ac.

To summarize, although the interaction between H3K9ac and RNAp2s2 was not impaired in our colocalization experiments, the expression of the two markers seemed to be altered in the HGPS model, especially for RNAp2s2. The increased expression of these two proteins, together with the highly reduced RNAp2s2 inter-foci distance and the increased foci dimension, results in augmented activity of the transcriptional machinery. Our findings are in accordance with the increased transcription activity previously reported in HGPS (Prokocimer et al., 2013).

7.2.6. H3K9me2

To evaluate and quantify the loss of heterochromatin in our HGPS cellular model, we immunostained the epigenetic modification H3K9me2 and, as in previously presented experiments, we first performed confocal imaging of non-expanded cells (Fig. 59).

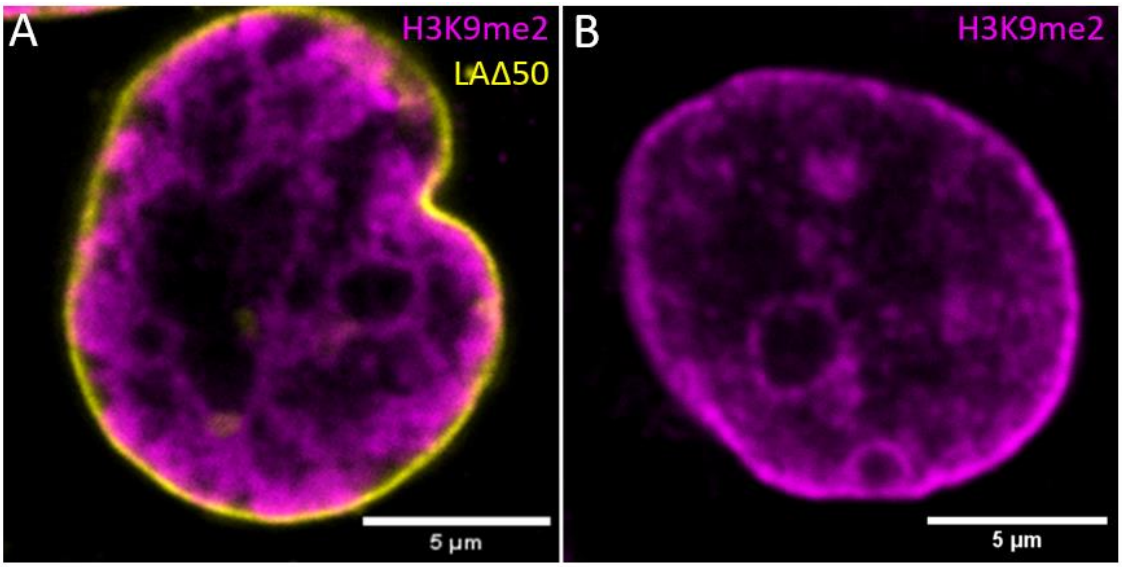

Fig. 59 Confocal imaging of non-expanded HEK293T labeled for H3K9me2. HGPS model expressing LAΔ50-eGFP (A) and CTRL (B).

Next, we used 2ABR-ProExM to achieve super-resolution imaging (Fig. 60) in order to perform quantitative analysis on the resolved histone modifications.

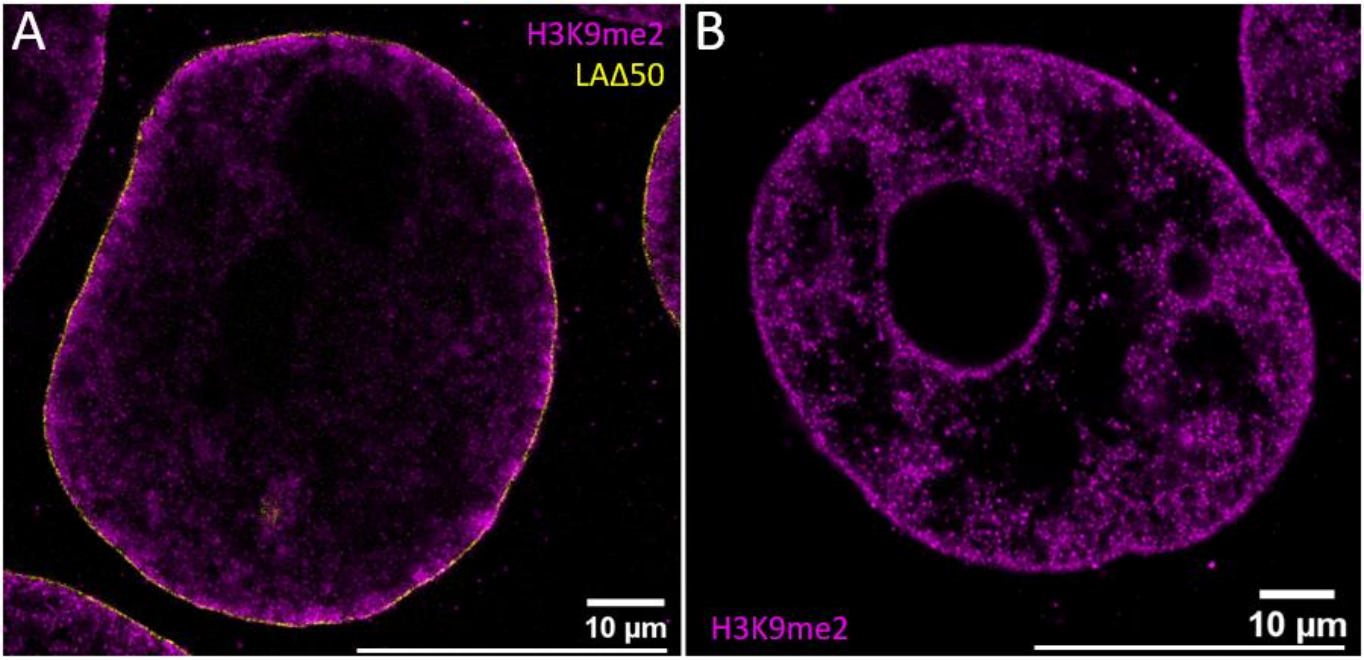

Fig. 60 Confocal 2ABR-ProExM imaging of HEK293T labeled for H3K9me2. HGPS model expressing LAΔ50-eGFP (A) and CTRL (B). The second scale bar in the images is normalized by the $EF = 4.2 \pm 0.1$

Subsequently, we performed particle and first neighbor distance distribution analyses (Fig. 61, N=20), showing a significant difference between the HGPS and the CTRL set, with an increase in H3K9me2 nuclear foci dimension.

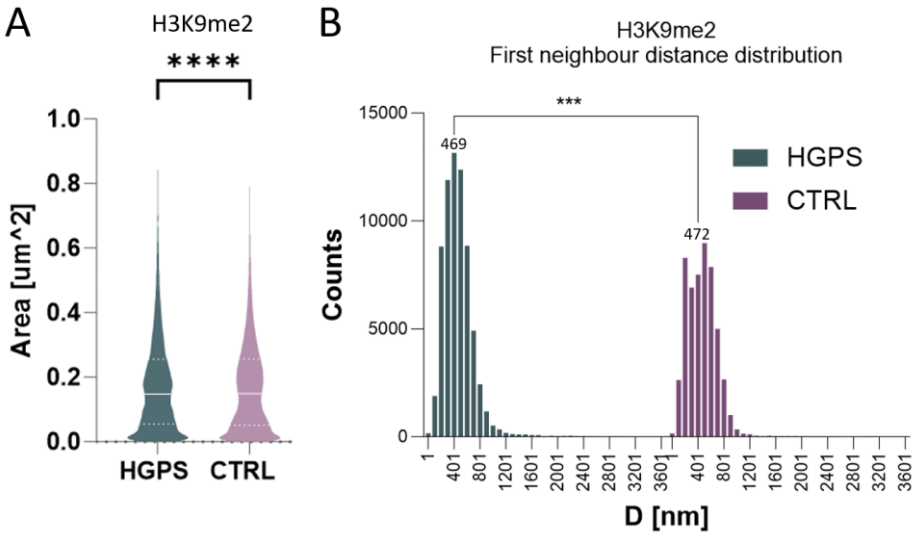

Fig. 61 Particle analysis (A) and first neighbor distance distribution analysis (B) of H3K9me2. Significance evaluated Kolmogorov-Smirnov test using Prism. EF=4.1±0.1, N=20.

The first neighbor distance analysis (Fig. 61 B) results are reported here:

- $Average\ FND_{\ \mathrm{H3K9me2},\ HGPS} = 472 \pm 1\ nm \equiv 115 \times EF \pm 1\ nm$
- $Average\ FND_{\ \mathrm{H3K9me2},\ CTRL} = 469 \pm 1\ nm \equiv 114 \times EF \pm 1\ nm$

Finally, we performed a Western Blot (Fig. 62), which revealed a slightly increased expression of H3K9me2. Our analyses show an increase in the production of H3K9me2 despite the loss of peripheral heterochromatin. These findings are coherent with the hypothesized disruption in the lamin-chromatin tethering mechanism mediated by HP1α and PRR14.

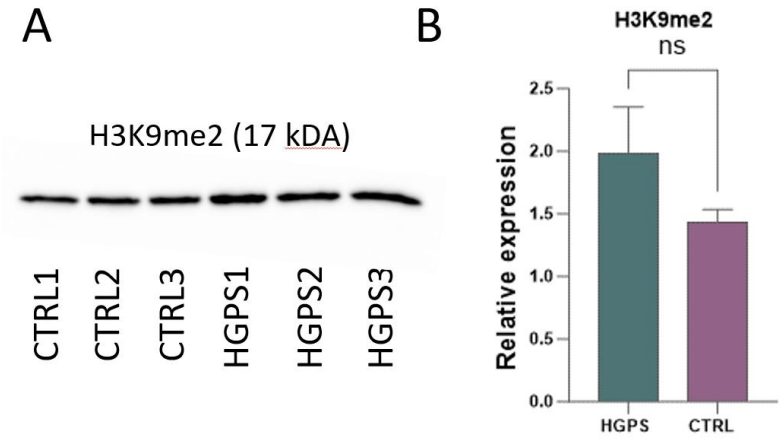

Fig. 62 Western Blot analysis of H3K9me2. Actin was used as a reporter. . Chemiluminescence images of the protein blots (A). Quantification plots (B). Significance evaluated Kolmogorov-Smirnov test using Prism, N=3.

7.2.7. Biomolecular essays

Global genomic DNA methylation analysis

The global genomic DNA methylation levels of HGPS and CTRL sets were quantified using an Enzyme-linked immunosorbent assay (ELISA). The results in Fig. 63 revealed a decrease in the global methylation level of genomic DNA in the HGPS model, which is associated with diminished gene transcription repression.

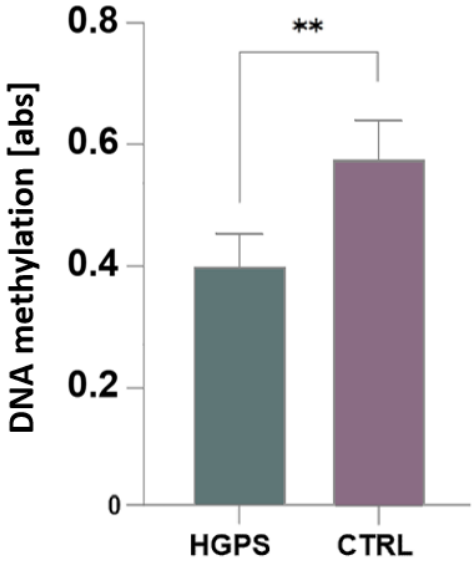

Fig. 63 Global DNA Methylation (5-mC) analysis performed using the ELISA Easy Kit (Epigentek, USA). Significance evaluated Kolmogorov-Smirnov test using Prism, N=4.

.

Quantitative real-time Polymerase Chain Reaction (qPCR)

In order to quantify the expression of the enzymes Histone acetyltransferase (KAT2A), DNA methyltransferase 1 (DNMT1), Histone-lysine N-methyltransferase (EHMT1), respectively responsible for histone acetylation, DNA methylation, and histone mutilation, qPCR was performed. The enzyme Glyceraldehyde-3-phosphate dehydrogenase (GAPDH) was used as a housekeeper. The results, showing an increased expression of all the enzymes essayed, are visible in Fig. 64.

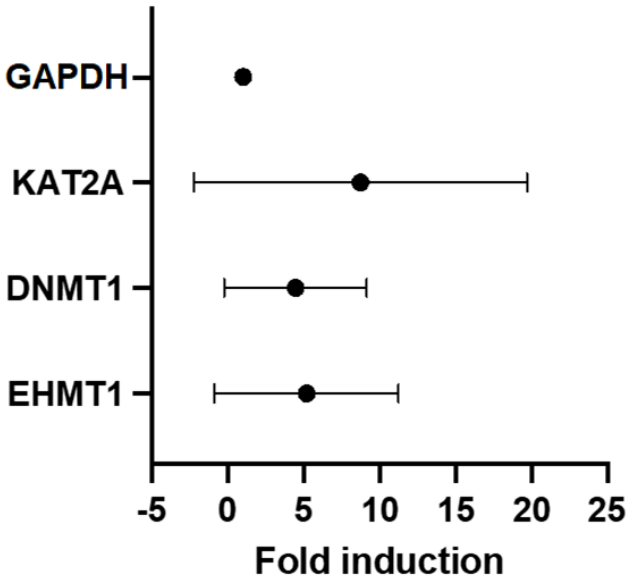

Fig. 64 Quantitative real-time Polymerase Chain Reaction (qPCR) results. HGPS relative enzyme quantification for the enzymes KAT2A, DNMT1 and EHMT1. Housekeeper enzyme GAPDH, N=3.

Overall, the performed biomolecular essays revealed a decrease in total DNA methylation despite the increased expression of the enzyme responsible, DNMT1. This result is in concordance with a recent publication reporting the same results obtained on a patient-derived cell line (Bejaoui et al., 2022). The pathway of this process in HGPS is yet to be investigated and needs further exploration.

The increased KAT2A expression in our HGPS model is consistent with the amplified transcriptional activity of euchromatin previously reported for HGPS and the augmented expression of H3K9ac presented in this work (Prokocimer et al., 2013).

Similarly, the increased expression of EHMT1 is coherent with the increased expression of H3K9me2 found in our HGPS cellular model. Our findings indicate that the loss of peripheral heterochromatin reported with HGPS is not associated with a global heterochromatin reduction but could instead be related to the alteration in the lamin-chromatin tethering mechanism caused by the accumulation of LAΔ50.

7.2.8. NPC clustering

To evaluate the presence of an alteration in the NPC distribution associated with HGPS (Röhrl et al., 2021) in our cellular model, we performed 3D-dSTORM acquisitions, as illustrated in section 6.5.3. We opted for single-molecule localization microscopy in order to resolve the single Nuclear Pore Complex units and perform a distribution analysis of this sub-resolution biological structure.

For both sets (HGPS, CTRL), we immunostained the NUP107, a nucleoporin that, unlike NUP153, is only localized in the external basked of the NPC, providing a more accurate indication of the NPC distribution. Then, single-molecule fitting and localization were performed using ThunderSTORM (Ovesný et al., 2014). The Gaussian rendering of the localization map is shown in Fig. 65.

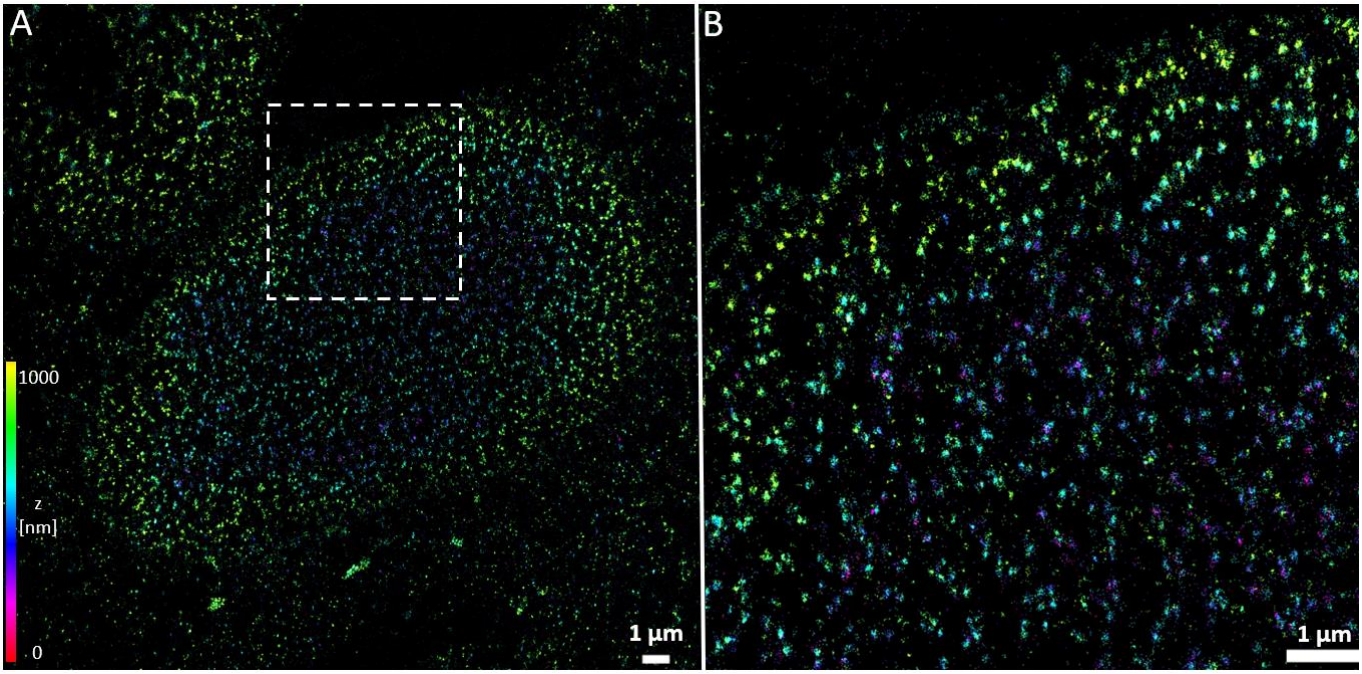

Fig. 65 3D-dSTORM acquisition of HEK293T basal layer immunolabeled for NUP107. Rendered Gaussian map, localization precision 20 nm (A). Magnification of the dashed square area in image A (B). Single-molecule fitting and localization performed using ThunderSTORM (Ovesný et al., 2014).

Subsequently, we performed a cluster analysis on the preliminary data to estimate the NPC distribution (Fig. 66). In order to identify a single cluster with a single Nuclear Pore Complex unit, we considered a cluster dimension coherent with the single NPC radius ($r_{cluster} = 60\ nm$).

The analysis (N=10) was performed using the custom Matlab algorithm described in section 6.9.4, with the following results:

- $Average\ NPC\ distance_{HGPS} = 172 \pm 9\ nm$
- $NPC\ density_{HGPS} = 10 \pm 1\ NPC\ \mu m^{-2}$
- $Average\ NPC\ distance_{CTRL} = 177 \pm 15\ nm$
- $NPC\ density_{CTRL} = 9 \pm 1\ NPC\ \mu m^{-2}$

Compared with the CTRL, the preliminary data collected did not show any alteration in the NPC distribution in our HGPS cellular model. Considering the variability of the samples and the localization precision achieved, further experiments with an increased sample size are needed.

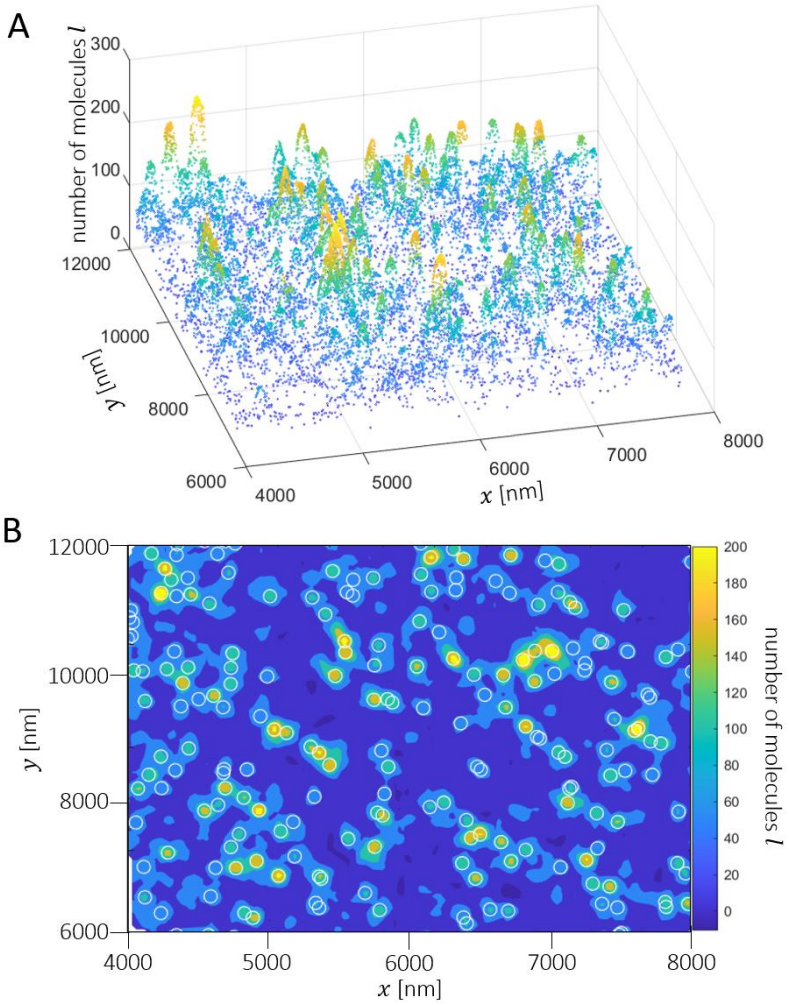

Fig. 66 Cluster analysis of HEK293T immunolabeled for NUP107 3D-dSTORM acquisition. 3D plot showing the number of molecules l for each localization (A). 2D l density map, with white circles indicating the identified clusters, corresponding to individual NPCs (B).

8. CONCLUSIONS

This doctoral thesis aimed to explore the chromatin architecture modifications associated with Hutchinson-Gilford Progeria Syndrome (HGPS) using super-resolution microscopy. The results of our study emphasize the critical role of chromatin organization in HGPS pathology and offer a deeper understanding of the cellular mechanisms underlying this rare yet enlightening condition.

The improvement in the Expansion Microscopy protocol, 2ABR-ProExM, has proven effective in significantly enhancing the fluorescent signal of immunostained biological structures. 2ABR-ProExM resulted in a notable increase in the signal-to-noise and signal-to-background ratios, allowing for the resolution of the target proteins' nuclear foci.

Super-resolution imaging of our HGPS cellular model revealed an abnormal spatial separation between chromatin and lamin at the nuclear periphery. Furthermore, our findings underscore the impact of LAΔ50 accumulation in reducing the expression of HP1α and PRR14 and their interaction, potentially disrupting the lamin-chromatin tethering mechanism.

Despite the observed loss of peripheral heterochromatin in our HGPS cellular model, our analyses revealed a global increase in the H3K9me2 nuclear foci dimension, which is consistent with the heightened expression of the enzyme EHMT1.

Our HGPS model also exhibited an elevated expression of the enzyme KAT2A, which aligns with the observed increased expression of the euchromatin marker H3K9ac. Alongside the decreased DNA methylation and the heightened RNAp2s2 expression, these findings point towards an increased transcriptional activity in HGPS.

Finally, even though the biomolecular essays showed a decrease in overall DNA methylation, the enzyme responsible for it, DNMT1, presented an increased expression. Further exploration is required to investigate the pathway of this process in HGPS.

In conclusion, this thesis has made a substantial contribution to our understanding of the biophysical aspects of HGPS through the innovative application of super-resolution microscopy. While our research primarily focused on HGPS, our findings have broader implications for understanding the aging process. The similarities between chromatin and nuclear envelope alterations in HGPS and those observed in typical aging suggest shared

underlying mechanisms. Therefore, our results expand our understanding of this rare syndrome and provide valuable insights into the fundamental processes of cellular aging, with potential ramifications for treating age-related diseases.

9. REFERENCES

Abbe, E. (1873). Beiträge zur Theorie des Mikroskops und der mikroskopischen Wahrnehmung. *Archiv Für Mikroskopische Anatomie*, *9*(1), 413–468. https://doi.org/10.1007/BF02956173

Al-Saaidi, R., & Bross, P. (2015). Do lamin A and lamin C have unique roles? *Chromosoma*, *124*(1), 1–12. https://doi.org/10.1007/s00412-014-0484-7

Alagna, N. S., Thomas, T. I., Wilson, K. L., & Reddy, K. L. (2023). Choreography of lamina-associated domains: structure meets dynamics. *FEBS Letters*, *597*(22), 2806–2822. https://doi.org/10.1002/1873-3468.14771

Allis, C. D., & Jenuwein, T. (2016). The molecular hallmarks of epigenetic control. In *Nature Reviews Genetics* (Vol. 17, Issue 8, pp. 487–500). Nat Rev Genet. https://doi.org/10.1038/nrg.2016.59

Amos, W. B., & White, J. G. (2003). How the Confocal Laser Scanning Microscope entered Biological Research. *Biology of the Cell*, *95*(6), 335–342. https://doi.org/10.1016/S0248-4900(03)00078-9

Arancio, W., Pizzolanti, G., Genovese, S. I., Pitrone, M., & Giordano, C. (2014). Epigenetic Involvement in Hutchinson-Gilford Progeria Syndrome: A Mini-Review. *Gerontology*, *60*(3), 197–203. https://doi.org/10.1159/000357206

Ashapkin, V. V., Kutueva, L. I., Kurchashova, S. Y., & Kireev, I. I. (2019). Are There Common Mechanisms Between the Hutchinson–Gilford Progeria Syndrome and Natural Aging? *Frontiers in Genetics*, *10*. https://doi.org/10.3389/fgene.2019.00455

Bates, M., Blosser, T. R., & Zhuang, X. (2005). Short-Range Spectroscopic Ruler Based on a Single-Molecule Optical Switch. *Physical Review Letters*, *94*(10), 108101. https://doi.org/10.1103/PhysRevLett.94.108101

Bejaoui, Y., Razzaq, A., Yousri, N. A., Oshima, J., Megarbane, A., Qannan, A., Potabattula, R., Alam, T., Martin, G. M., Horn, H. F., Haaf, T., Horvath, S., & El Hajj, N. (2022). DNA methylation signatures in Blood DNA of Hutchinson–Gilford Progeria syndrome. *Aging Cell*, *21*(2). https://doi.org/10.1111/acel.13555

Betzig, E., Patterson, G. H., Sougrat, R., Lindwasser, O. W., Olenych, S., Bonifacino, J. S., Davidson, M. W., Lippincott-Schwartz, J., & Hess, H. F. (2006). Imaging Intracellular Fluorescent Proteins at Nanometer Resolution. *Science*, *313*(5793), 1642–1645. https://doi.org/10.1126/science.1127344

Boisvert, F.-M., van Koningsbruggen, S., Navascués, J., & Lamond, A. I. (2007). The multifunctional nucleolus. *Nature Reviews Molecular Cell Biology*, *8*(7), 574–585. https://doi.org/10.1038/nrm2184

Bolte, S., & Cordelières, F. P. (2006). A guided tour into subcellular colocalization analysis in light microscopy. *Journal of Microscopy*, *224*(3), 213–232. https://doi.org/10.1111/j.1365-2818.2006.01706.x

Bonev, B., & Cavalli, G. (2016). Organization and function of the 3D genome. *Nature Reviews Genetics 2016 17:11*, *17*(11), 661–678. https://doi.org/10.1038/nrg.2016.112

Bridger, J. M., Foeger, N., Kill, I. R., & Herrmann, H. (2007a). The nuclear lamina. *The FEBS Journal*, *274*(6), 1354–1361. https://doi.org/10.1111/J.1742-4658.2007.05694.X

Burtner, C. R., & Kennedy, B. K. (2010). Progeria syndromes and ageing: what is the connection? *Nature Reviews Molecular Cell Biology*, *11*(8), 567–578. https://doi.org/10.1038/nrm2944

Camps, J., Erdos, M. R., & Ried, T. (2015). The role of lamin B1 for the maintenance of nuclear structure and function. *Nucleus*, *6*(1), 8–14. https://doi.org/10.1080/19491034.2014.1003510

Capell, B. C., Collins, F. S., & Nabel, E. G. (2007). Mechanisms of Cardiovascular Disease in Accelerated Aging Syndromes. *Circulation Research*, *101*(1), 13–26. https://doi.org/10.1161/CIRCRESAHA.107.153692

Castillo-Aguilera, O., Depreux, P., Halby, L., Arimondo, P., & Goossens, L. (2017). DNA Methylation Targeting: The DNMT/HMT Crosstalk Challenge. *Biomolecules*, *7*(4), 3. https://doi.org/10.3390/biom7010003

Chakravarthy, S., Park, Y.-J., Chodaparambil, J., Edayathumangalam, R. S., & Luger, K. (2005). Structure and dynamic properties of nucleosome core particles. *FEBS Letters*, *579*(4), 895–898. https://doi.org/10.1016/J.FEBSLET.2004.11.030

Chang, J. B., Chen, F., Yoon, Y. G., Jung, E. E., Babcock, H., Kang, J. S., Asano, S., Suk, H. J., Pak, N., Tillberg, P. W., Wassie, A. T., Cai, D., & Boyden, E. S. (2017). Iterative expansion microscopy. *Nature Methods*, *14*(6), 593–599. https://doi.org/10.1038/nmeth.4261

Chen, F, Wassie, A., Cote, A., Sinha, A., Alon, S., Asano, S., Daugharthy, E., Chang, J., Marblestone, A., GM, C., A, R., & ES, B. (2016). Nanoscale imaging of RNA with expansion microscopy. *Nature Methods*, *13*(8), 679–684. https://doi.org/10.1038/NMETH.3899

Chen, Fei, Tillberg, P. W., & Boyden, E. S. (2015a). Expansion microscopy. *Science*, *347*(6221), 543–548. https://doi.org/10.1126/science.1260088

Chen, Fei, Tillberg, P. W., & Boyden, E. S. (2015b). Expansion microscopy. *Science*, *347*(6221), 543–548. https://doi.org/10.1126/science.1260088

Chozinski, T. J., Halpern, A. R., Okawa, H., Kim, H.-J., Tremel, G. J., Wong, R. O. L., & Vaughan, J. C. (2016). Expansion microscopy with conventional antibodies and fluorescent proteins. *Nature Methods*, *13*(6), 485–488. https://doi.org/10.1038/nmeth.3833

Chrun, E. S., Modolo, F., & Daniel, F. I. (2017). Histone modifications: A review about the presence of this epigenetic phenomenon in carcinogenesis. In *Pathology Research and Practice* (Vol. 213, Issue 11, pp. 1329–1339). Elsevier GmbH. https://doi.org/10.1016/j.prp.2017.06.013

Cobb, A. M., Larrieu, D., Warren, D. T., Liu, Y., Srivastava, S., Smith, A. J. O., Bowater, R. P., Jackson, S. P., & Shanahan, C. M. (2016). Prelamin A impairs 53BP1 nuclear entry by mislocalizing NUP153 and disrupting the Ran gradient. *Aging Cell*, *15*(6), 1039–1050. https://doi.org/10.1111/acel.12506

Cohen, Y., Ramon, O., Kopelman, I. J., & Mizrahi, S. (1992). Characterization of inhomogeneous polyacrylamide hydrogels. *Journal of Polymer Science Part B: Polymer Physics*, *30*(9), 1055–1067. https://doi.org/10.1002/polb.1992.090300913

Conchello, J.-A., & Lichtman, J. W. (2005). Optical sectioning microscopy. *Nature Methods*, *2*(12), 920–931. https://doi.org/10.1038/nmeth815

Coppede, F. (2021). Mutations Involved in Premature-Ageing Syndromes. *The Application of Clinical Genetics*, *Volume 14*, 279–295. https://doi.org/10.2147/TACG.S273525

Costes, S. V., Daelemans, D., Cho, E. H., Dobbin, Z., Pavlakis, G., & Lockett, S. (2004). Automatic and Quantitative Measurement of Protein-Protein Colocalization in Live Cells. *Biophysical Journal*, *86*(6), 3993–4003. https://doi.org/10.1529/biophysj.103.038422

D'Angelo, M. A., & Hetzer, M. W. (2006). The role of the nuclear envelope in cellular organization. *Cellular and Molecular Life Sciences CMLS*, *63*(3), 316–332. https://doi.org/10.1007/s00018-005-5361-3

Dans, P. D., Walther, J., Gómez, H., & Orozco, M. (2016). Multiscale simulation of DNA. In *Current Opinion in Structural Biology* (Vol. 37, pp. 29–45). Elsevier Ltd. https://doi.org/10.1016/j.sbi.2015.11.011

Davis, L. I. (1995). THE NUCLEAR PORE COMPLEX. *Annual Review of Biochemistry*, *64*(1), 865–896. https://doi.org/10.1146/annurev.bi.64.070195.004245

De Magistris, P., & Antonin, W. (2018). The Dynamic Nature of the Nuclear Envelope. *Current Biology*, *28*(8), R487–R497. https://doi.org/10.1016/j.cub.2018.01.073

Dechat, T., Pfleghaar, K., Sengupta, K., Shimi, T., Shumaker, D. K., Solimando, L., & Goldman, R. D. (2008). *Nuclear lamins: major factors in the structural organization and function of the nucleus and chromatin*. https://doi.org/10.1101/gad.1652708

Diaspro, A., & Bianchini, P. (2020). Optical nanoscopy. In *Rivista del Nuovo Cimento*. Springer. https://doi.org/10.1007/s40766-020-00008-1

Doye, V., & Hurt, E. (1997). From nucleoporins to nuclear pore complexes. *Current Opinion in Cell Biology*, *9*(3), 401–411. https://doi.org/10.1016/S0955-0674(97)80014-2

Dreesen, O. (2020). Towards delineating the chain of events that cause premature senescence in the accelerated aging syndrome Hutchinson–Gilford progeria (HGPS). *Biochemical Society Transactions*, *48*(3), 981–991. https://doi.org/10.1042/BST20190882

Duc, C., & Thiriet, C. (2021). Replication-Coupled Chromatin Remodeling: An Overview of Disassembly and Assembly of Chromatin during Replication. *International Journal of Molecular Sciences*, *22*(3), 1–11. https://doi.org/10.3390/IJMS22031113

Dunst, S., & Tomancak, P. (2019). Imaging Flies by Fluorescence Microscopy: Principles, Technologies, and Applications. *Genetics*, *211*(1), 15–34. https://doi.org/10.1534/genetics.118.300227

Fuks, F., Burgers, W. A., Brehm, A., Hughes-Davies, L., & Kouzarides, T. (2000). DNA methyltransferase Dnmt1 associates with histone deacetylase activity. *Nature Genetics*, *24*(1), 88–91. https://doi.org/10.1038/71750

Gambarotto, D., Hamel, V., & Guichard, P. (2021). *Ultrastructure expansion microscopy (U-ExM)* (pp. 57–81). https://doi.org/10.1016/bs.mcb.2020.05.006

Gao, M., Maraspini, R., Beutel, O., Zehtabian, A., Eickholt, B., Honigmann, A., & Ewers, H. (2018). Expansion Stimulated Emission Depletion Microscopy (ExSTED). *ACS Nano*, *12*(5), 4178–4185. https://doi.org/10.1021/acsnano.8b00776

Gao, R., Asano, S. M., & Boyden, E. S. (2017). Q&A: Expansion microscopy. *BMC Biology*, *15*(1), 50. https://doi.org/10.1186/s12915-017-0393-3

Getis, A., & Franklin, J. (1987). Second-Order Neighborhood Analysis of Mapped Point Patterns. *Ecology*, *68*(3), 473–477. https://doi.org/10.2307/1938452

Gorlich, D. (1998). Transport into and out of the cell nucleus. *The EMBO Journal*, *17*(10), 2721–2727. https://doi.org/10.1093/emboj/17.10.2721

Guerra, J. M. (1995). Super-resolution through illumination by diffraction-born evanescent waves. *Applied Physics Letters*, *66*(26), 3555–3557. https://doi.org/10.1063/1.113814

Gustafsson, M. G. L., Shao, L., Carlton, P. M., Wang, C. J. R., Golubovskaya, I. N., Cande, W. Z., Agard, D. A., & Sedat, J. W. (2008). Three-dimensional resolution doubling in wide-field fluorescence microscopy by structured illumination. *Biophysical Journal*, *94*(12), 4957–4970. https://doi.org/10.1529/biophysj.107.120345

Happel, N., & Doenecke, D. (2009). Histone H1 and its isoforms: Contribution to chromatin structure and function. *Gene*, *431*(1–2), 1–12. https://doi.org/10.1016/J.GENE.2008.11.003

Heilemann, M. (2010). Fluorescence microscopy beyond the diffraction limit. *Journal of Biotechnology*, *149*(4), 243–251. https://doi.org/10.1016/j.jbiotec.2010.03.012

Heilemann, M., van de Linde, S., Schüttpelz, M., Kasper, R., Seefeldt, B., Mukherjee, A., Tinnefeld, P., & Sauer, M. (2008). Subdiffraction-Resolution Fluorescence Imaging with Conventional Fluorescent Probes. *Angewandte Chemie International Edition*, *47*(33), 6172–6176. https://doi.org/10.1002/anie.200802376

Hell, S.W., Jakobs, S., & Kastrup, L. (2003). Imaging and writing at the nanoscale with focused visible light through saturable optical transitions. *Applied Physics A: Materials Science & Processing*, *77*(7), 859–860. https://doi.org/10.1007/s00339-003-2292-4

Hell, Stefan W. (2005). Fluorescence nanoscopy: Breaking the diffraction barrier by the RESOLFT concept. *Nanobiotechnology*, *1*(3), 296–297. https://doi.org/10.1385/Nano:1:3:296

Hell, Stefan W., & Wichmann, J. (1994). Breaking the diffraction resolution limit by stimulated emission: stimulated-emission-depletion fluorescence microscopy. *Optics Letters*, *19*(11), 780. https://doi.org/10.1364/ol.19.000780

Hennekam, R. C. M. (2006). Hutchinson–Gilford progeria syndrome: Review of the phenotype. *American Journal of Medical Genetics Part A*, *140A*(23), 2603–2624. https://doi.org/10.1002/ajmg.a.31346

Jacinto, F. V., Benner, C., & Hetzer, M. W. (2015). The nucleoporin Nup153 regulates embryonic stem cell pluripotency through gene silencing. *Genes & Development*, *29*(12), 1224–1238. https://doi.org/10.1101/gad.260919.115

Jonkman, J. (2020). Rigor and Reproducibility in Confocal Fluorescence Microscopy. *Cytometry Part A*, *97*(2), 113–115. https://doi.org/10.1002/cyto.a.23924

Kanwal, R., & Gupta, S. (2012). Epigenetic modifications in cancer. *Clinical Genetics*, *81*(4), 303–311. https://doi.org/10.1111/j.1399-0004.2011.01809.x

Khater, I. M., Nabi, I. R., & Hamarneh, G. (2020). A Review of Super-Resolution Single-Molecule Localization Microscopy Cluster Analysis and Quantification Methods. *Patterns*, *1*(3), 100038. https://doi.org/10.1016/j.patter.2020.100038

Kiseleva, A. A., & Poleshko, A. (2023). The secret life of chromatin tethers. *FEBS Letters*, *597*(22), 2782–2790. https://doi.org/10.1002/1873-3468.14685

Ku, T., Swaney, J., Park, J. Y., Albanese, A., Murray, E., Hun Cho, J., Park, Y. G., Mangena, V., Chen, J., & Chung, K. (2016). Multiplexed and scalable super-resolution imaging of three-dimensional protein localization in size-adjustable tissues. *Nature Biotechnology*, *34*(9), 973–981. https://doi.org/10.1038/nbt.3641

Lai, W. K. M., & Pugh, B. F. (2017). Understanding nucleosome dynamics and their links to gene expression and DNA replication. *Nature Reviews. Molecular Cell Biology*, *18*(9), 548. https://doi.org/10.1038/NRM.2017.47

Lee, J. M., Nobumori, C., Tu, Y., Choi, C., Yang, S. H., Jung, H.-J., Vickers, T. A., Rigo, F., Bennett, C. F., Young, S. G., & Fong, L. G. (2016). Modulation of LMNA splicing as a strategy to treat prelamin A diseases. *Journal of Clinical Investigation*, *126*(4), 1592–1602. https://doi.org/10.1172/JCI85908

Lee, K. K., Gruenbaum, Y., Spann, P., Liu, J., & Wilson, K. L. (2000). C. elegans Nuclear Envelope Proteins

Emerin, MAN1, Lamin, and Nucleoporins Reveal Unique Timing of Nuclear Envelope Breakdown during Mitosis. *Molecular Biology of the Cell*, *11*(9), 3089–3099. https://doi.org/10.1091/mbc.11.9.3089

Lee, K. K., & Workman, J. L. (2007). Histone acetyltransferase complexes: one size doesn't fit all. *Nature Reviews Molecular Cell Biology*, *8*(4), 284–295. https://doi.org/10.1038/nrm2145

Lesterlin, C., Ball, G., Schermelleh, L., & Sherratt, D. J. (2014). RecA bundles mediate homology pairing between distant sisters during DNA break repair. *Nature*, *506*(7487), 249–253. https://doi.org/10.1038/nature12868

Liang, Y., & Hetzer, M. W. (2011). Functional interactions between nucleoporins and chromatin. *Current Opinion in Cell Biology*, *23*(1), 65–70. https://doi.org/10.1016/j.ceb.2010.09.008

Lin, D. H., & Hoelz, A. (2019). The Structure of the Nuclear Pore Complex (An Update). *Annual Review of Biochemistry*, *88*(1), 725–783. https://doi.org/10.1146/annurev-biochem-062917-011901

Luger, K. (2001). Nucleosomes: Structure and Function. *Encyclopedia of Life Sciences*. https://doi.org/10.1038/NPG.ELS.0001155

Luo, Y.-B., Mastaglia, F. L., & Wilton, S. D. (2014). Normal and aberrant splicing of LMNA. *Journal of Medical Genetics*, *51*(4), 215–223. https://doi.org/10.1136/jmedgenet-2013-102119

M, O., DG, P., & Y, T. (2018). Nucleosome-level 3D organization of the genome. *Biochemical Society Transactions*, *46*(3). https://doi.org/10.1042/BST20170388

Ma, R., Štefl, M., & Nienhaus, G. U. (2022). Single molecule localization-based analysis of clathrin-coated pit and caveolar dynamics. *Nanoscale Horizons*, *7*(4), 385–395. https://doi.org/10.1039/D2NH00008C

Markaki, Y., Gunkel, M., Schermelleh, L., Beichmanis, S., Neumann, J., Heidemann, M., Leonhardt, H., Eick, D., Cremer, C., & Cremer, T. (2010). Functional nuclear organization of transcription and DNA replication: A topographical marriage between chromatin domains and the interchromatin compartment. *Cold Spring Harbor Symposia on Quantitative Biology*, *75*, 475–492. https://doi.org/10.1101/sqb.2010.75.042

Martins, F., Sousa, J., Pereira, C. D., da Cruz e Silva, O. A. B., & Rebelo, S. (2020). Nuclear envelope dysfunction and its contribution to the aging process. *Aging Cell*, *19*(5). https://doi.org/10.1111/acel.13143

McKenna, T., Baek, J.-H., & Eriksso, M. (2013). Laminopathies. In *Genetic Disorders*. InTech. https://doi.org/10.5772/53793

Murphy D, D. M. (2012). *Fundamentals of Light Microscopy and Electronic Imaging* (2nd ed.). Wiley.

Murr, R. (2010). *Interplay Between Different Epigenetic Modifications and Mechanisms* (pp. 101–141).

https://doi.org/10.1016/B978-0-12-380866-0.60005-8

Musich, P. R., & Zou, Y. (2011). DNA-damage accumulation and replicative arrest in Hutchinson–Gilford progeria syndrome. *Biochemical Society Transactions*, *39*(6), 1764–1769. https://doi.org/10.1042/BST20110687

Nieuwenhuizen, R. P. J., Lidke, K. A., Bates, M., Puig, D. L., Grünwald, D., Stallinga, S., & Rieger, B. (2013). Measuring image resolution in optical nanoscopy. *Nature Methods*, *10*(6), 557–562. https://doi.org/10.1038/nmeth.2448

Nigg, E. A. (1989). The nuclear envelope. *Current Opinion in Cell Biology*, *1*(3), 435–440. https://doi.org/10.1016/0955-0674(89)90002-1

Ou, H. D., Phan, S., Deerinck, T. J., Thor, A., Ellisman, M. H., & O'Shea, C. C. (2017). ChromEMT: Visualizing 3D chromatin structure and compaction ninterphase and mitotic cells. *Science (New York, N.Y.)*, *357*(6349). https://doi.org/10.1126/SCIENCE.AAG0025

Ovesný, M., Křížek, P., Borkovec, J., Švindrych, Z., & Hagen, G. M. (2014). ThunderSTORM: a comprehensive ImageJ plug-in for PALM and STORM data analysis and super-resolution imaging. *Bioinformatics*, *30*(16), 2389–2390. https://doi.org/10.1093/bioinformatics/btu202

Patel, D. J., & Wang, Z. (2013). Readout of Epigenetic Modifications. *Annual Review of Biochemistry*, *82*(1), 81–118. https://doi.org/10.1146/annurev-biochem-072711-165700

Pesce, L., Diaspro, A., & Bianchini, P. (2021). Expansion microscopy. In *Imaging Modalities for Biological and Preclinical Research: A Compendium, Volume 1: Part I: Ex vivo biological imaging*. IOP Publishing. https://doi.org/10.1088/978-0-7503-3059-6ch20

Poleshko, A., Mansfield, K. M., Burlingame, C. C., Andrake, M. D., Shah, N. R., & Katz, R. A. (2013). The Human Protein PRR14 Tethers Heterochromatin to the Nuclear Lamina during Interphase and Mitotic Exit. *Cell Reports*, *5*(2), 292–301. https://doi.org/10.1016/j.celrep.2013.09.024

Poleshko, A., Smith, C. L., Nguyen, S. C., Sivaramakrishnan, P., Wong, K. G., Murray, J. I., Lakadamyali, M., Joyce, E. F., Jain, R., & Epstein, J. A. (2019). H3k9me2 orchestrates inheritance of spatial positioning of peripheral heterochromatin through mitosis. *ELife*, *8*. https://doi.org/10.7554/eLife.49278

Prokocimer, M., Barkan, R., & Gruenbaum, Y. (2013). Hutchinson–Gilford progeria syndrome through the lens of transcription. *Aging Cell*, *12*(4), 533–543. https://doi.org/10.1111/acel.12070

Rayleigh. (1879). XXXI. Investigations in optics, with special reference to the spectroscope. *The London, Edinburgh, and Dublin Philosophical Magazine and Journal of Science*, *8*(49), 261–274. https://doi.org/10.1080/14786447908639684

Rippe, K. (2007). Dynamic organization of the cell nucleus. *Current Opinion in Genetics & Development*,

17(5), 373–380. https://doi.org/10.1016/j.gde.2007.08.007

Roberti, M. J., Lopez, L. O., Ossato, G., Steinmetz, I., Haas, P., Hecht, F., & Alvarez, L. A. (2020). TauSense: a fluorescence lifetime-based tool set for everyday imaging. *Nature Methods*, *September*. https://www.nature.com/articles/d42473-020-00364-w

Röhrl, J. M., Arnold, R., & Djabali, K. (2021). Nuclear Pore Complexes Cluster in Dysmorphic Nuclei of Normal and Progeria Cells during Replicative Senescence. *Cells*, *10*(1), 153. https://doi.org/10.3390/cells10010153

Rossetto, D., Avvakumov, N., & Côté, J. (2012). Histone phosphorylation. *Epigenetics*, *7*(10), 1098–1108. https://doi.org/10.4161/epi.21975

Rust, M. J., Bates, M., & Zhuang, X. (2006). Sub-diffraction-limit imaging by stochastic optical reconstruction microscopy (STORM). *Nature Methods*, *3*(10), 793–796. https://doi.org/10.1038/nmeth929

Scaffidi, P., & Misteli, T. (2005). Reversal of the cellular phenotype in the premature aging disease Hutchinson-Gilford progeria syndrome. *Nature Medicine*, *11*(4), 440–445. https://doi.org/10.1038/nm1204

Sheppard, C. J. R., & Choudhury, A. (1977). Image Formation in the Scanning Microscope. *Http://Dx.Doi.Org/10.1080/713819421*, *24*(10), 1051–1073. https://doi.org/10.1080/713819421

Small, A., & Stahlheber, S. (2014). Fluorophore localization algorithms for super-resolution microscopy. *Nature Methods*, *11*(3), 267–279. https://doi.org/10.1038/nmeth.2844

Soeller, C., & Jayasinghe, I. D. (2018). Quantitative Super-Resolution Microscopy of Cardiomyocytes. In *Microscopy of the Heart* (pp. 37–73). Springer International Publishing. https://doi.org/10.1007/978-3-319-95304-5_3

SW, H., & J, W. (1994). Breaking the diffraction resolution limit by stimulated emission: stimulated-emission-depletion fluorescence microscopy. *Optics Letters*, *19*(11), 780. https://doi.org/10.1364/OL.19.000780

T. Wilson, C. J. R. S. (1984). *Theory and practice of scanning optical microscopy*. Academic Press.

Tillberg, P. W., Chen, F., Piatkevich, K. D., Zhao, Y., Yu, C. C., English, B. P., Gao, L., Martorell, A., Suk, H. J., Yoshida, F., Degennaro, E. M., Roossien, D. H., Gong, G., Seneviratne, U., Tannenbaum, S. R., Desimone, R., Cai, D., & Boyden, E. S. (2016). Protein-retention expansion microscopy of cells and tissues labeled using standard fluorescent proteins and antibodies. *Nature Biotechnology*, *34*(9), 987–992. https://doi.org/10.1038/nbt.3625

Toraldo di Francia, G., Francia, T. di, & G. (1955). Resolving power and information. *JOSA*, *45*(7), 497.

Tremethick, D. J. (2007). Higher-Order Structures of Chromatin: The Elusive 30 nm Fiber. In *Cell* (Vol. 128, Issue 4, pp. 651–654). Elsevier B.V. https://doi.org/10.1016/j.cell.2007.02.008

Uzer, G., Fuchs, R. K., Rubin, J., & Thompson, W. R. (2016). Concise Review: Plasma and Nuclear Membranes Convey Mechanical Information to Regulate Mesenchymal Stem Cell Lineage. *Stem Cells*, *34*(6), 1455–1463. https://doi.org/10.1002/stem.2342

VAISSIERE, T., SAWAN, C., & HERCEG, Z. (2008). Epigenetic interplay between histone modifications and DNA methylation in gene silencing. *Mutation Research/Reviews in Mutation Research*, *659*(1–2), 40–48. https://doi.org/10.1016/j.mrrev.2008.02.004

van de Linde, S., Löschberger, A., Klein, T., Heidbreder, M., Wolter, S., Heilemann, M., & Sauer, M. (2011). Direct stochastic optical reconstruction microscopy with standard fluorescent probes. *Nature Protocols*, *6*(7), 991–1009. https://doi.org/10.1038/nprot.2011.336

van de Linde, S., & Sauer, M. (2014). How to switch a fluorophore: from undesired blinking to controlled photoswitching. *Chem. Soc. Rev.*, *43*(4), 1076–1087. https://doi.org/10.1039/C3CS60195A

Vaquerizas, J. M., Suyama, R., Kind, J., Miura, K., Luscombe, N. M., & Akhtar, A. (2010). Nuclear Pore Proteins Nup153 and Megator Define Transcriptionally Active Regions in the Drosophila Genome. *PLoS Genetics*, *6*(2), e1000846. https://doi.org/10.1371/journal.pgen.1000846

Vicidomini, G., Bianchini, P., & Diaspro, A. (2018). STED super-resolved microscopy. In *Nature Methods* (Vol. 15, Issue 3, pp. 173–182). Nat Methods. https://doi.org/10.1038/nmeth.4593

Vicidomini, G., Schönle, A., Ta, H., Han, K. Y., Moneron, G., Eggeling, C., & Hell, S. W. (2013). STED Nanoscopy with Time-Gated Detection: Theoretical and Experimental Aspects. *PLoS ONE*, *8*(1), e54421. https://doi.org/10.1371/journal.pone.0054421

Wassie, A. T., Zhao, Y., & Boyden, E. S. (2019). Expansion microscopy: principles and uses in biological research. *Nature Methods*, *16*(1), 33–41. https://doi.org/10.1038/s41592-018-0219-4

Wilson, K. L., & Berk, J. M. (2010). The nuclear envelope at a glance. *Journal of Cell Science*, *123*(12), 1973–1978. https://doi.org/10.1242/jcs.019042

Zhao, Y., Bucur, O., Irshad, H., Chen, F., Weins, A., Stancu, A. L., Oh, E.-Y., DiStasio, M., Torous, V., Glass, B., Stillman, I. E., Schnitt, S. J., Beck, A. H., & Boyden, E. S. (2017). Nanoscale imaging of clinical specimens using pathology-optimized expansion microscopy. *Nature Biotechnology*, *35*(8), 757–764. https://doi.org/10.1038/nbt.3892

10. LIST OF PUBLICATIONS

10.1. Articles

F. Baldini, I. Cainero, L. Cuneo, M. Oneto, E. Gatta, **C. Usai**, P. Bianchini, A. Pagano, L. Vergani and A. Diaspro, "Investigating nanoscale chromatin alterations involved in neuroblastoma transformation by optical Nanoscopy", *Il Nuovo Cimento*, **2022**.

C. Usai, I. Cainero, F. Baldini, S. Civita, L. Cuneo, P. Bianchini, A. Diaspro, in preparation.

I.Cainero, F.Baldini, A. Pierzynska-Mach, **C. Usai**, P. Bianchini, A.Diaspro. "Chromatin landscapes investigated by Optical microscopy methods", *Biophysical Reports*, in preparation.

10.2. Conference Proceedings

C. Usai, M. Oneto, I. Cainero, F. Baldini, A. Pierzynska-Mach, P. Bianchini, A. Diaspro. (**2021**) "*Evaluating the effect of different expansion microscopy protocols on mammalian DNA-chromatin architecture*" EUROPEAN BIOPHYSICS JOURNAL WITH BIOPHYSICS LETTERS 50 (SUPPL 1), 118-118

F. Baldini, I. Cainero, **C. Usai**, P. Bianchini, A. Pagano, L. Vergani, A. Diaspro. (**2021**) "Deciphering th nanoscale structure of chromatin during neuroblastoma transformation by optical nanoscopy". EUROPEAN BIOPHYSICS JOURNAL WITH BIOPHYSICS LETTERS 50 (SUPPL 1), 115-115

I. Cainero, F. Baldini, **C. Usai**, P. Bianchini, A. Diaspro. (**2021**) "*Nanoscale investigation of Nucleoplasmic Reticulum and chromatin organization*". EUROPEAN BIOPHYSICS JOURNAL WITH BIOPHYSICS LETTERS 50 (SUPPL 1), 190-190

F. Baldini, I. Cainero, **C. Usai**, P. Bianchini, A. Pagano, L. Vergani, A. Diaspro (**2021**). "*Deciphering the nanoscale structure of chromatin during neuroblastoma transformation by optical nanoscopy"*. EUROPEAN BIOPHYSICS JOURNAL WITH BIOPHYSICS LETTERS 50 (SUPPL 1), 115-115

I. Cainero, E. Cerutti, F. Baldini, **C. Usai**, P. Bianchini, A. Diaspro, L. Lanzanò (**2021**) "*Novel approaches to reconstruct and analyze Structured Illumination Microscopy data*"**.** XXV Congresso Nazionale SIBPA. June 28th- July 1st.

I. Cainero, F. Baldini**, C. Usai**, P. Bianchini, A. Diaspro (**2021**) "*Nucleoplasmic Reticulum role investigated by Super-Resolution Microscopy*". 107° Congresso della Società Italiana di Fisica, (September 13th-17th)

F. Baldini, I. Cainero, L. Cuneo, **C. Usai**, P. Bianchini, L. Vergani, A. Pagano, A. Diaspro. (**2021**). "Investigating nanoscale chromatin alterations involved in neuroblastoma transformation by optical nanoscopy". 107° Congresso della Società Italiana di Fisica (September 13th-17th).

C. Usai, I. Cainero, L. Cuneo, F. Baldini, M. Mariangeli, I. Nepita, P. Bianchini, Diaspro (**2022**).

"Investigating the role of chromatin compaction at the nanoscale in Hutchinson-Gilford progeria syndrome using expansion microscopy". Biophysical Journal, vol. 121 (3).

F. Baldini, I. Cainero, L. Cuneo, I. Nepita, **C. Usai**, P. Bianchini, L. Vergani, A. Pagano, A. Diaspro (**2022**). "*Decrypting nanoscale chromatin architecture alterations implicated in neuroblastoma transformation by optical nanoscopy*". Biophysical Journal, vol. 121 (3).

C. Usai, I. Cainero, L. Cuneo, F. Baldini, P. Bianchini, A. Diaspro (**2023**), "Decrypting the Spatial Relationship between Peripheral Chromatin and Nuclear Lamina in Hutchinson-Gilford Progeria Syndrome Using Super Resolution Microscopy Techniques", Biophysical Journal, vol. 122, (3).

C. Usai, I. Cainero, L. Cuneo, F. Baldini, P. Bianchini, A. Diaspro, "Expansion Microscopy As a Tool to Explore the Spatial Relationship between Chromatin nd Nuclear Lamin in Hutchinson-Gilford Progeria Syndrome", FOM2023, Porto, Portugal, April 2-5, **2023**.

A. Diaspro, P. Bianchini, L. Cuneo, F. Baldini, I. Cainero, **C. Usai,** S. Civita, M.Oneto, M. Mariangeli (**2023**) *"Optical nanoscopy challenges in the metaverse era. The case of multimodal imaging of chromatin in the nucleus"*, Biophysical Journal, vol. 122, (3).

Mariangeli, **C. Usai,** S. Civita, S. Dante, P. Delcanale, S. Abruzzetti, A. Diaspro, C. Viappiani, P. Bianchini (**2023**), *"Photosensitizers against pathogens: Model membranes characterization with hypericin"*, Biophysical Journal, vol. 122, (3).

10.3. Oral Presentations

"Expansion Microscopy: a tool to explore the role of chromatin compaction in Hutchinson-Gilford Progeria Syndrome", Focus on Microscopy, held virtually, April 11, **2022**.

"Investigating the spatial relationship between Chromatin and Lamin at the nuclear periphery in Hutchinson-Gilford Progeria Syndrome using Expansion Microscopy", XXVI Congresso Nazionale SIBPA, San Miniato (PI), September 13, **2022**.

"Sample preparation and Expansion Microscopy", invited lecturer at the 6th NIC@IIT Practical Workshop on Advanced Microscopy, 29th November-3rt December **2022**.

" Unraveling the Spatial Relationship between Peripheral Chromatin and Nuclear Lamina in Hutchinson-Gilford Progeria Syndrome using Super-Resolution Microscopy Techniques", Biocube Meeting 2022, Sestriere (TO), December 11th-18th, **2022**.

"Unlocking nano-scale insights into Hutchinson-Gilford Progeria Syndrome using Expansion Microscopy", Focus on Microscopy, Genova (GE), March 24th-27th, **2024**.

10.4. Scientific Courses and Workshops

6th Nikon School NIC@IIT, Practical Workshop on Advanced Microscopy, Istituto Italiano di Tecnologia, Genova, November 30th to December 3rd **2021**.

International school of Physics "Enrico Fermi", course 210 "Multimodal and Nanoscale Optical Microscopy", Varenna, Italy 10-15 July **2022**.

7th Nikon School NIC@IIT, Practical Workshop on Advanced Microscopy, Istituto Italiano di Tecnologia, Genova, November 28th to December 2nd **2022**

Biocube Meeting, Sestriere (TO), December 11th-18th, **2022**.

10.5. Teaching experience

"Sample Preparation and Expansion Microscopy", 6th Nikon School NIC@IIT, Practical Workshop on Advanced Microscopy, Istituto Italiano di Tecnologia, Genova, November 30th to December 3rd **2021**.

"Validating Expansion Microscopy from macro- to nanoscale using NPC and other intrinsic reporters", ExM User Group Meeting, held virtually, October 5th, **2022**.

"Sample Preparation and Expansion Microscopy", 7th Nikon School NIC@IIT, Practical Workshop on Advanced Microscopy, Istituto Italiano di Tecnologia, Genova, November 28th to December 2nd **2022**

"Sample Preparation and Expansion Microscopy", 8th Nikon School NIC@IIT, Practical Workshop on Advanced Microscopy, Istituto Italiano di Tecnologia, Genova, November 27th to December 1st **2023**

"Expansion Microscopy", Focus on The Invisible, Microscopy School, Fondazione Golinelli, Bologna (BO), held virtually**, 2023**